BIMODAL FORCING OF A SHARP-EDGED IMPINGING JET WITH CONSIDERATION OF WALL COOLING

By

Basil Abdelmegied

A DISSERTATION

Submitted to
Michigan State University
in partial fulfillment of the requirements
for the degree of

Mechanical Engineering- Doctor of Philosophy

2023

ABSTRACT

With the current oil price inflation, there is a crucial need for reducing the fuel consumption of gas turbines/jet engines by increasing the turbine efficiency. More crucially, this would also reduce carbon emissions due to less fuel consumption, which is necessary to combat global warming. Enhancing the gas turbine efficiency can be fulfilled by increasing the turbine's operating temperature via enhanced cooling of the turbine blades. One of the methods typically used for effective cooling of gas turbine blades utilizes impinging jets. The present work is primarily focused on investigating the change in the development of the vortex structure of an impinging jet caused by a novel flow excitation technique. A secondary objective is to examine if this change might have the potential for enhanced cooling of the impingement surface. The flow excitation approach, known as bi-modal forcing, utilizes two excitation frequencies: the initial instability frequency of the jet shear layer and its subharmonic. This type of forcing involves several parameters: the intermodal phase (ϕ) , the modal amplitude ratio (AR), and the overall forcing level. While an abundance of studies exists on pure harmonic excitation of impinging jets, there is a lack of similar investigations utilizing bi-modal forcing. With rare exceptions, existing studies of bi-modal forcing are for the non-impinging jet.

The present study utilizes an impinging jet with a sharp-edged exit of diameter D at a Reynolds number based on the jet exit velocity and diameter of $Re_D=4,233$. A high-speed time-resolved flow visualization study is conducted at a forcing amplitude of 0.3%, AR=1, the full range of ϕ (0° – 180°), and jet to impingement plate distance of H/D=2. The flow visualization results are complemented with single hot-wire measurements for cases deemed interesting. Flow visualization experiments are also conducted for AR=0.5 and 2, forcing level of 0.1% and H/D=3 and 4. Temperature sensitive paint is used for preliminary measurements of Nusselt

number on the impingement plate under constant heat flux heating. The natural jet and pureharmonic forcing at the fundamental and the subharmonic frequency are also studied as benchmark cases for bi-modal forcing.

Results show that all modes of forcing accelerate the development of the vortex structure by producing two vortex pairings ahead of the impingement plate at H/D=2. This double-paired structure is rarely seen in the natural jet and is promoted the most under *pure subharmonic* forcing and bi-modal forcing. The intermodal phase is found to have a strong effect with the double-paired structure remaining symmetric (between the visualized top and bottom parts of the shear layer) at $\phi \approx 165^{\circ}$, or exhibiting significant asymmetry and disorganization at $\phi \approx 90^{\circ}$. The main distinction between bi-modal forcing at $\phi = 165^{\circ}$ and pure subharmonic forcing is that the doublepaired vortex structure is more persistent and occurs with better cycle-to-cycle repeatability in the former case. With subharmonic forcing alone, the vortex structure is more energetic but exhibits some random switching between the symmetric double-paired structure, asymmetric structure, and single-paired structure. Overall, the promotion of double-pairing leads to faster narrowing of the jet core and stronger vortex-wall interaction. Preliminary heat transfer measurements also indicate a positive influence of bi-modal forcing on heat transfer in the stagnation zone accompanied by negative influence at larger radial locations. These opposing effects can be balanced by the choice of ϕ . The heat transfer data are preliminary and need to be confirmed and examined in further depth by future studies.

Copyright by BASIL ABDELMEGIED 2023 To my parents, lovely wife and my son

ACKNOWLEDGMENTS

First, I would like to thank my parents for their continuous support, I would have not made it to this point without them. They have helped me complete this journey, every step of the way. They have always been my best motivators and listeners. Thank you for everything, especially the continuous supplications. Thanks to my siblings, they have always got my back and gave me strength.

I want to thank my wife for her help and support. Even though she joined me towards the end of my Ph.D. journey, this part has been the most stressful part. Sincerely, I want to thank you for your patience, support, and lots of discussions. This time would have been inevitably tough without you and Adam who, recently, joined our little family.

I would like to express my special thanks and extreme gratitude to my supervisor, Dr. Ahmed Naguib for his invaluable advice, continuous support, and patience during my Ph.D. study. His immense knowledge has encouraged me and guided me. I would like to thank my committee members (Dr. Petty, Dr. Benard, and Dr. Mejia) for their discussions and comments on my work. A lot of thanks to my colleagues (David Olson, Mitch Albrecht, Kian Kalan, Borhan Hamdani, and Hussam Jabbar) for their technical discussions and the friendly environment. It would have been tough without you guys. I would also like to extend my thanks to Roy Baliff and Mike Koschmider for their help in fabricating and the experimental apparatus.

Thanks to the Egyptian and the Islamic community for making life in East Lansing enjoyable. I would like to acknowledge the support of the National Science Foundation for funding this project through NSF grant number CBET-1603720. Any opinions, findings, and conclusions expressed are those of the author and do not necessarily reflect the views of NSF.

TABLE OF CONTENTS

LIST OF SYMBOLS AND ABBREVIATIONS	ix
CHAPTER 1. INTRODUCTION	1
1.1 Literature Review	2
1.1.1 Jets: free and impinging	3
1.1.2 Active control and bi-modal forcing of jets	8
1.1.3 Heat transfer of natural and forced impinging jets	11
1.2 Motivation	
1.3 Objectives	14
CHAPTER 2. EXPERIMENTAL SETUP AND PROCEDURES	16
2.1 Jet Facility	17
2.1.1 Jet assembly	17
2.2 Experimental Techniques	26
2.2.1 Velocity measurements	
2.2.2 Flow visualization	30
2.2.3 Forcing of the jet flow	39
2.3 Experimental Procedures, Parameters and Data Analysis	
2.3.1 Velocity profiles	47
2.3.2 Flow visualization	49
2.3.3 Acoustic Forcing	51
CHAPTER 3. FLOW VISUALIZATION	53
3.1 Intermodal Phase (ϕ) Effect	53
3.1.1 Time-averaged analysis	53
3.1.2 Time-resolved analysis	63
3.1.3 Quantitative analysis	73
3.2 Forcing Amplitude Level	85
3.3 Amplitude Ratio (<i>AR</i>)	87
3.4 Impingement Plate Location	89
CHAPTER 4. HOT-WIRE MEASUREMENTS	92
4.1 Mean and RMS Radial and Streamwise Velocity Profiles	93
4.2 Modal Energy Evolution	
4.2.1 Radial modal RMS profiles	
4.2.2 Streamwise development of modal energy in the shear layer	110
4.3 Streamwise Development of Modal Coherence and Phase	
4.3.1 Modal coherence	122
4.3.2 Intermodal and modal phase	127
CHAPTER 5. PRELIMINARY HEAT TRANSFER EXPERIMENTS	136
5.1 Experimental Techniques	
5.2 Experimental Procedures and Data Analysis	144
5.3 Results	147

CHAPTER 6. CONCLUSIONS AND RECOMMENDATIONS	. 156
BIBLOGRAPHY	. 162
APPENDIX	. 167

LIST OF SYMBOLS AND ABBREVIATIONS

List of Abbreviations

ADC Analog to Digital converter

CCD Charged-coupled device

CL Centerline

CTA Constant Temperature Anemometer

DAC Digital to Analog converter

RMS Root mean square

RTD Resistance temperature detector

SNR Signal to noise ratio

pdf Probability density function

TSP Temperature sensitive paint

List of Symbols

 a_f Pressure amplitude of the acoustic forcing at the fundamental frequency

 a_{fsu} Pressure amplitude of the acoustic forcing at the subharmonic frequency

AR Amplitude ratio $\left(\frac{a_f}{a_{f_{SU}}}\right)$

 C_w Particle-free core width

 $C_{w,min}$ Minimum particle-free core width

D Jet exit diameter

E Hot-wire output voltage

 E_c Corrected hot-wire output voltage

 E_m Measured hot-wire output voltage

 E_{nr} Temperature sensitive paint excitation energy

f Fundamental mode frequency

 f_{su} Subharmonic mode frequency

 f_{2su} Second subharmonic mode frequency

H Nozzle-to-plate distance

h Convective heat transfer coefficient

 L_{pc} Potential core length

Nu Nusselt number

 Nu_0 Nusselt number at stagnation point

 P_s Stagnation pressure

 P_{atm} Atmospheric pressure

*P*_{static} Static pressure

R Universal gas constant

 R_{xy} Cross correlation coefficient in the pattern recognition scheme

 Re_D Reynolds number based on jet exit diameter and average jet velocity at the jet exit

r Radial polar coordinate

 r_o Hotwire overheat ratio

S Nozzle-to-Nozzle distance

 St_D Strouhal number based on jet exit diameter and average jet velocity at the jet exit

 St_{θ_i} Strouhal number based on initial shear-layer thickness and average jet velocity at

the jet exit

 T_a Ambient temperature

 T_{cal} Air temperature during hot-wire calibration

T_m	Air temperature during hot-wire measurements
T_p	Time percentage the double-paired symmetric structure is present
T_w	Hot wire temperature
U_j	Average velocity at the jet exit
U_{vc}	Vena-contracta velocity
и	Instantaneous velocity
u'	RMS of the fluctuating velocity component
u_f'	RMS of the fundamental mode fluctuating velocity component
$u_{f_{su}}^{\prime}$	RMS of the subharmonic mode fluctuating velocity component
$u_{f_{2su}}^{\prime}$	RMS of the second subharmonic mode fluctuating velocity component
x	Streamwise coordinate
у	Transverse coordinate
Z	Cross-stream coordinate
ν	Fluid kinematic viscosity
α	Resistance-temperature coefficient of hot-wire material
ϕ	Intermodal phase between the fundamental and the subharmonic mode
ϕ_r	Intermodal phase between the fundamental and the subharmonic mode at the
ϕ_s	Intermodal phase between the subharmonic and the second subharmonic mode
Φ	Spectral energy
θ	Azimuthal polar coordinate
$ heta_i$	Initial shear layer momentum thickness

CHAPTER 1. INTRODUCTION

Impinging jets have several important engineering applications, such as drying, heating, cooling, mixing, ventilation, and vertical/short take-off and landing of aircraft. Understanding of the flow physics of these jets will facilitate developing control methods of the flow field. This is beneficial for enhancing mixing or the convective heat transfer coefficient from the impingement surface. One of the significant applications of impinging jets is cooling of gas turbine blades, highpower electronics, and other devices. The present work is partly motivated by the cooling of gas turbine blades, where enhancement in the cooling ability of impinging jets would allow a higher operating temperature of the gas turbine, consequently yielding an improved turbine efficiency. This in turn, would enable higher power to weight ratio of a gas turbine, which would be of great benefit for jet engines. The higher gas turbine efficiency will not only conserve the finitelyavailable fossil fuel resources and save energy, but it will also reduce greenhouse gases and environmental pollution. Another important role of impinging jets is cooling of high-performance electronics, which are utilized in many applications such as high-performance computers, airspace, aviation, and maritime applications. These electronics are usually located in a tight space and require the most efficient way of cooling to allow high performance.

This thesis focuses on the study of the flow, with some preliminary consideration of the heat transfer, of an impinging jet that emerges from a sharp-edged orifice and impacts a flat plate, as illustrated in Figure 1. The coordinate system is defined as follows: the streamwise direction is x, the transverse direction is y, and the direction normal and into to the paper is z. Polar coordinates are also used, where the radial direction from the center of the jet is defined as r and the azimuthal angle is defined as θ . Two main parameters define the flow geometry: the first is the jet exit diameter D, and the second is the spacing between the jet exit (x = 0) and the impingement plate

H. The impinging-jet flow zones are typically divided into four different zones, the initial development zone (near the jet lip), the free-jet zone (before the jet is influenced by the presence of the impingement surface), the stagnation zone (extending radially outward from r=0 to r=D), and the wall-jet zone (r>D).

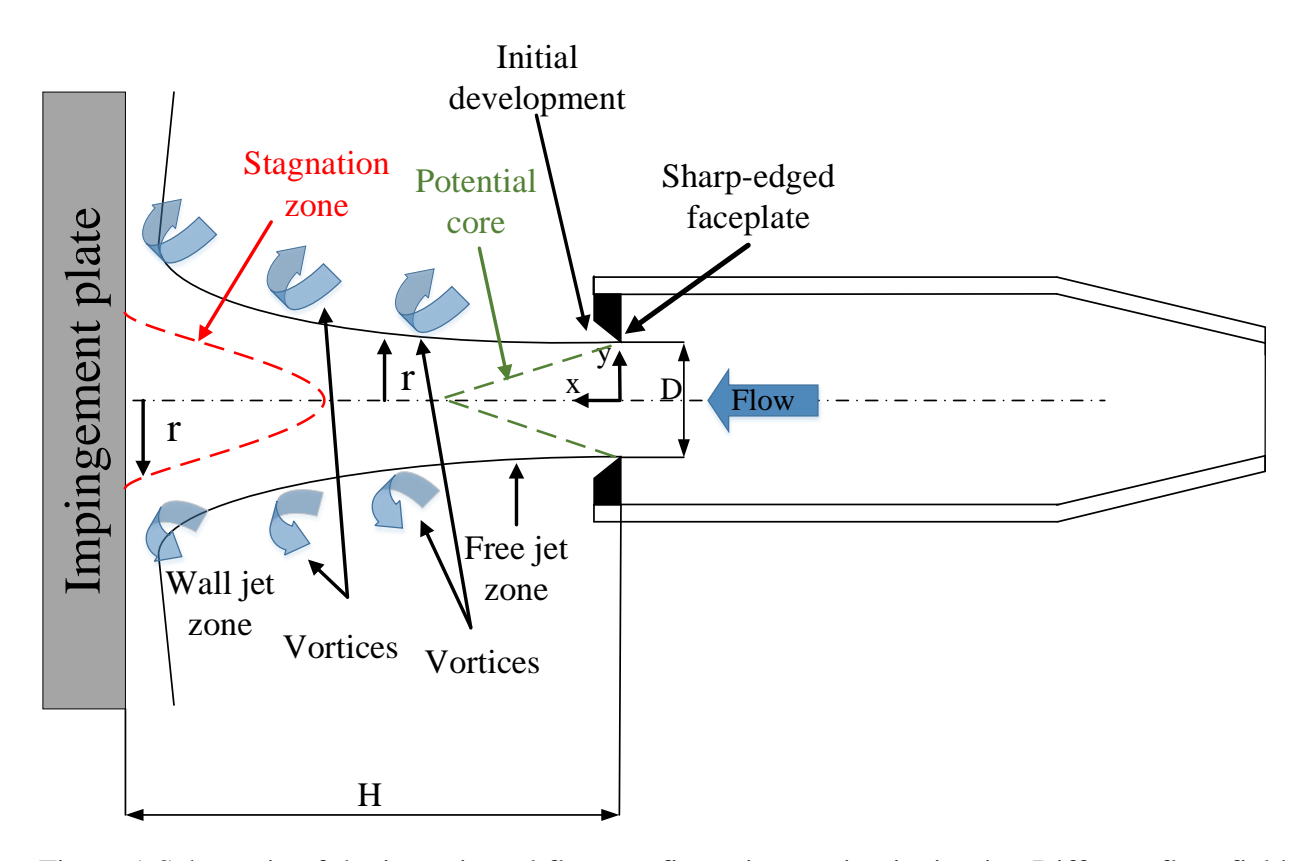


Figure 1 Schematic of the investigated flow configuration: an impinging jet. Different flow-field zones are labeled

1.1 <u>Literature Review</u>

Background for this research is connected to a wide range of studies on natural and forced, free and impinging jets, and heat transfer in impinging jets. The following provides a brief review of these topics as relevant to the present work. First, the background on natural non-impinging and impinging jets is given, followed by a summary of active control of jets with focus on the present jet excitation scheme, employing bi-modal forcing. Finally, a concise review of heat transfer characteristics of impinging jets with and without control of the jet is provided.

1.1.1 Jets: free and impinging

The focus of the present research is on jets emerging from a sharp-edged orifice. The bulk of literature is on jet flows exiting from a contoured nozzle; therefore, the basic jet flow features are first described based on the nozzle configuration. Subsequently, similarities and differences with the sharp-edged orifice jets are discussed. The free-jet flow field can be divided into an initial development zone (very close to the jet lip), a free-jet or a transitional zone (where coherent vortical structures develop from an initial flow instability), and a fully-turbulent zone, farther downstream [1], [2]. The initial and transitional zones extend in the streamwise direction from the jet exit to $x/D \approx 4$, at Reynolds number, $Re_D = U_j D/\nu \approx 1,000$, based on jet diameter and jet exit velocity [2]. As Re_D increases, the extent of the transitional zone decreases, reaching $x/D \approx 0.5$ at $Re_D \approx 200,000$ [2]. The current study is concerned with the development of jets over a domain extending from the jet exit to no more than x/D = 4 at a relatively low Reynolds number of $Re_D = 4,333$. Hence, the focus of the present review is on the initial and transitional zones.

At the start of the initial zone, a shear layer surrounding the jet is created when the flow emerging from the jet exit is suddenly exposed to the surrounding stagnant fluid. The shear layer is initially laminar, then instabilities start to amplify (unstable waves grow) as the shear layer develops farther downstream [1]–[6]. Shear layers are stable to short waves, but they are unstable to waves with much longer wavelength than the shear-layer thickness [3]. This linear instability, which is known as the Kelvin-Helmholtz instability, is associated with exponential growth of the velocity fluctuation with downstream distance. The instability wavelength scales with the initial momentum thickness (θ_i) of the shear layer, hence the wavelength is inversely proportional to the square root of the average jet velocity, when the boundary layer at the jet exit is laminar [1], [5]. The Strouhal number of the instability is experimentally observed to be $St_{\theta_i} \approx 0.012$ [1], [7]–[9],

which is different from the theoretical value of the most amplified instability waves $St_{\theta_i} \approx 0.017$ [9], [10]. This difference can be related to the feedback occurring from downstream events [11]; this will be discussed below.

Farther downstream, the velocity fluctuation level increases and the instability growth becomes non-linear, leading to saturation of the instability amplitude (neutral growth). This behavior is associated with the roll-up of the shear layer into axisymmetric vortex rings. At the location of neutral growth of the initial (fundamental) instability frequency, the subharmonic mode (at half the fundamental frequency) exhibits strong linear growth. In addition, the phase difference between the fundamental and subharmonic modes falls in a certain range [8], which leads to significant growth in the subharmonic via "subharmonic resonance" at a rate exceeding that of linear instability. The growth of the subharmonic component is a key parameter in the mixing layer dynamics, and it has a significant role in the promotion of vortex pairing (merging) [5], [7], [12]. Vortex pairing involves merging of each successive pair of vortices, initially forming at the fundamental instability frequency, to produce a vortex of a larger size at the subharmonic frequency. Thus, coexistence of the fundamental and subharmonic modes is necessary for pairing to occur. The presence of a subharmonic frequency upstream of the vortex pairing location has been found to be connected to acoustic feedback of disturbances to the jet lip from vortex merging. This was confirmed by observing a subharmonic spectral peak at the jet exit [5], [13].

The presence of the jet vortices strongly affects the rate of the shear layer spread into the potential flow bounding the shear layer on the inside (the potential core; see Figure 1) and the outside of the jet. From outside of the jet, the vortices entrain surrounding fluid into the jet and transport this fluid toward the jet centerline along the upstream side of the vortices. On the other hand, the fluid on the inside of the jet is transported away from the jet centerline. Most of the

entrained fluid flows toward the jet centerline and then the vortex rings start to detach from the shear layer [6]. The subsequent spread of the shear layer is mainly produced through successive stages of vortex merging [5] that ultimately lead to the shear layer reaching the jet centerline at the end of the potential core. The potential-core's end location depends on Reynolds number; specifically, the length of the potential core is inversely proportional to Reynolds number [2], [5]. The larger the spread rate of the shear layer, the faster the potential core ends. Beyond the end of the potential core, the jet centerline velocity decays with streamwise distance. The decay rate of this velocity is inversely proportional to Reynolds number [14], [15].

The connection between the transitional (early) development stage of the jet and the fully-turbulent stage is initiated through the instability of the vortex rings. As the vortex rings convect downstream, they start to grow azimuthal waviness and develop higher vorticity. This leads to vortex ring distortion and breakup, hence the generation of small-scale incoherent turbulent structures that ultimately dominate the vorticity field [2], [5]. The details of the vortex instability and breakup are not described further here since the present study is primarily concerned with early development of the jet in the transitional zone.

Another fundamental aspect of the jet instability that is not considered here in detail, is the presence of a second mode of jet instability known as, the jet-column or "preferred" mode of the jet [4], [8], [9]. Unlike the initial Kelvin-Helmholtz instability of the shear layer, which scales on the initial shear layer thickness (θ_i), the preferred mode scales with the diameter of the jet exit. The preferred mode occurs at $St_D = fD/U_j \approx 0.3 - 0.5$, which is the dominant fluctuation frequency found at the end of the potential core in natural jets. The "switch" from an initial to a "terminal" instability of a different character, as the flow evolves from the jet exit to the end of the potential core is explained in [9] to be due to the vortex structure scale becoming limited by the jet

diameter and independent of the initial thickness θ_i around x/D=2-3. The present work takes advantage of the initial shear layer instability, the development of the fundamental and subharmonic modes, and their possible resonance, and the vortex formation and pairing. Therefore, the preferred mode instability, which is fundamental to natural jet development and the control of free jets, is not directly relevant to this study but is mentioned here for completeness.

The sharp-edged orifice jet flow regime is close to that of the contoured nozzle; however, there are some distinct differences between the two jets. In both cases, the flow regions can be divided the same way: initial development zone, transitional zone, and fully-developed or fully-turbulent zone [16], [17]. Very close to the exit, the orifice jet is distinguished with off-center peaks in the mean radial velocity profile, which is not present in the top-hat initial velocity profile of contoured nozzles. Unlike the contoured nozzle, the streamlines of the orifice jet are curved immediately downstream of the jet exit, and the fluid accelerates along the jet centerline. The streamlines curvature is the result of an inward radial velocity component, which leads to the creation of the *vena-contracta* [16], [17]. The streamwise flow acceleration terminates at the vena-contracta, and farther downstream, the lateral spread of the jet is driven by turbulent diffusion of the jet into the surrounding fluid.

The vortex structure development and entrainment of fluid from the surrounding in the orifice jet is similar to that in the contoured-nozzle jet. However, the initial vortex roll-up and the momentum transport are observed to occur at a higher rate for the orifice jet than for the contoured-nozzle jet. Correspondingly, a higher Strouhal number for the preferred mode is found for the orifice jet than that for the contoured-nozzle jet ($St_D \approx 0.7$ for the orifice jet [18]). The higher Strouhal number of the preferred mode in the case of the orifice jet is attributed to the thickness of the initial shear-layer. Specifically, for the same jet exit diameter and Reynolds number, the initial

shear-layer thickness is thinner for the orifice jet, which increases the initial shear-layer instability's frequency [18]–[20]. The thinner shear layer is associated with stronger mean-velocity gradient, higher turbulence intensity, and earlier development of three-dimensionality of the vortex structure [21]. This accelerates the development of the jet towards the fully-turbulent state, which enhances the entrainment and mixing and the shear-layer spread rate in the transitional zone for the orifice in comparison to the nozzle jet [18]. As a result, the potential core length of the orifice jet $(L_{pc} \approx 4D)$ is generally smaller than the contoured nozzle $(L_{pc} \approx 5D)$ [17], [21].

An impinging jet can be described as a free jet with a flat impingement plate located at a distance H downstream of the jet exit at a normal incidence. The flow field can be divided into free-jet zone, stagnation zone, and wall-jet zone, as depicted in Figure 1. The impinging-jet characteristics in the free-jet zone are found to be the same as the free jet, except close to the impingement plate [6], [22]–[24]. Hence, the initial instability frequency is not affected by the presence of the impingement plate when H/D > 1.2 [22], [25], [26]. However, when the jet exit-to-plate distance is of the order of the potential core length, the flow will be affected by the feedback from the impinging flow (via "collective interaction" [20]).

In impinging jets, the flow structure initially develops like a free jet, then the vortex rings approaching the wall start to deform, stretch, and increase in ring diameter. When a jet vortex approaches the impingement wall, the vortex losses the axial convection velocity component and gains a radial convection velocity component [6], [24]. Subsequently, the vortex propagates outwards in the radial direction (i.e. the vortex ring is stretched radially outward by the mean flow convection), causing local separation of the boundary layer beneath the vortex. The separated shear layer rolls up into a counter-rotating secondary vortex, which occurs downstream of the primary

vortex, in the wall-jet region. The secondary vortex forms completely then it ejects away from the wall in the radial domain 1.9 < r/D < 2.3, diminishing farther downstream [24].

1.1.2 Active control and bi-modal forcing of jets

Active control (also excitation or forcing) of a jet has been utilized for a long time to influence the behavior of the jet in order to improve mixing with the surrounding fluid, attenuate acoustic noise emitted from the jet, and/or enhance the cooling effectiveness of impinging jets. Most of these active control methods aim to take advantage of the inherent instabilities of the jet; either the initial shear layer instability, or the preferred mode instability. A detailed summary of many of the literature in this area can be found in the booked titled "Acoustic control of turbulent jets" [27].

Studies of active control of jets predominantly focus on using a single, pure harmonic excitation at the frequency of the initial shear layer instability or the preferred mode. The excitation is produced via acoustic waves from a speaker, mechanical oscillation from a piezoelectric actuator, or unsteady body force from a plasma actuator, among other methods. In the present study, acoustic forcing is utilized to control the jet. Unlike the bulk of the literature, the target of the forcing is not to excite the initial shear layer or preferred mode instability; instead, the present control scheme aims to take advantage of a phenomenon known as subharmonic resonance. Therefore, the forcing requires excitation at the fundamental instability frequency *and* its subharmonic. In the remainder of this section, a review is given of the very few studies found that utilize this type of bi-modal forcing to excite jets. With the exception of one study, which employs an impinging jet, all works pertain to free jets.

Simultaneous forcing at the initial shear layer fundamental frequency and its subharmonic is demonstrated in [7], [28], [29] for a non-impinging jet. These studies showed that the initial

phase shift between the fundamental and its subharmonic has a significant influence on subharmonic resonance, either by enhancement or attenuation, which consequently enhances or attenuates respectively the merging of vortices. Since the shear layer growth is closely connected with vortex pairing, this growth could then be changed significantly through adjustment of the intermodal phase angle (ϕ) in the bi-modal forcing scheme. This offers a degree of freedom in the control approach that is not possible through pure harmonic excitation.

In [7], the maximum attenuation of the subharmonic mode is found at $\phi = 72^{\circ}$, and the best enhancement at $\phi = 150^{\circ}$ when the forcing amplitude is 0.1% for both frequencies. However, when the forcing amplitude is one order of magnitude higher (1%), the peak-attenuation phase shift is found to be 27°, while the enhancement phase shift is found to be 120°. This dependence of the *initial* (imposed) phase on the forcing amplitude is explained in [7] to be related to the fact that the key to subharmonic resonance is not the initial value of ϕ but the intermodal phase at the streamwise location of resonance. When this phase (ϕ_r) is zero, subharmonic resonance, and hence vortex pairing, is enhanced. On the other hand, when $\phi_r = \pi/2$, subharmonic resonance growth and pairing are attenuated. The resonance location is the streamwise location at which the fundamental mode amplitude saturates. This location is inversely proportional to the forcing amplitude and directly proportional to the frequency. Hence, a lower forcing amplitude causes saturation farther downstream, while higher forcing amplitude causes earlier, upstream, saturation [7]. This variation in the resonance location with forcing amplitude translates to different required initial intermodal phase (at the jet exit) to produce ϕ_r at the resonance location if pairing enhancement is desired.

Other prominent studies of bi-modal forcing of non-impinging jets include [12], [30]. Unlike [7], [28], [29], these studies select the fundamental frequency to be the preferred mode.

These works are not discussed further here since the present work makes use of the initial shear layer instability in planning the bi-modal control scheme. It is worth noting, however, that [30] demonstrated that bi-modal excitation can affect the jet flow more strongly than pure harmonic excitation.

One study of bi-modal excitation for the impinging jet is reported in [11]. In this case, forcing is done $St_D=0.8$ and 1.6, where for reference, the initial shear layer instability for the specific flow conditions used corresponds to $St_D\approx 2.25$. Hence, the fundamental frequency does not correspond to either the shear layer or preferred mode instability. The study showed that this bi-modal forcing arrangement enhances vortex pairing in the free-jet zone. On the other hand, forcing at one-third instead of one-half of the fundamental frequency in the bi-modal scheme; i.e. $St_D=0.53$ and 1.6, leads to the merging of three vortices in the free jet zone. In both cases, bi-modal forcing helped to accelerate the formation of larger scale vortices that produced periodic velocity fluctuation above the impingement plate and induce unsteady boundary layer separation. In the study, the amplitude of the fundamental mode is 1% of the jet exit velocity, while the subharmonic mode's amplitude is kept at one-third of that of the fundamental. The intermodal phase difference is not found to affect the results significantly, yet the authors acknowledge that their phase increments might not have been sufficiently small to see the significant phase influence reported in non-impinging-jet studies.

Overall, the studies cited above have demonstrated that bi-modal excitation is more effective than single-frequency excitation in terms of promoting formation of large coherent structures and mixing enhancement, in addition to controlling the near-wall flow for impinging jets.

1.1.3 <u>Heat transfer of natural and forced impinging jets</u>

The jet flow impinging on a wall at normal incidence creates a convective heat transfer distribution that depends on the near-wall flow field. The coherent flow structures, the velocity fluctuation, the unsteady boundary layer separation are all phenomena that can affect the local heat transfer from the wall. The convective heat transfer coefficient h and associate Nusselt number (Nu) on the impingement plate experience a peak at the stagnation point. The heat transfer is directly dependent on Reynolds number, as given by several empirical correlations. However, correlations reported in different studies exhibit significant variation [31]. Two of the widely known correlations are: $Nu_0 = kRe^a$, where $a = f\left(\frac{H}{D}\right)$ and k is a constant, and $Nu_0 = 0.698Re^{0.573}\left(\frac{H}{D}\right)^{-0.116}$ [20], [31]. At $H/D \le 4$, the radial distribution of the local heat transfer experiences two distinguished peaks [32]. Boundary layer separation is reported to be the reason for local heat transfer reduction between the two peaks [26], [32]. Farther out in the radial direction $(r/D \ge 4.5)$, Nu can be solely related to the radial location independent of the nozzle-to-plate distance [26], [31], [32].

Heat transfer from the stagnation zone of the impingement plate increases as the nozzle-to-plate distance increases for $2 \le H/D \le 6$. For larger distances, (H/D > 6), the local heat transfer declines gradually with increasing H/D [33], [34]. The nozzle-to-plate distance where the maximum stagnation heat transfer occurs is found to be the same as the x location where the maximum turbulence intensity is found. Higher turbulence intensity provides higher heat transfer, even after the end of the potential core [31], [35]. It is also observed that increasing the turbulence intensity at the jet exit increases the heat transfer coefficient at the stagnation point [35].

The jet-exit geometry also affects the heat transfer from the impingement plate. Comparing the heat transfer of a jet exiting from a contoured nozzle to a sharp-edged orifice, the Nusselt number exhibits 25% and 20% enhancement at H/D=4 and 8 respectively in the case of an orifice jet [36], [37]. Generally, the orifice jet provides better heat transfer for H/D<10 [31], [38].

When it comes to heat transfer enhancement of impinging jets via flow excitation, studies are only reported for single-frequency forcing. Forcing at the jet's shear-layer fundamental frequency and H/D=1.125 develops intermittent vortex paring, which increases the turbulence and consequently the local heat transfer at r/D=1.75. In contrast, employing a forcing frequency close to the subharmonic frequency reduces the local heat transfer due to more stable vortex pairing and organized flow structures [26].

Another study [39] compares the excited to the unexcited jet at H/D=3. Forcing at $St_D=0.26$ shows heat transfer enhancement at the stagnation zone. However, the forcing also causes Nu to decrease relative to the unexcited jet in the wall-jet zone (r/D>1.5). For $St_D=0.51$, similar local heat transfer to the unexcited jet is observed in the stagnation zone, while the excited jet shows local heat transfer increase in the range 1 < r/D < 2. For $St_D=0.79$, enhancement in the local heat transfer occurs in the stagnation zone. The authors attribute the heat transfer enhancement/attenuation in the heat transfer coefficient at different forcing frequencies to the increase/reduction in the local turbulence intensity due to the forcing.

Two other notable studies are [33], [34]. In these studies, when forcing at $St_D = 2.4$, 3 and 4 for H/D = 2, the stagnation zone does not show differences between the excited and unexcited jet [33], [34]. However, at larger radial locations, in the wall-jet zone, the local heat

transfer is reduced. A slight enhancement is found at a lower forcing frequency corresponding to $St_D = 1.2$ [33]. At H/D = 4, forcing at $St_D = 2.4$ and 3 reduces the stagnation heat transfer with respect to the unexcited jet, due to a decline in the turbulence intensity [26], [33], [34].

Overall, the above studies show that benefits of flow excitation on heat transfer enhancement are mixed. However, none of the studies explored the influence of bi-modal forcing.

1.2 Motivation

As outlined in Section 1.1.3, single-frequency forcing of impinging jets can enhance the heat transfer from the impingement plate by increasing the local level of turbulence. This study is motivated by exploring a different approach for the enhancement of the heat transfer through control of the jet vortex dynamics in the transitional zone. In the work of Aweni [40], he showed that the unsteady surface pressure fluctuations produced on the impingement plate can be particularly intense if vortex pairing occurs while the pairing vortices are convecting parallel to the impingement plate. The intensity of the pressure fluctuation was significantly more than that if a single vortex, whether pre- or post-pairing, interacts with the impingement plate. While pressure fluctuations do not necessarily affect the heat transfer directly, these findings, indicated that wall effects due to vortex-wall interaction in impinging jets can be significantly affected by the stage of pairing when the vortices interact with the wall.

The findings of Aweni [40] motivated a study of the heat transfer in isolated vortex-wall interaction [41], [42]. These authors studied three different scenarios of the interaction: a pair of vortices interacting with the wall as they merge together, one of the vortices interacting alone with the wall, and a single vortex with twice the size and circulation of the latter vortex interacting with the wall. The last two scenarios emulate pre- and post-pairing interactions with the wall, while the first scenario corresponds to "during-pairing" interactions. The results showed that the latter case

results in the strongest heat transfer rate per interaction with the wall, followed by the pre-pairing vortex interaction then the post-pairing interaction. The "during-pairing" interaction, however, also results in the biggest deterioration in heat transfer when unsteady boundary layer separation occurs. Overall, it was not clear if in an impinging jet, the pre-pairing, or during-pairing interactions would provide the best heat transfer. However, [40], [41]clearly show that the ability to control the stage of pairing relative to the wall has a strong influence on the heat transfer due to vortex-wall interaction.

In a natural jet, the stage of pairing relative to the wall is dictated by the initial jet conditions, Re_D and H/D. If these conditions are fixed, one can, however, control the vortex structure evolution relative to the impingement plate by promoting or attenuating vortex pairing using bi-modal forcing (as discussed in Section 1.1.2). The present study is motivated by implementing this idea in an impinging jet and studying its possible effectiveness in enhancing the heat transfer in an impinging jet. Given the novelty of the study, the bulk of the work is focused on understanding the effect of the forcing on the vortex structure development, while the heat transfer aspects only receiving a preliminary consideration.

1.3 Objectives

The specific objectives of the present study may be summarized as follows:

1. Designing and constructing of a new impinging-jet setup with provisions for acoustic excitation of the jet as well as measurements of the convective heat transfer coefficient from the impingement plate. The jet exit geometry is a sharp-edged orifice, which is selected as a canonical (fundamental) flow geometry that represents the impinging jets found in gas-turbine cooling applications better than a jet exiting from a contoured nozzle.

- 2. Conducting flow visualization experiments of the forced jet flow over a range of bi-modal forcing parameters and different H/D values in the range 2-4. The forcing parameters include the forcing level, the amplitude ratio of the two modes and the intermodal phase. The goal of these experiments is to capitalize on the efficiency of flow visualization to examine a wide parameter space, allowing determination of the parameters at which significant change to the jet vortical structures are produced.
- 3. Using the results from the flow visualization investigation, a narrow parameter range is identified for further study using hot-wire measurements. For these studies, hot-wire profiles will be obtained at different streamwise and radial locations to quantify changes produced by the forcing to the statistics of the mean and the fluctuating velocity.
- 4. Implementing experiments to investigate the potential for heat transfer enhancement from the impingement plate in response to the jet forcing over the same experimental parameters range used in the hot-wire experiments. Data from these experiments will be used in conjunction with the flow visualization and hot-wire information to develop hypotheses for the mechanisms of heat-transfer enhancement and attenuation (if any). Due to the time it took to cover objectives 1-3, only limited heat-transfer experiments are carried out as part of this thesis.

The remainder of this thesis is organized as follows. All of the experimental details addressing objective 1 are given in Chapter 2. Results addressing objective 2 are presented in Chapter 3, while Chapter 4 covers presentation and analysis of the hot-wire data. Chapter 5 contains a summary of the limited heat-transfer measurements conducted in this work. Conclusions and recommendations of this thesis are provided in Chapter 6.

CHAPTER 2. EXPERIMENTAL SETUP AND PROCEDURES

The present study investigates the flow of an axisymmetric jet impinging on a flat plate, with preliminary evaluation of the effect of the jet on the heat transfer from the impingement plate. The investigation is carried out for the natural jet and the acoustically forced jet. High-speed time-resolved flow visualization is employed to study the flow structure qualitatively over a range of forcing parameters. Some quantitative information are also extracted from the flow visualization recordings. Additionally, a single hot wire is also utilized to characterize the jet flow and to quantify the effect of forcing on the jet. Limited measurements of the convective heat transfer coefficient from the impingement plate is carried out using TSP (Temperature Sensitive Paint) applied to a heated constant-heat-flux impingement surface. Due to the mirror-like finish of this impingement plate, it is inconvenient to use it for flow visualization. Hence, two impingement plates are used to conduct the experiments with/without the presence of heat transfer. The first setup includes the jet assembly with the flow visualization plate. The second setup includes the jet assembly with the heated plate.

This section contains a description of the components used for the setup of the present research. The setup includes the flow facility (the jet assembly and the impingement plate), and the different instrumentation and diagnostic methods used to run the experiments and acquire data. Also reported here are the procedure used in the different types of experiments. Because the experimental conditions for the heat transfer experiments are not identical to those for the flow investigations (primarily regarding where the acoustic forcing field is measured), the description of the setup and the procedure for the heat transfer measurements are deferred to Chapter 5, where a self-contained coverage of these experiments is provided.

2.1 <u>Jet Facility</u>

2.1.1 Jet assembly

The present investigation is a foundational work for long-term research motivated by the use of impinging jet arrays for cooling of gas turbine blades. To this end, a new facility has been constructed with the aim of facilitating studies of a "minimal" (three-jet) axisymmetric jet array over a range of parameters relevant to gas turbine cooling: Re_D in the range 20,000-70,000, H/D in the range 1-5, and the inter-jet spacing S/D in the range 3-12 [43]. The new jet facility is capable of running with Reynolds numbers up to 21,400, H/D up to 8, and S/D between 3 and 17. The present work, however, is only concerned with a single jet and H/D between 2 and 4. Additionally, given the novelty of the bi-modal jet forcing scheme used in this work, it was easier for the present study to focus on a relatively low Reynolds number (Re_D = 4,233) where the jet vortex structures are expected to remain organized, facilitating interpretation of the flow response to forcing.

Figure 2 shows the main jet facility used in the current project. The main skeleton that carries all the components shown in Figure 2 is made of 80/20 standard aluminum bars with the respective fittings and connections. Air is supplied to the jet facility using a 9.5mm (3/8 ") pneumatic tubing connected to the building's pressurized air supply. The air passes through two flow regulation stages prior to entering the jet housing, one of which is shown in Figure 3, and one flow conditioning stage within the jet housing. A 0.25" standard industrial pneumatic spring coupling is used to connect the pressurized air supply hose to the jet. The air flow rate is set using two valves: the first, a ball valve located at the air supply line in the wall. The flow from this valve passes through a pressure regulator (Speed air 1Z838D 250 psi max) and an air filter (RTi 3CX-020-PX2-FI). The second flow rate setting stage is located just before the air enters the jet. It consists of a high precision pressure regulator (Omega PRG200-60), needle valve (Swagelok SS-

1RF4-SH), turbine flowmeter (Omega FLR1205), and a T-type thermocouple (Omega 5SRTC-GG-T-24-72), as shown in Figure 3. The precision pressure regulator can handle a maximum input pressure of up to 150 psi and output pressure up to 60 psi. The needle valve is used to set the jet flow rate with high resolution. To achieve this, the needle valve is deliberately chosen to have a large number of turns (10 turns) between the fully closed and fully open conditions. The flow exiting the needle valve passes through the flowmeter, which is used to verify the stability of the flow.

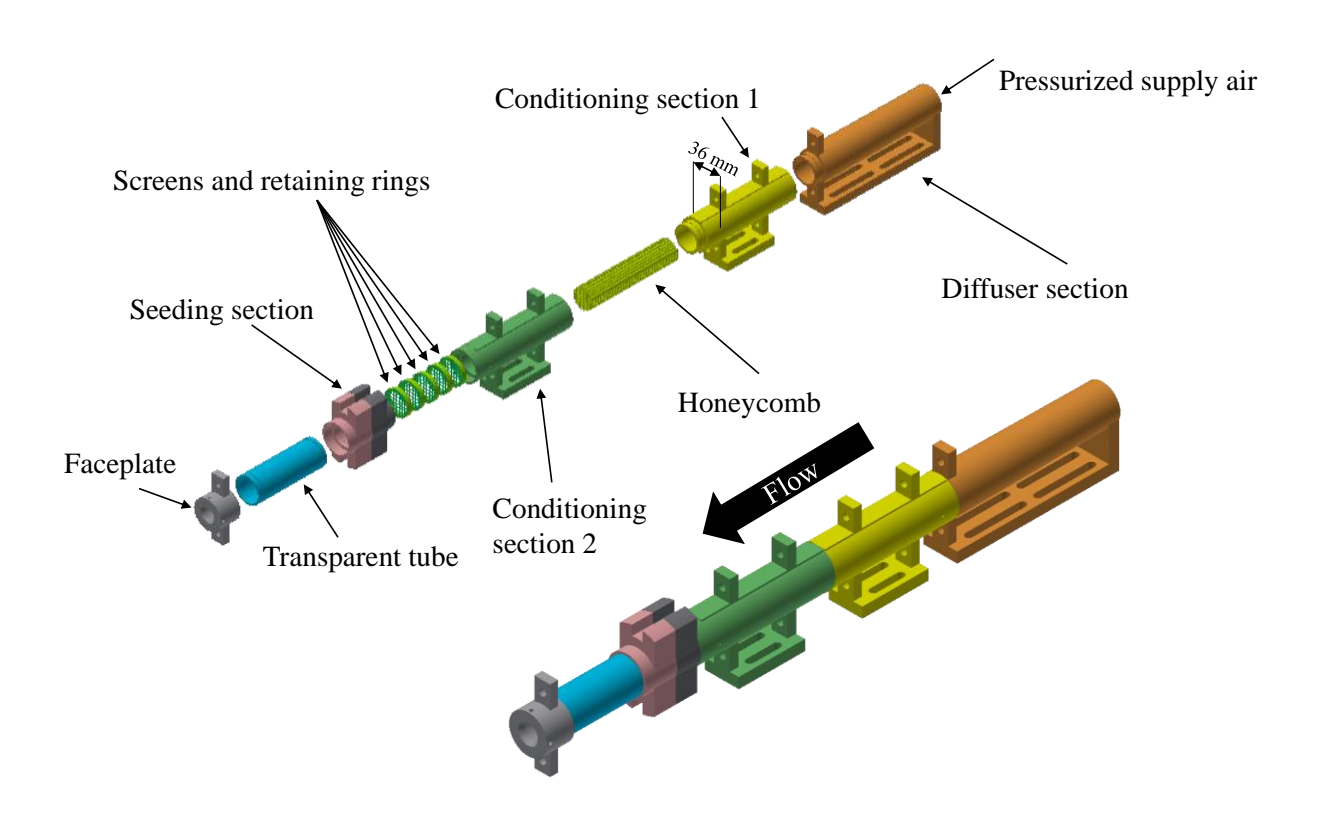


Figure 2 3D drawing of the jet assembly (bottom) and an exploded drawing of the jet components (top). The screens and the honeycombs are colored with the same color as their respective housing

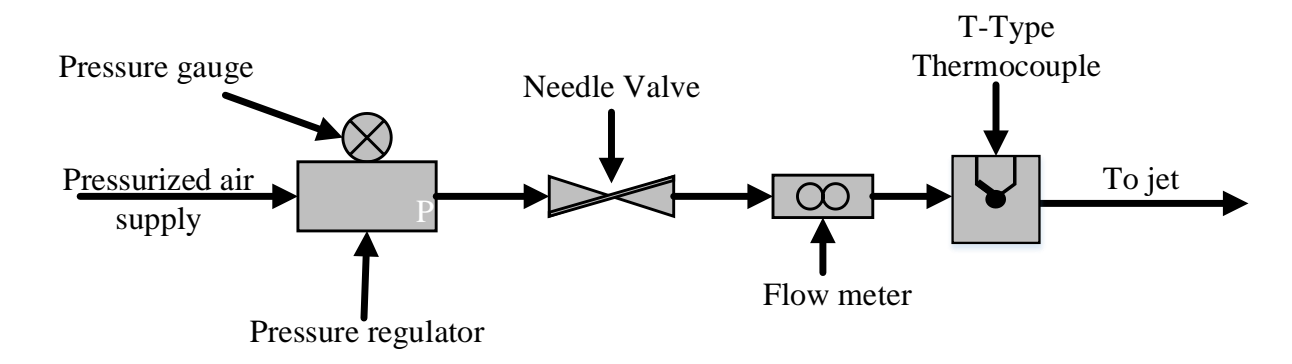


Figure 3 Diagram of the second flow-rate-setting stage

The selected jet velocity corresponds to volume flow rate that is just below the flow meter's specified operating range. Therefore, the average jet exit velocity is determined by measuring the mean streamwise velocity profile at x/D=0 in the cross-stream (y) direction using a single hotwire probe (see Sections 2.2.1 and 2.3.1 for hot-wire measurement details). With the assumption of axisymmetry, the resulting profile is integrated to compute the total flow rate, from which the mean jet exit velocity is obtained by dividing by the jet exit cross-sectional area. This process is repeated several times to iteratively find the required average velocity. The results reported here are conducted at an average velocity of 5 m/s, with an uncertainty of 1%, and a Reynolds number based on diameter at 20 °C (room temperature) of 4,233 with an uncertainty of ± 42

After the air exits the flow meter, the air temperature is monitored using a T-type thermocouple before entering the jet assembly. The range and the accuracy of the T-type thermocouple are ° 0 C to 200 °C and ± 1 °C respectively. In addition to monitoring the temperature of the flow, the second flow-setting stage is employed to reduce the flow fluctuation due to variability in the supply airline pressure. This is achieved with the aforementioned Omega precision regulator, as demonstrated in Figure 4. The left part of the figure depicts measurement of the average jet exit velocity (U_i) using the flowmeter every 10 seconds for a total period of six

hours. Figure 4 (right) displays the same result after removing the mean jet velocity to be able to better see the velocity fluctuation. As shown in Figure 4, the velocity fluctuation is minimal with a value of less than $\pm 0.5\%$ of U_j . Note that the value of U_j in Figure 4 is about 10% higher than 5 m/s in order to fit the jet flow rate within the range of the flow meter for the purpose of the stability test.

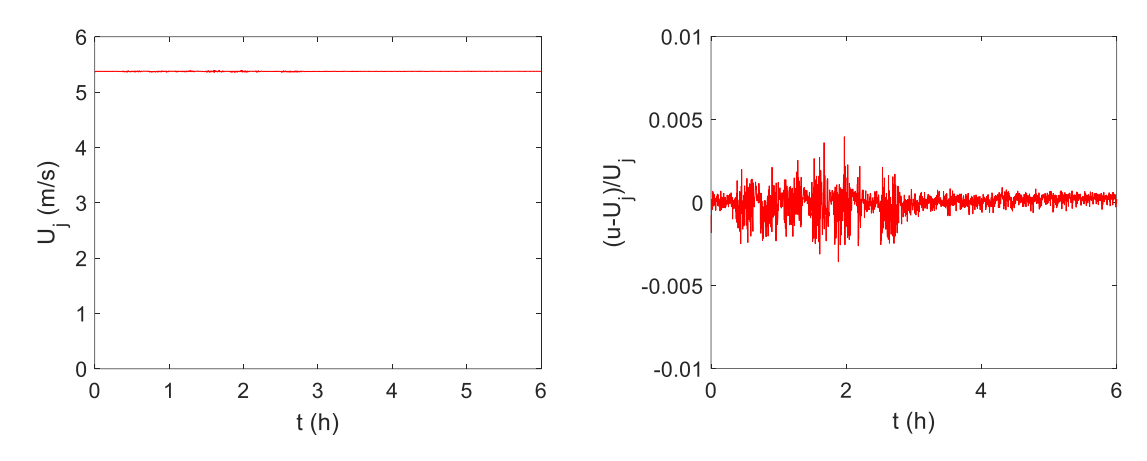


Figure 4 Jet flow stability over a six-hour time span (left). Jet velocity fluctuations for the same test results (right)

The jet components in Figure 2 are modeled and 3D printed at Michigan State University. The flow enters the jet through the pneumatic adaptor attached to the diffuser section. The diffuser section is used to expand the flow cross-sectional diameter from the pneumatic fitting size to the internal diameter of the jet facility (25.7 mm). The outer diameter of the jet facility is 36 mm, which is selected to maintain the rigidity of the facility while allowing a minimum jet-to-jet spacing of S/D = 3 for future jet-array experiments.

The diffuser is designed with a shallow flow area expansion angle (3.1°) to avoid flow separation [44]. Downstream of the diffuser, the air enters the conditioning stage, which consists of two sub-sections: conditioning section 1 and conditioning section 2 (see Figure 2). Conditioning section 1 consists of 3.175 mm (0.125") cell diameter honeycomb that is 114.3 mm (4.5") long. Conditioning section 2 consists of five mesh screens with different sizes, starting with

the coarsest screen nearest to the honeycomb and getting finer toward the Seeding section. The screens mesh sizes are 18×18 , 20×20 , 24×24 , 30×30 , and 35×35 opening per inch square in the direction of the flow, with a wire diameter of 0.4318 mm, 0.4064 mm, 0.3556 mm, 0.3048 mm and 0.254 mm respectively.

The Seeding section is included in the facility to enable careful injection of seed particles into the boundary layer for flow visualization. The Seeding section details are depicted in Figure 5 with a 3D cut-away showing the settling cavity, inlet port, and the injection slit. The 2D cross-section in Figure 5 shows the internal flow diameter and a zoomed view of the injection slit. This section is designed and 3D printed into two parts to allow the removal of the support 3D printed material in the cavity of the Seeding section. The seed particles enter from a port in the grey-colored section (Figure 5), they flow into the cavity between the two parts, as shown in Figure 5, and finally pass to the air mainstream through a 0.7 mm slit inclined at $\alpha = 45^{\circ}$ to the flow direction. The slit has a radius r = 12.85 mm, are angle $2\theta = 80^{\circ}$, which yields are length equal to 18 mm. Tests are made to ensure that the injection velocity of the seed particles is sufficiently low to avoid changing the jet flow dynamics (see Section 2.2.2).

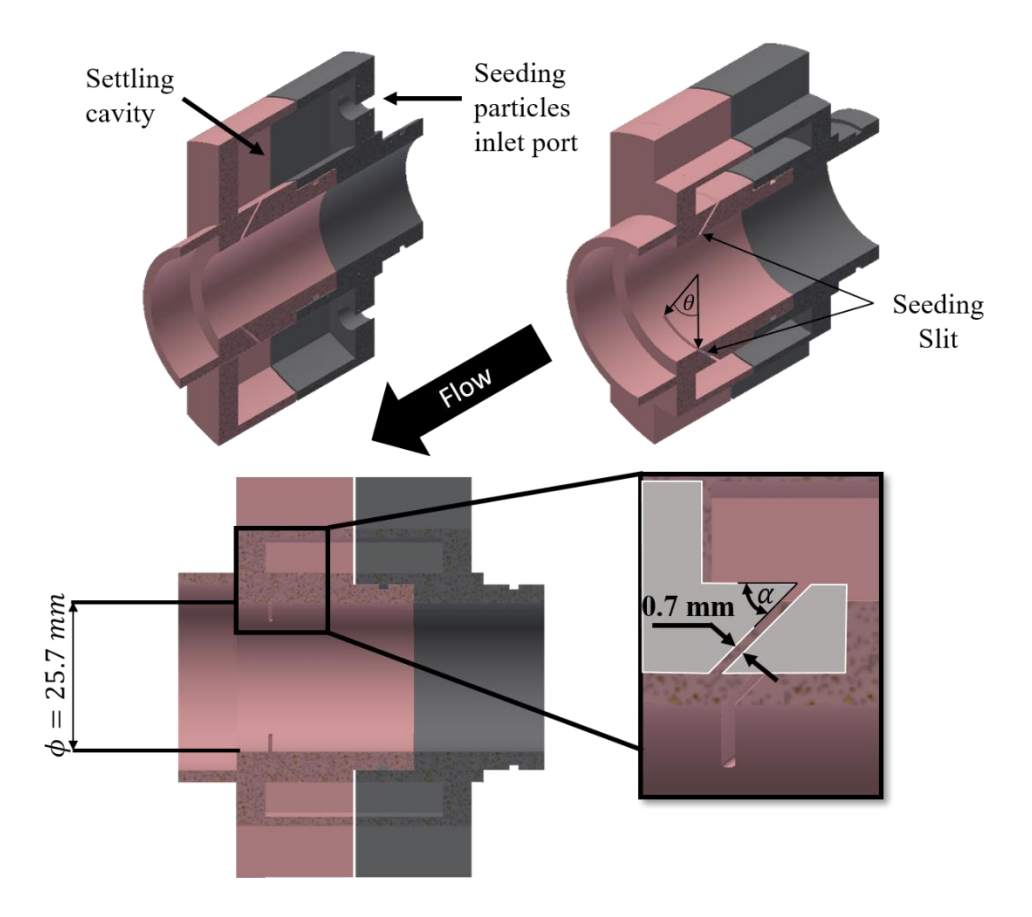


Figure 5 3D and sectional drawings of the Seeding section: 3D section of the seeding particles settling cavity and the inlet port (top left), 3D section showing the seeding particles injection slit and the cavity (top right), 2D section showing the diameter of the jet mainstream and a zoomed view of the slit (bottom)

A transparent plexiglass tube is utilized downstream of the Seeding section. The tube allows any local disturbance from the injection port to die out while enabling visual access to the flow inside the tube as needed. A faceplate section is located downstream of the transparent tube. The section reduces the flow cross-sectional diameter from 25.7 mm to an exit diameter of 12.7 mm (Figure 6) using a faceplate with a sharp-edged round exit. The sharp edge ensures that the jet exit geometry is defined by the exit diameter only and not the thickness of the opening. This geometry is used in literature as a canonical case representing jets emerging from simple opening (as opposed to long pipes or contoured nozzles) such as those used in gas turbine blade cooling. The contraction ratio of the jet (upstream flow area/exit flow area) is 4, which is substantially

smaller than that for typical jet research facilities. This small value, which should result in a higher than usual turbulence intensity at the jet exit, was necessary in order to keep the overall diameter of the jet facility small enough to accommodate inter-jet spacing of at least three jet exit diameters for future studies utilizing jet arrays.

The faceplate section also contains four 2.6 mm counter-bored holes for mounting microphones that are spaced 90-degree apart around the perimeter of the faceplate (Figure 6). The microphone sensing holes are 0.8 mm in diameter and their centerlines are offset minimally (0.4 mm) upstream of the sharp edge of the jet exit orifice. As described in Section 2.2.3, these microphones are employed to measure the acoustic pressure fluctuation used to excite the jet in order to control and quantify the forcing amplitude and waveform.

Two impingement plates are used in this project. The first is used for flow visualization (Figure 7 and Figure 8), is a 9.525mm (3/8") thick polyethylene plate with width and height of 469.9mm and 520.7mm respectively. These dimensions correspond to $37D \times 41D$ respectively. The plate has a black color to minimize light scatter from the surface during visualization. The second impingement plate is used for the heat transfer measurements. Details of this setup may be found in Chapter 5. The jet orientation for all experiments correspond to normal impingement on the plate.

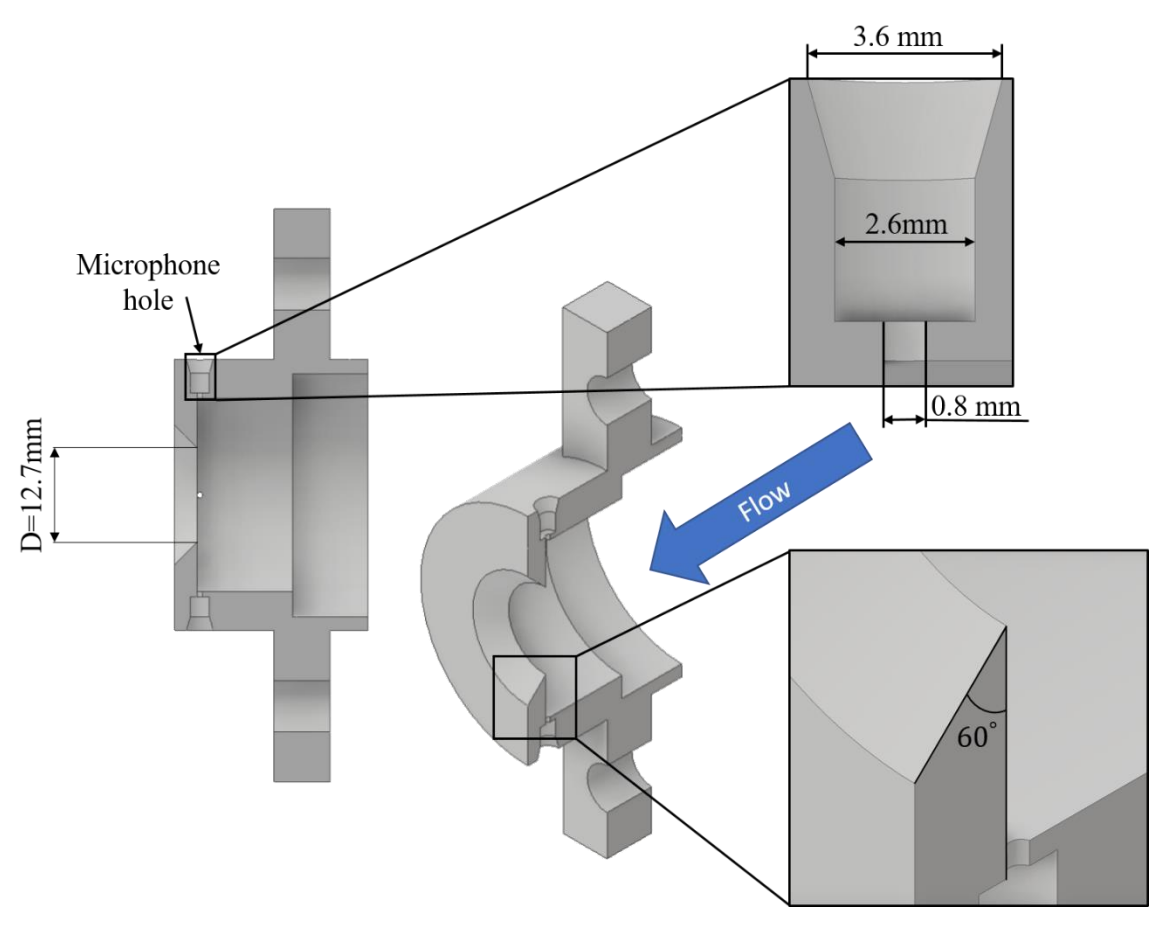


Figure 6 3D sectional drawing of the Faceplate section containing the sharp-edged faceplate and provisions for mounting four microphones around the perimeter of the faceplate

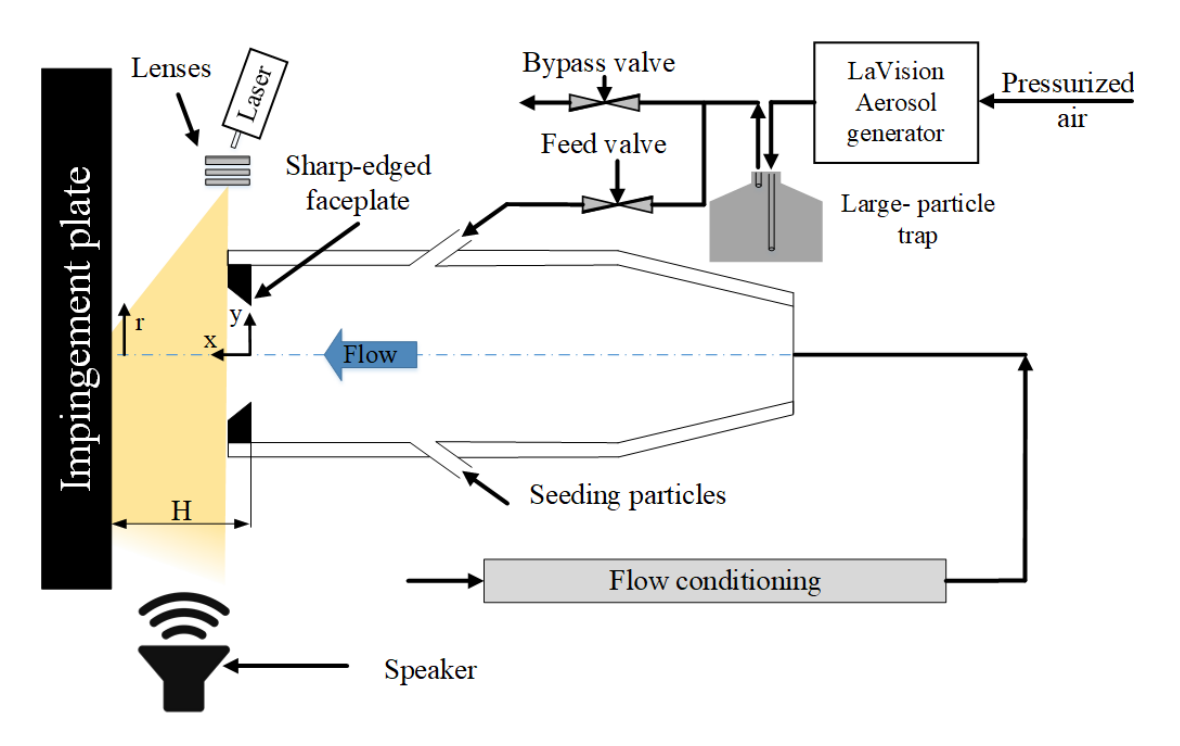


Figure 7 Schematic of the flow visualization setup. The camera used for visualization is directed normal to the plane of the drawing (normal to the page)

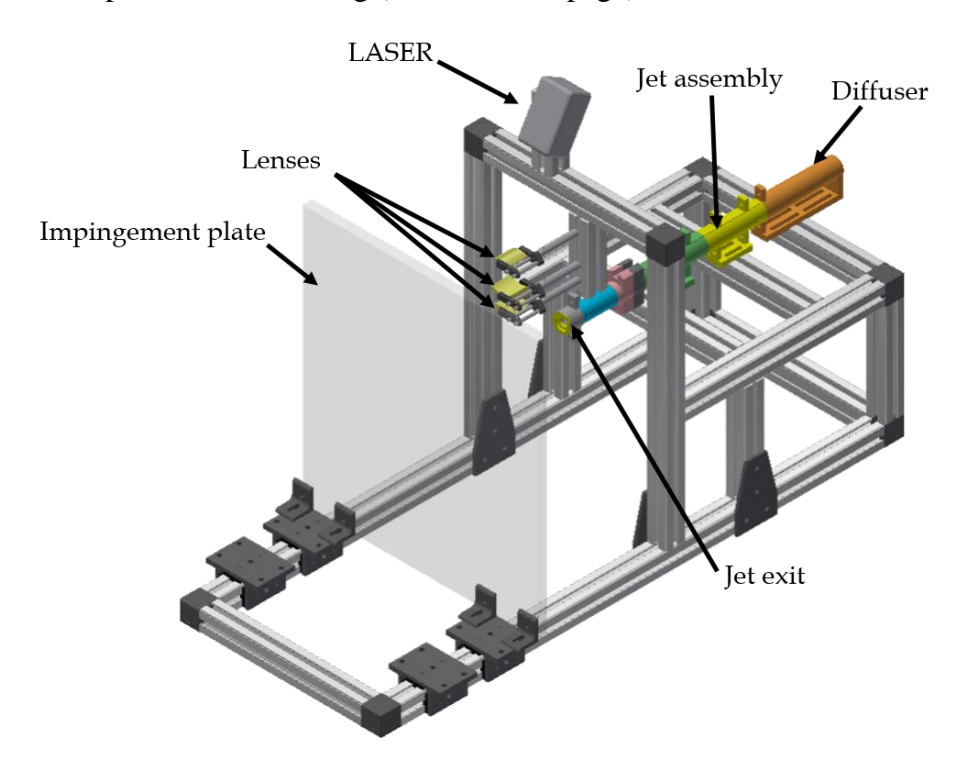


Figure 8 3D drawing for the flow visualization setup, the air inlet is into the diffuser section

2.2 Experimental Techniques

2.2.1 <u>Velocity measurements</u>

A single hot-wire probe is employed to measure the streamwise velocity at different locations in the flow. The hot-wire data are used to: (1) obtain mean and RMS streamwise velocity profiles for the purpose of characterizing the flow of the newly constructed jet facility; (2) verify that the seeding for the flow visualization experiment does not create an unacceptable disturbance to the flow; (3) quantify the effect of forcing on the jet and complement the qualitative flow visualization information.

The hot wire is made of a 5 μ m-diameter tungsten wire that is electro-plated with copper at the wire's two ends while leaving 1mm (0.078D) sensing length of bare tungsten in the middle. The hot-wire probe's typical cold resistance is between 3.5 Ω and 5 Ω including the lead wire and the broaches resistance. The probe lead resistance without the wire is 0.4 Ω . The ratio between the sensing length to the diameter of the wire is 200. The hot wire is connected to a constant temperature anemometer (Dantec mini CTA 54T30) that is set to operate with an over-heat ratio of 0.65, corresponding to a typical wire temperature of 177°C, computed using

(2.1)

$$r_o = \alpha (T_w - T_a) \tag{2.1}$$

Where r_o is the overheat ratio, α is the temperature coefficient of resistance of tungsten, T_w is the wire temperature, and T_a is the ambient temperature. The -3dB bandwidth of the circuit is 10kHz, as stated by the manufacturer and verified using a sine wave test.

To calibrate the hot wire, it is necessary to place it in the jet where the flow is steady, the turbulence intensity is low and the velocity is known. As the sharp-edged jet emerges into the

ambient, its cross-sectional area decreases in the streamwise direction to reach a minimum at the vena-contracta. As a result, the mean streamlines are initially curved and the jet static pressure is above ambient. At the vena-contracta, the streamlines become parallel and the static pressure becomes the same as the surrounding ambient pressure P_{atm} . Thus, by placing the hot wire on the jet's centerline in the potential core at the streamwise location of the vena-contracta (where the turbulence intensity is reasonably low; below 5%), it is possible to determine the flow velocity, using Bernoulli's equation, which leads to

$$U_{vc} = \sqrt{\frac{2(P_s - P_{atm})}{\rho}} \tag{2.2}$$

Where ρ is the air density, P_s is the stagnation pressure at the location of the hot wire, and subscript vc indicates the vena-contracta.

To determine P_s without introducing a stagnation probe next to the hot wire, which would result in significant flow blockage for the relatively small jet diameter, the static pressure upstream of the faceplate P_{static} is measured and used to calculate P_s . P_{static} is measured using a pressure tap inserted into the sidewall of the jet facility upstream of the Seeding section. Using the continuity and Bernoulli equations, the two pressures are related as follows

$$(P_s - P_{atm}) = (P_{static} - P_{atm}) \left(1 - \left(\frac{A_{vc}}{A_{static}} \right)^2 \right)$$
 (2.3)

Where, A_{static} is the cross-sectional area of the jet facility upstream of the faceplate, A_{vc} is the cross-sectional area of the jet at the vena-contracta, and P_{static} is the static pressure upstream of the jet exit. The Area ratio term in (2.3) is not known since the vena-contracta cross-sectional area is unknown. Additionally, this ratio will be influenced by the effect of the boundary layer on A_{static} and the shear layer on A_{vc} . Therefore, $P_s - P_{atm}$ is determined from $P_{static} - P_{atm}$ via

direct calibration. To do so, $P_{static} - P_{atm}$ (which is later used to determine U_{vc}) is calibrated against a pitot-static tube placed on the centerline at the vena-contracta (at x = 1.5D). The calibration implemented at different jet velocities covering the full hot wire calibration range.

Figure 9 shows the pressure tap calibration data points and a linear fit to these points (2.4).

$$(P_s - P_{atm})_{vc} = 1.03(P_{static} - P_{atm}) + 0.14 \quad (Pa)$$
 (2.4)

For a given jet velocity, (2.4) is used to convert the measurement of $(P_{static} - P_{atm})$ to $(P_s - P_{atm})$, which is then substituted into (2.2) to obtain the flow velocity U_{vc} sensed by the hotwire during calibration. $(P_{static} - P_{atm})$ is measured using Validyne pressure transducer (DP15-22) with one of its sides connected with Tygon tubing to the static pressure tap, and the other side is left open to the atmosphere. The range of the pressure transducer is 137 Pa and the sensitivity is 13.48 Pa/Volt. The same pressure transducer is used in all of the pressure measurements implemented in this study.

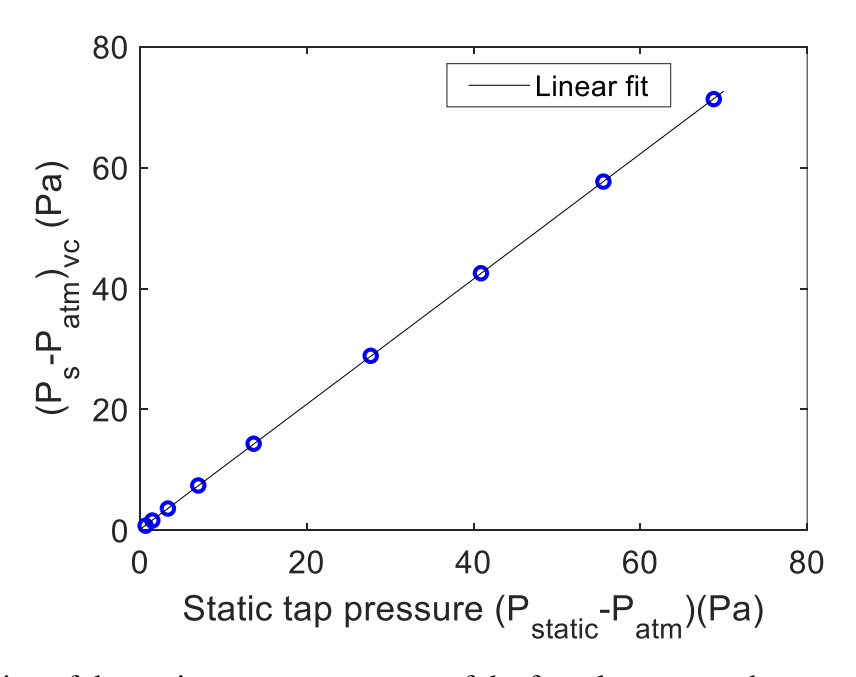


Figure 9 Calibration of the static pressure upstream of the faceplate versus the stagnation pressure in the vena-contracta. Data points (blue circles) and linear fit (black line)

The temperature of the jet flow and the static pressure are acquired simultaneously with the hot wire. The temperature is measured using an RTD temperature probe (Newport 205-MC2) to correct the hot-wire output for any temperature variation between calibration and measurement. The temperature probe is located next to the jet outside the flow field but comparison between this temperature and that measured in the air line shows a maximum temperature difference of 1°C, which is within the accuracy of the airline thermocouple. During calibration, a MatLab code is used to acquire the three signals (hot wire, static pressure and temperature) simultaneously using a 16-bit resolution National Instruments (NI-USB 6343) Analog to Digital Converter (ADC) with the ADC range set to ± 10 V. The sampling frequency and the number of data points for each calibration point are set to ± 10 V. The sampling frequency and the number of data points for each ± 10 V. A total of eight calibration data points are used. A non-linear fit to the data using a built-in function in MatLab ("nlinfit") is employed to calculate the calibration constants in (2.5) (A, B and B) of King's law:

$$E^2 = A + B U^n \tag{2.5}$$

Where, E is the hot-wire output voltage. The calibration constants, together with (2.5), are used to calculate the velocity in subsequent experiments after correcting the hot-wire raw voltage for temperature deviation using (2.6)

$$E_c = E_m \sqrt{\left(\frac{Tw - Tcal}{Tw - Tm}\right)} \tag{2.6}$$

Where, E_c is the corrected voltage, E_m the measured voltage, T_{cal} the air temperature during calibration, T_m the air temperature during measurement, and T_w the hot-wire temperature. The typical range of temperature change between the experiments and calibration is ± 0.5 °C.

The hot wire is calibrated before and after the experiment. The deviation between these two calibrations is typically within $\pm 1\%$. Figure 10 shows an example of a hot-wire calibration comparison. The minimum, maximum, and the mean deviation between pre and post calibrations in this example is 0.55%, 0.79%, and 0.68% respectively.

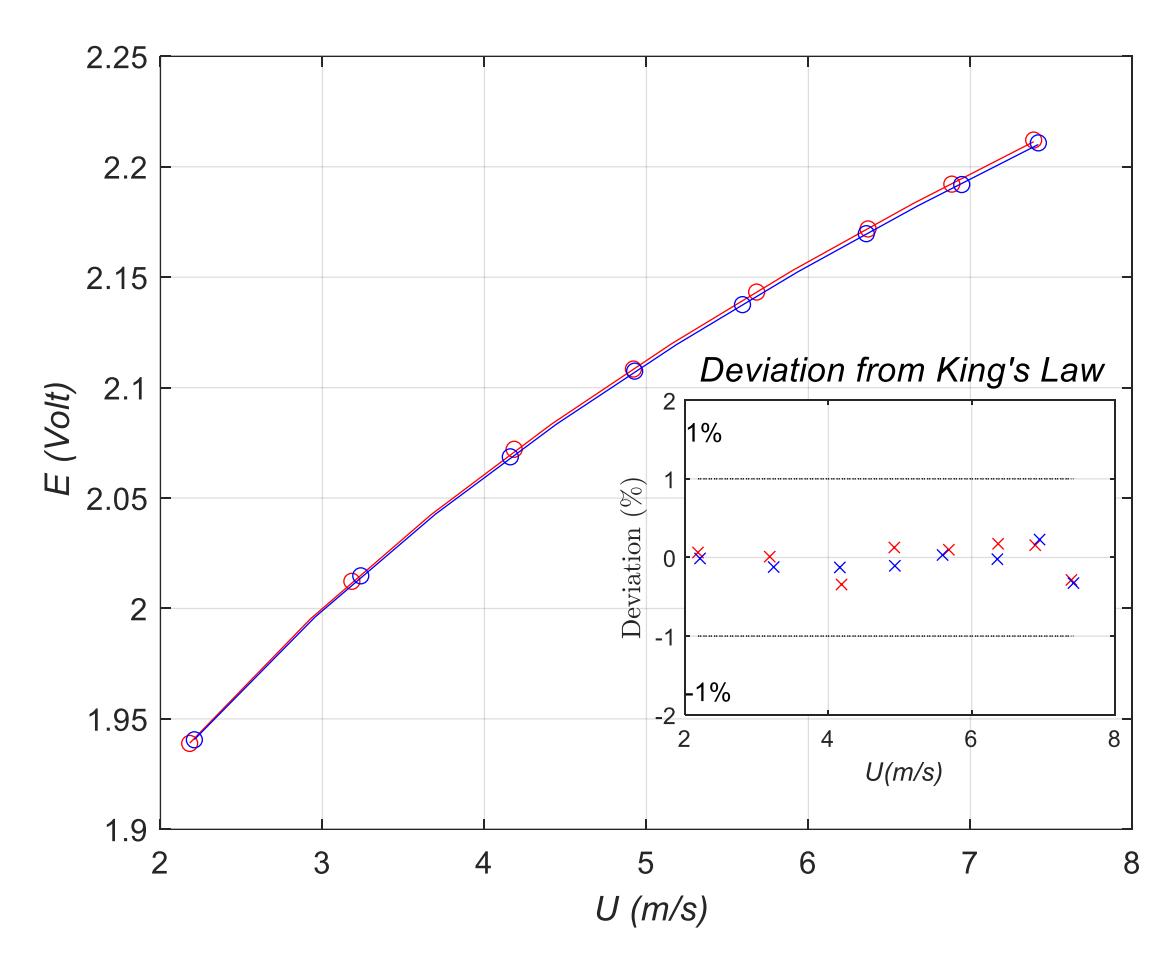


Figure 10 Comparison between hot-wire pre and post calibrations. The red color shows precalibration information and the blue color shows post-calibration information. Circles represent the actual data points, lines depict King's law fit to the data, and x-symbols in the inset show the % deviation of the data from the fit

2.2.2 Flow visualization

The flow-visualization system is sketched in Figure 7. As seen in the figure, Di-Ethyl-Hexyl-Sebacat (DEHS) particles are generated from a LaVision atomizer (model number 1108926) driven by the flow of pressurized air. The typical diameter size of the particles is $1 \mu m$,

as given in the manufacturer specifications. The pressurized air supply is maintained at 8 psi using a pressure regulator (Omega PRG200-60) upstream of the atomizer. After generating the seeding particles, the pressurized air passes through a large-particle trap to catch the large particles and stop them from getting injected into the flow. Then, the flow splits between two gate valves: a bypass valve and a feed valve. The two valves have a visual indicator of the valve opening. For the experiments reported here, the bypass valve is fully open while the feed valve is two-turn open. The bypass valve reduces the seeding stream flow rate into the jet, without affecting the operation of the atomizer. The valves are carefully regulated to test the required seeding injection velocity to provide enough seeding density without disrupting the flow. The seeding particles are confined to a narrow zone near the jet inner wall, consequently, they are primarily concentrated in the shear layer when the jet emerges into the ambient.

The seeding slits are not placed upstream of the conditioning section, to avoid any potential clogging of the honeycomb and the screens. However, by seeding downstream of the flow conditioning section, no means are present farther downstream to attenuate any disturbances that might be introduced by seeding through the wall slits. To verify that the seeding flow is small enough to avoid disturbing the jet flow, hot-wire measurements of the jet flow are conducted to measure the mean and the fluctuating streamwise velocity with and without the seeding flow. When conducting measurements with the seeding flow, the atomizer is drained from the DEHS fluid, so that the same seeding air flow rate is present as during visualization but without the particles. This is done to avoid the disturbance of the hot-wire measurements, or breaking of the wire due to particles striking the wire. Also, when seeding the jet, the pressurized air flow into the jet is reduced to account for the additional volume flow rate due to seeding. This is done by

measuring cross-stream jet velocity profiles at x/D = 0 to ensure that the average jet exit velocity is also 5 m/s with seeding.

In addition to possible disturbance of the jet by the injection of seed particles, another concern is whether the particles follow the flow accurately. This concern is usually checked by computing Stokes number $Stk = \tau u/l$ (where, τ is a characteristic particle response time to the flow drag force, u is a characteristic velocity scale of the flow (U_i) , and 1 is a characteristic length scale of the flow, D). With the current particles having a diameter of 1 µm, the Reynolds number of the particle is less than unity, which makes the particle in the "Stokes regime" and $\tau = \frac{\rho_p d_p^2}{18\mu} \rightarrow$ $Stk = \frac{\rho_p d_p^2 U_j}{18\mu D}$; where, ρ_p and d_p are the particle density and diameter and μ is the dynamic viscosity of the air. The resulting Stk value is of order 10^{-3} , which is much less than unity, confirming the particle's ability to follow the streamlines. This can also be expressed differently through the bandwidth corresponding to the ability of the particle to follow different frequencies of oscillation in the flow. This bandwidth is expressed as $f_c = \frac{1}{2\pi\tau}$, or $f_c = 56kHz$. This is more than an order of magnitude higher than the highest frequency of interest in the present flow (1000 Hz), alleviating any concerns about the ability of the particles to follow the flow in the flow visualization study.

Figure 11 shows the mean velocity profile in the y direction with and without seeding for $U_j = 5 \text{ m/s}$ ($Re_D = 4,233$) and x/D = 0, 0.059, 0.118, 0.275, and 0.5. The y coordinate is plotted in the figure relative to the centerline of the jet; i.e. $y - y_{cl}$. The centerline coordinate is determined by finding the point that will show similar profiles between the top and the bottom portions of the profile. Qualitatively, the profiles look similar with a uniform-velocity potential-core region bounded by shear regions on top and bottom. The RMS profiles (Figure 12) also agree

well with and without seeding (except for some deviation at x/D = 0.275). The profiles closer to the jet exhibit only one RMS peak (at negative y values) due to the practical difficulty of profiling the whole jet exit at a very close distance to the jet lip.

To make quantitative comparisons regarding the effect of seeding on the flow, several shear layer characteristics are computed. The 99% shear-layer thickness (δ_{sl}) is estimated as the thickness over which U/U_j changes from 0.1, on the low-speed side, to 0.99, on the high-speed side. The 0.1 threshold set on the low-speed side is used to avoid hot-wire signal rectification errors due to the possible presence of reversed flow at the edge of the jet. Table 1 shows a comparison between δ_{sl}/D with and without seeding at different locations, which is determined with a resolution (data spacing) error of 0.01D. The non-dimensional maximum velocity gradient $dU/dy \times D/U_i$ values are also included in the comparison in Table 1.

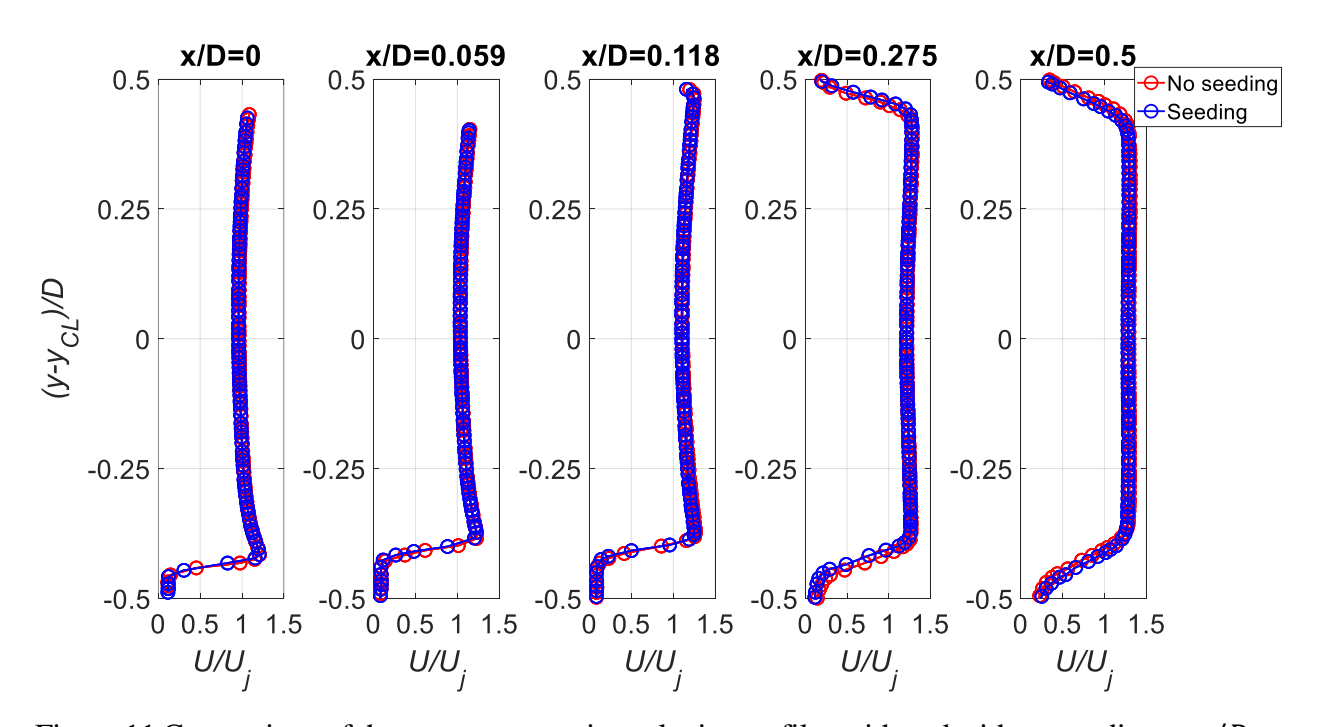


Figure 11 Comparison of the mean streamwise velocity profiles with and without seeding at x/D = 0, 0.059, 0.118, 0.275, and 0.50

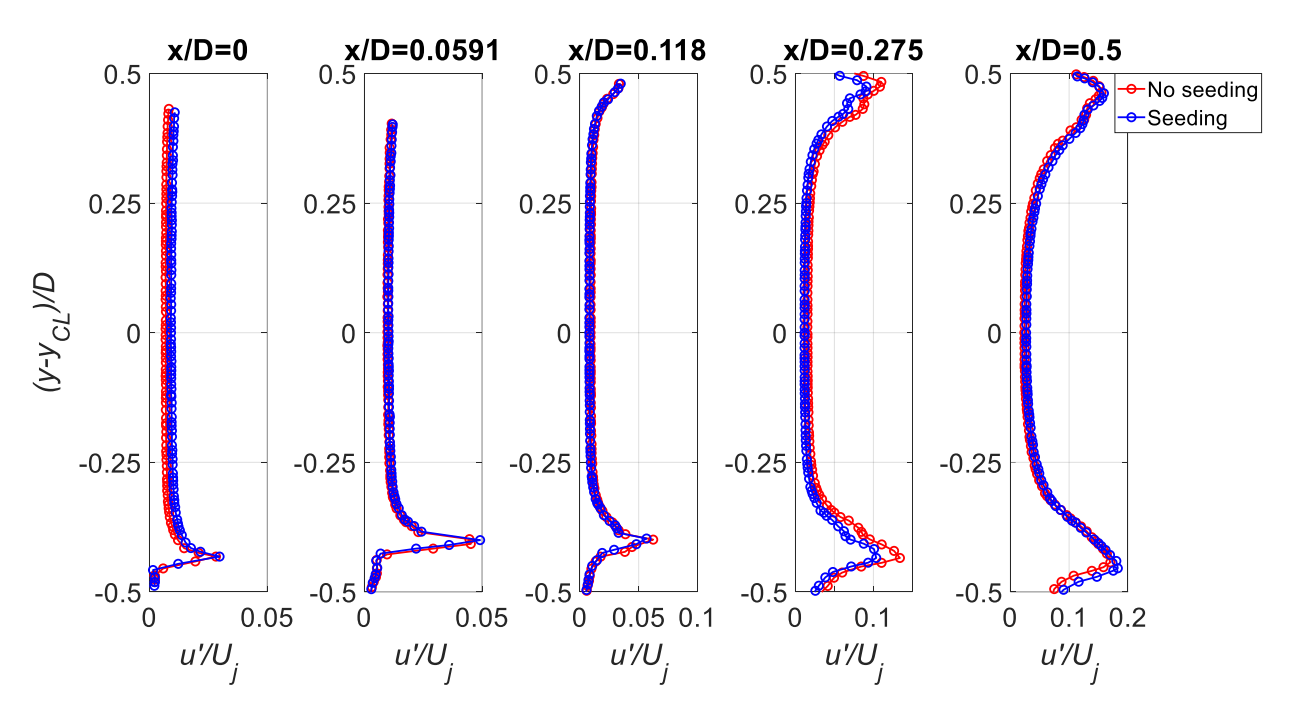


Figure 12 Comparison of the RMS streamwise velocity profiles with and without seeding at x/D = 0, 0.059, 0.118, 0.275, and 0.50

Table 1 Shear layer thickness and normalized gradient comparison

	$\frac{x}{D} = 0$	$\frac{x}{D} = 0.059$	$\frac{x}{D} = 0.118$	$\frac{x}{D} = 0.275$	$\frac{x}{D} = 0.5$
$\frac{\delta_{sl}}{D}$ (without seeding)	0.029	0.039	0.039	0.108	0.187
$\frac{\delta_{sl}}{D}$ (with seeding)	0.029	0.039	0.039	0.088	0.216
$\frac{dU}{dy} \times \frac{D}{U_j} $ (without seeding)	42.63	32.72	38.11	22.44	15.02
$\frac{dU}{dy} \times \frac{D}{U_j} \text{ (with seeding)}$	43.66	37.18	37.54	24.44	14

In addition to checking the mean and RMS velocity profiles, it is important to verify that the jet dynamics have not changed with the introduction of seeding. One indicator of this is that the jet vortex passing frequency remains unchanged in the presence of seeding. In the present study, this frequency is determined from analyzing the power spectrum Φ of the streamwise

velocity fluctuation obtained at the y location of the maximum RMS (Figure 13). The normalized spectrum is plotted versus Strouhal number ($St_D = fD/U_j$; where f is frequency in Hz) for the cases with and without seeding. The spectra show a dominant peak fundamental frequency around $St_D = 2.54$ (1000 Hz) at all streamwise locations, the dominant fundamental frequency is pointed out with the vertical red broken line, while the subharmonic frequency is pointed with the vertical green broken line (Figure 13). The dominant fundamental frequency corresponds to the initial vortex development of the jet. The spectra at different streamwise location show good agreement between the flow with and without seeding, which depicts minimal influence from the seeding particles on the jet characteristics. The different dominant frequencies at different streamwise location and the vortex pairing will be discussed later in presenting the results for the flow visualization (CHAPTER 3) and the hot-wire measurement (CHAPTER 4).

Spectra on the jet centerline are also inspected. The centerline spectra show a peak around the same frequency as the shear layer ($St_D = 2.54$, 1000 Hz). The comparison between the flow with and without seeding shows similar behavior at all x/D locations (Figure 14).

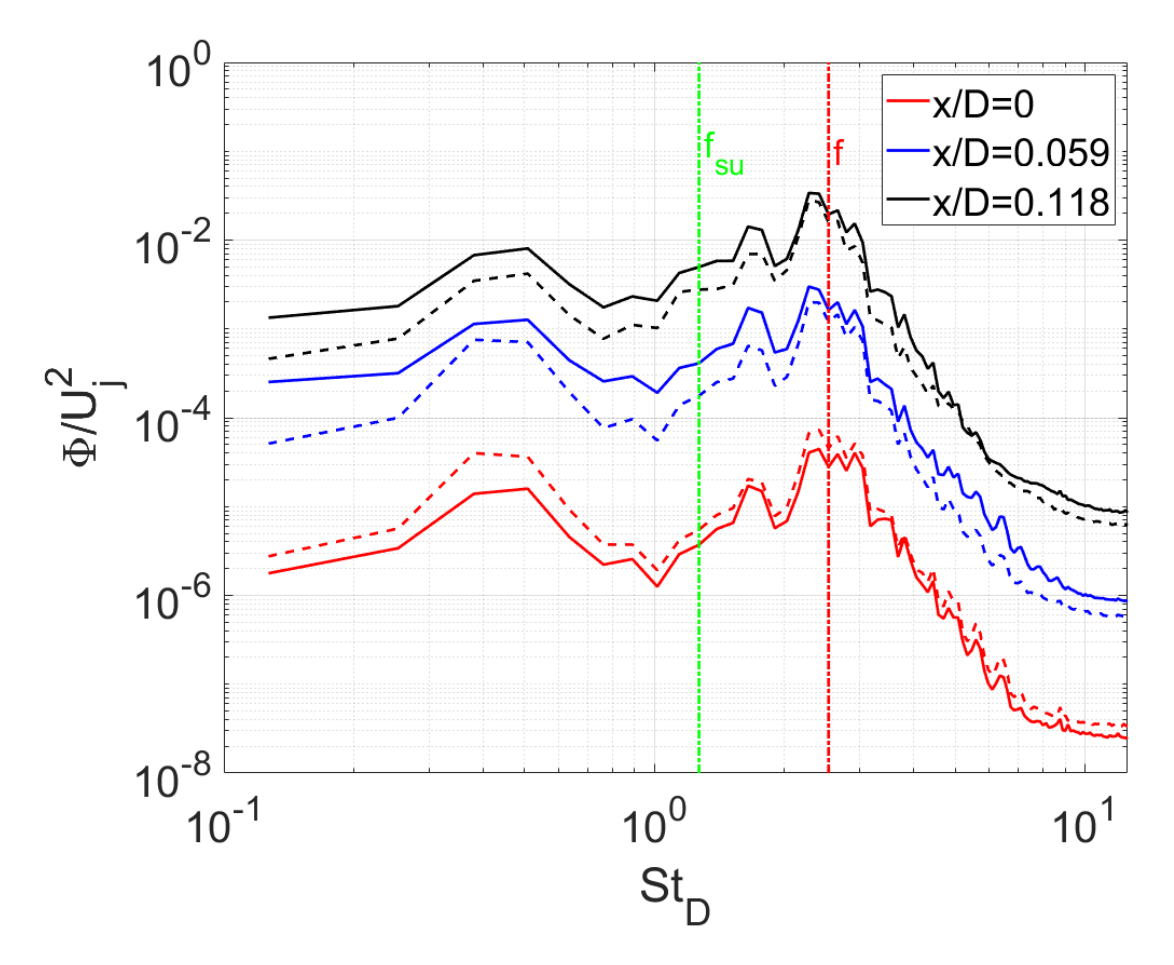


Figure 13 Comparison of the normalized spectra at the y-location of the RMS peak of the lower shear layer at different x/D locations without and with seeding. Solid and broken lines show results without and with seeding respectively (spectra at successive x-locations are shifted by one order of magnitude from each other to avoid clutter)

The seeded flow exiting through the sharp-edged orifice is illuminated using a 4.5-Watt LED three-color (RGB) laser (Laserland W4000) that is shaped into a laser sheet. To maximize the illumination energy, all three colors are used simultaneously. To form the laser sheet, a set of lenses is used to reshape the initially rectangular laser beam. The first lens (Thorlabs - LJ1403L1-A) is a convex cylindrical lens (focal length=60 mm) that focuses the laser in the direction normal to the visualization (x - y) plane. The second lens is a cylindrical concave (focal lens= -50 mm), placed with its focal point coincident with the location where the laser is focused by the first lens. This leads to the beam emerging collimated with the desired thickness in the direction normal to

the visualization plane. The selection of the focal lengths of the first two lenses is set to achieve the desired laser sheet thickness within the available space in the experiment. The third lens has the same specifications as the second lens, however it is rotated 90 degrees in order to diverge the laser sheet in the streamwise direction to completely illuminate the field of view of interest. Over the visualized area, the average thickness of the laser sheet is 0.5 mm. The flow can be illuminated up to x/D = 4 depending on the location of the impingement plate.

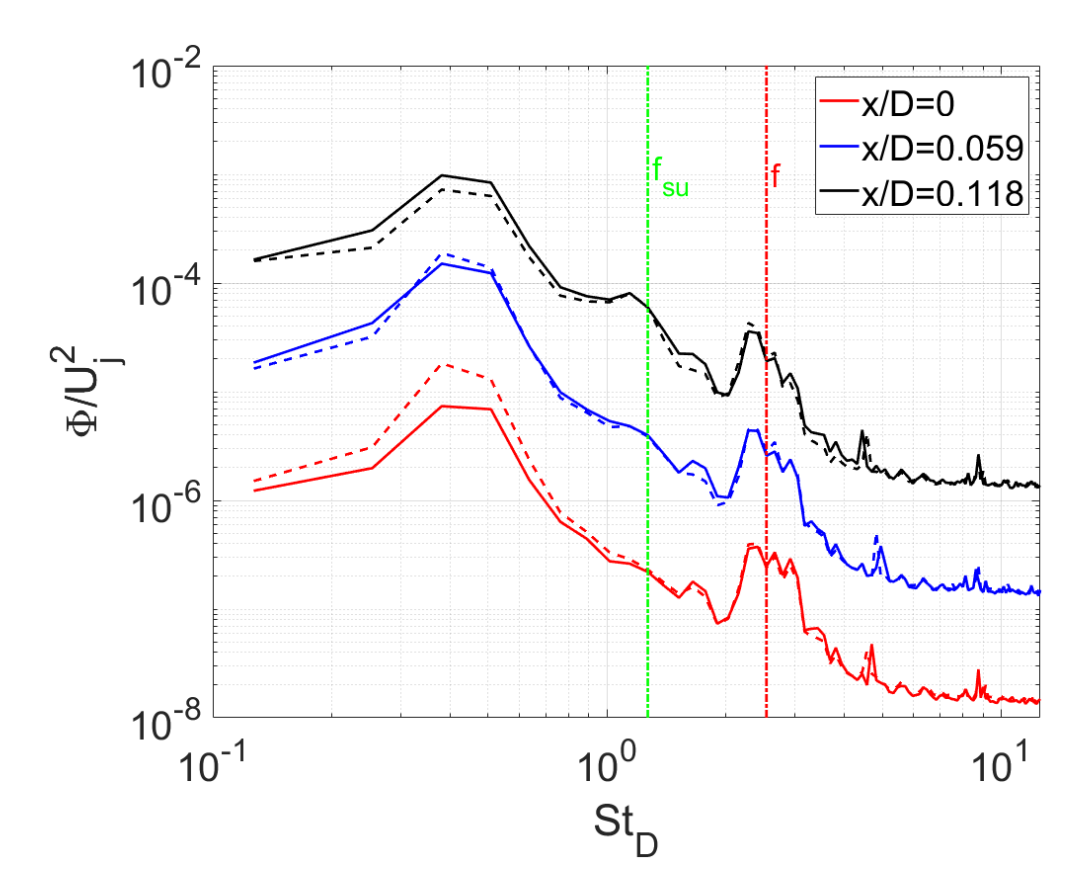


Figure 14 Comparison of the normalized spectra at the centerline at different x/D locations without and with seeding. Solid and broken lines shown results without and with seeding respectively (spectra at successive x-locations are shifted by one order of magnitude from each other to avoid clutter)

A high-speed CMOS 12-bit monochromatic camera (Phantom V2512) capable of capturing up to 25,700 fps is used to acquire time-resolved flow visualization images with 60mm lens (f/1.2). The camera has 1280×800 -pixel sensor which is exposed to a field of view of 22mm \times 50mm,

in the x and the y direction respectively. This field of view is equivalent to 1.7D \times 4D at H/D = 2. The imaging scale is calculated by determining the number of pixels across an image of a scaling grid. For all images, the scale is found to be 0.127 mm/pixel (0.01D/pixel).

A frame rate of 10,000 fps is used to capture the images in this work with an exposure time of 99.525 μ s. This frame rate provides 20 or 10 frames per cycle with respect to the subharmonic or the fundamental frequency respectively. During the exposure time of acquiring the images, the seeding particles travel 0.497 mm (0.04D) at 5 m/s. Figure 15 provides an example for an instantaneous flow visualization image for the natural jet and H/D=2.

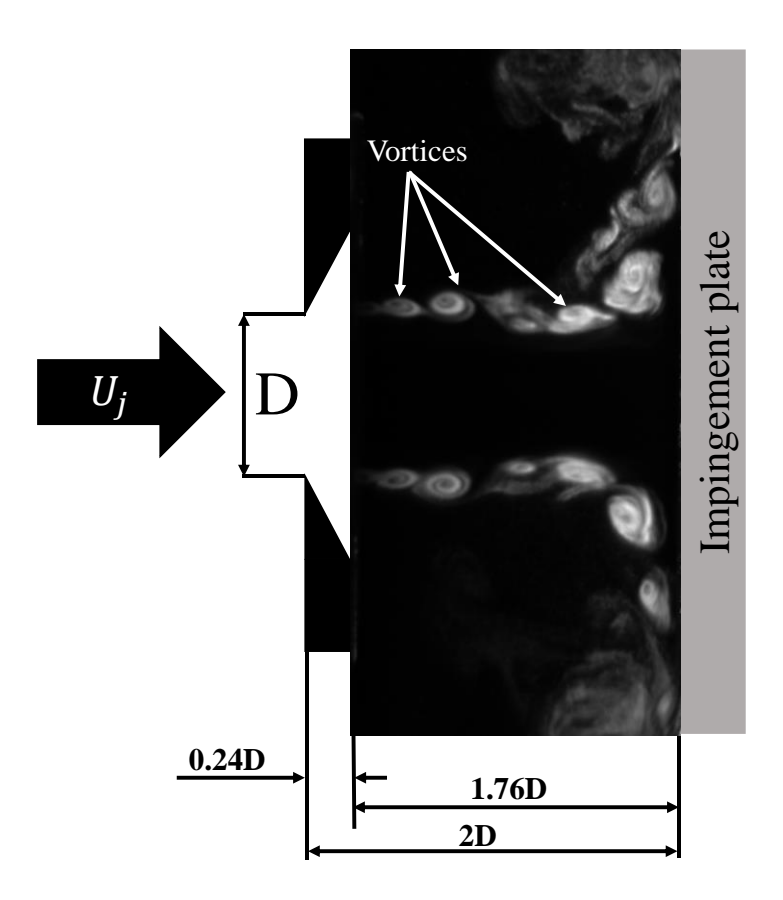


Figure 15 Instantaneous flow visualization example for the natural jet at H/D=2

2.2.3 Forcing of the jet flow

Bi-modal acoustic forcing is employed to control the flow structure of the impinging jet. The forcing frequencies are chosen to be the initial instability frequency of the jet shear layer (fundamental frequency f) and its subharmonic f_{su} . The acoustic pressure forcing signal maybe expressed as follows:

$$p'(t) = a_f \sin(2\pi f t) + a_{f_{su}} \sin(2\pi f_{su} t + \phi)$$
 (2.7)

where, a_f and a_{fsu} are the acoustic forcing amplitudes at the fundamental and the subharmonic frequency, respectively, ϕ is the phase shift between the two modes (where $0^{\circ} \leq \phi < 180^{\circ}$), and t is time. The bi-modal signal is periodic in ϕ with a period of 180° (corresponding to one full period of the fundamental frequency and half period of the subharmonic). Hence, intermodal phase values outside the interval $0^{\circ} - 180^{\circ}$ do not produce acoustic pressure signatures different from those generated within the interval.

To find the initial instability frequency, hot-wire time series of the streamwise velocity at the center of the shear layer (the y location of maximum u') are used to obtain the fluctuating velocity spectrum. These measurements are done sufficiently close to the jet lip where the initial instability is developing yet upstream of where other lower frequencies arise from successive vortex pairings. The spectra, given earlier in Figure 13, show a prominent spectral peak at $St_D = 2.54$ (1000 Hz). This is the earliest spectral peak to develop and hence is identified as the fundamental shear layer frequency. Both peaks are identified with a vertical broken line in Figure 13. It is noteworthy that a third peak is seen in the spectra at $St_D \approx 0.4$. This peak believed to be related to possible flow unsteadiness driven by corner separation behind the faceplate. This will

be discussed further when examining detailed streamwise evolution of the velocity spectra in Chapter 4.

In the present work, the overall amplitude of the acoustic disturbance p', the forcing frequencies, and $AR = a_f/a_{fsu}$ are maintained fixed, while ϕ is varied over its full range to investigate the effect of the intermodal phase shift on the flow structure. Two acoustic velocity amplitudes are tested: 0.3% and 0.1% of U_j . The former corresponds to sound pressure level SPL = 110 dB and the latter to 90 dB. With the specific speaker used for forcing, it was not possible to force at a higher SPL level without distorting the generated sound (i.e. producing undesired higher harmonics). At the higher forcing amplitude, three AR values of 0.5, 1, and 2 are examined for an impingement plate location of H/D = 2. Only the higher forcing amplitude and AR = 1 are utilized to test H/D = 3 & 4. A summary of the cases tested and experiments conducted can be found in Table 2 and Table 3 in Sections 2.3.1 and 2.3.2.

The forcing signal is created in MatLab using a program that also controls the Digital to Analog Converter (DAC) used to output the signal. The bi-modal signal (which has a periodicity of 500 Hz; the subharmonic frequency) is digitized with an output frequency of 90 kS/s; thus, giving 180 points per cycle. The DAC (NI-USB 6343) has an output range of ± 10 Volt and 16-bit DAC resolution. The DAC output is connected to a Crown sound amplifier (XTi 2002) with 475 W power in stereo setting (current setting) and 1600W in the bridge setting (Figure 16). The amplifier drives an Eminence audio sub-woofer (Delta Pro-8A) with a usable frequency range that falls between 100 Hz and 3 kHz and initial impedance of 8 Ω . The speaker is placed outside the jet flow with its centerline normal to the jet centerline at r/D = 36.5 (as seen in Figure 7 and Figure 8). This "transversal orientation" of the speaker is reported to lead to axisymmetric development of the forced jet when the jet emerges from a sharp-edged orifice [27]. The same is

not true for jets emerging from a nozzle, where distortion of the jet axisymmetry is seen due to different development of the jet in the x-y versus x-z planes (see [27] for more details). It is noteworthy to mention that for the highest frequency contained in the forcing signal (1000 Hz), the sound wavelength (λ_a) remains significantly larger than the jet exit diameter $(\lambda_a/D \approx 27)$.

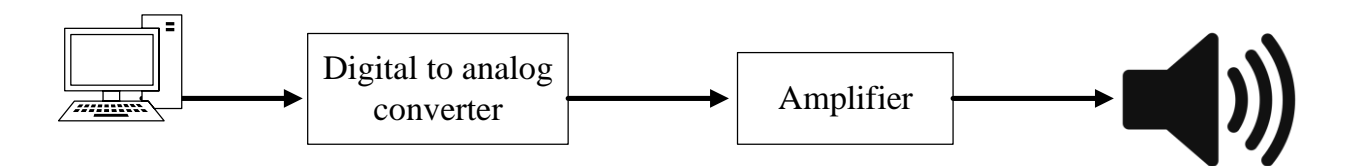


Figure 16 A diagram of the acoustic forcing system

Four Knowles (FG-23629-P16A) microphones with an external diameter of 2.6 mm and sensing hole diameter of 0.8 mm are fitted around the jet perimeter just behind the faceplate exit in the holes indicated in Figure 6. These microphones are used to measure the forcing acoustic pressure level in the "same" plane as the sharp edge of the jet, where environmental acoustic disturbances are known to be converted into hydrodynamic shear layer disturbances via the receptivity process. Additionally, the microphones are employed to check the axisymmetry of the acoustic forcing field. These microphones are used because of their exceptionally small size that allows to place them as close as possible to the sharp edge plane of the jet. They are also known to have a flat frequency response between 100 Hz and 10kHz and a nominal sensitivity of 22.4 mV/Pa. However, the microphones are not individually calibrated by the manufacturer and individual units may have a sensitivity that differs from the nominal specifications. Therefore, it is necessary to calibrate the Knowles microphones.

A Brüel and Kjær (B&K) ¼" microphone (model 4938-A-011) connected to B&K 2690-0S power and signal conditioning unit is used to calibrate the faceplate microphones using white noise produced from a function generator (Agilent 33120A). The bandwidth of the B&K

microphone is 3Hz-70kHz and its sensitivity (including an amplification factor on the conditioning unit) is 10 mV/Pa. The calibration of the Knowles microphones is done when the calibration B&K microphone is inserted 4.25 mm into the jet from the jet lip along the jet centerline.

To calibrate the faceplate microphones, the signal is acquired with and without the white noise, to subtract the background noise from the actual created signal. The calibration provides the frequency response of the microphone; i.e. the dependence of the microphone sensitivity and phase delay on frequency. Specifically, the complex response (including real and imaginary components) is given by:

$$S_x(f) = K(f)e^{i\psi(f)} = \frac{\Phi_{xy}(f)}{\Phi_{yy}(f) - \Phi_{nn}(f)}$$
 (2.8)

where, K(f) and $\psi(f)$ are the sensitivity and phase frequency response of the x Knowles microphone. Φ_{xy} is the cross spectrum between the Knowles and B&K microphones signals in Volt and Pa, respectively. Φ_{yy} is the power spectrum of the B&K microphone signal in Pa² and Φ_{nn} is the background noise power spectrum measured by the B&K microphone in Pa² when the white noise calibration source is turned off.

The calibration is valid at frequencies where the coherence between the Knowles and the B&K microphone signals is high. The coherence is computed using

$$\Gamma_{xy}(f) = \frac{|\Phi_{xy}(f)|}{\sqrt{\Phi_{xx}\Phi_{yy}}}$$
 (2.9)

where, Φ_{xx} is the power spectrum of the Knowles microphone signal. Γ_{xy} varies between 0 and 1, where 0 represent no coherence between the two signals and 1 perfect coherence. The cross and power spectra are calculated from 1.8×10^5 point long time series that are acquired at a sampling frequency of 20 kS/s. The time series are divided into 225 records, each record consists

of 8000 points, yielding a frequency resolution of 2.5 Hz and random uncertainty of 4.7%. The cross spectrum is computed by taking the fast fourier transform (FFT) for each record, and multiplying the FFT of the faceplate microphone signal by the calibration microphone signal FFT complex conjugat. The result of all records is averaged to obtain the final cross spectrum. The same approach is utilized to compute the power spectrum except in this case only the signal from one microphone is used.

The coherence between all four Knowles microphones and the B&K microphone during one calibration run is shown in Figure 17 over the frequency range 100 Hz – 1500 Hz, which encompasses all frequencies of interest in the present study; i.e. the sub-harmonic (500 Hz) and fundamental (1000 Hz) frequencies.

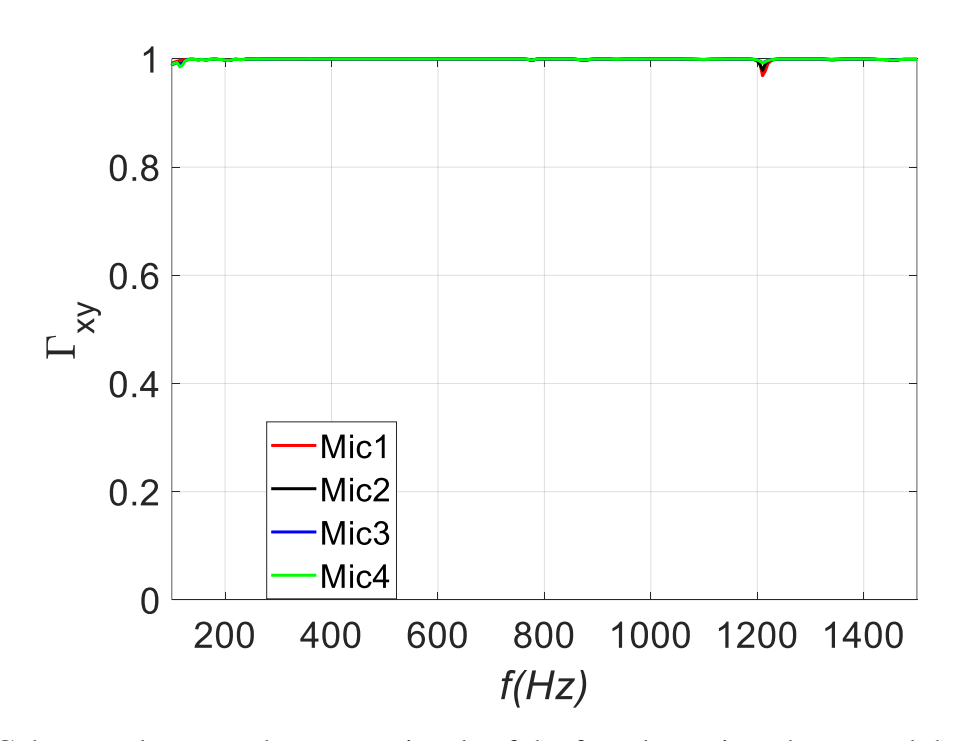


Figure 17 Coherence between the output signals of the faceplate microphones and the calibration microphone

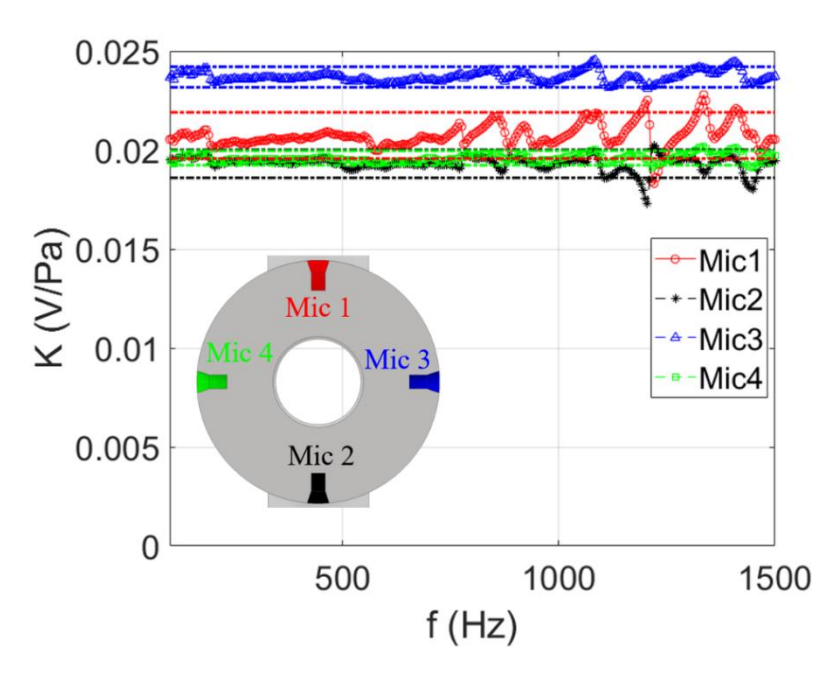


Figure 18 Sensitivity of the faceplate microphones versus the frequency range of interest. Inset shows the layout of the microphones when viewed from downstream

Some analysis is also done in CHAPTER 4 based on simultaneous acquisition of hot wire and microphone signals, which makes use of the second sub-harmonic frequency (250 Hz). As seen from Figure 17, the coherence over the range of interest is high, providing confidence in the calibration process.

Figure 18 depicts the sensitivity of the four faceplate microphones versus the frequency range of interest. The sensitivities of the microphones are obtained by averaging over the shown frequency range, yielding values of 20.73, 19.3, 23.68, and 19.59 mV/Pa for microphones 1 through 4 respectively (an inset showing the orientation of the different microphones is contained in Figure 18). For reference, the nominal sensitivity reported by the manufacturer is 22.4 mV/Pa. The uncertainty in the measured sensitivity due to fluctuation in the sensitivity versus frequency is computed from the standard deviation of these fluctuations. Figure 18 depicts the uncertainty bounds (based on confidence interval 95%) for each microphone's sensitivity using broken lines

with the same color as that of the microphone's sensitivity plot. The uncertainties are 1.16, 0.70, 0.52, and 0.36 mV/Pa for microphone 1 through 4, respectively.

Figure 19 shows the phase response of all microphones. The time delay of the different microphones can be calculated by finding the slope of a straight line fit between the phase response in rad and the frequency in rad/s. The time delay for the microphones is 1.16, 17.9, 16.29, and 21.29 μ s for microphones 1 through 4 respectively. The largest time delay is more than two order of magnitude smaller than the convection time scale of the jet, which is = 2.5 ms.

In the MatLab program used to generate the forcing signal, when the signal is synthesized using the desired values for a_f , a_{fsu} and ϕ , the actual acoustic signal measured at the jet exit does not maintain the same value of these parameters. This is due to the dynamic response characteristics of the speaker and sound propagation and interference effects within the jet facility's space. Thus, the values a_f , a_{fsu} and ϕ in the MatLab program are set based on an amplitude and a phase calibration that ensures the desired values of these parameters are achieved at the jet exit. This calibration process is described in Section 2.3.3. Figure 20 shows a comparison between the desired acoustic forcing signal and the actual forcing signal (measured with the faceplate microphone) at the forcing conditions that are investigated the most. As seen from the figure, the measured forcing signal agrees very well with the intended forcing signal. Note that for pure-harmonic forcing, the forcing signal is measured with jet flow on which produces minor modulation of the signal due to flow unsteadiness. In addition to the waveform, the overall actual SPL is checked to correspond to the target 110dB for the case shown in Figure 20. It is also notable how the output from all four faceplate microphones collapse well on one another, which is indicative of the axisymmetry of the acoustic sound field.

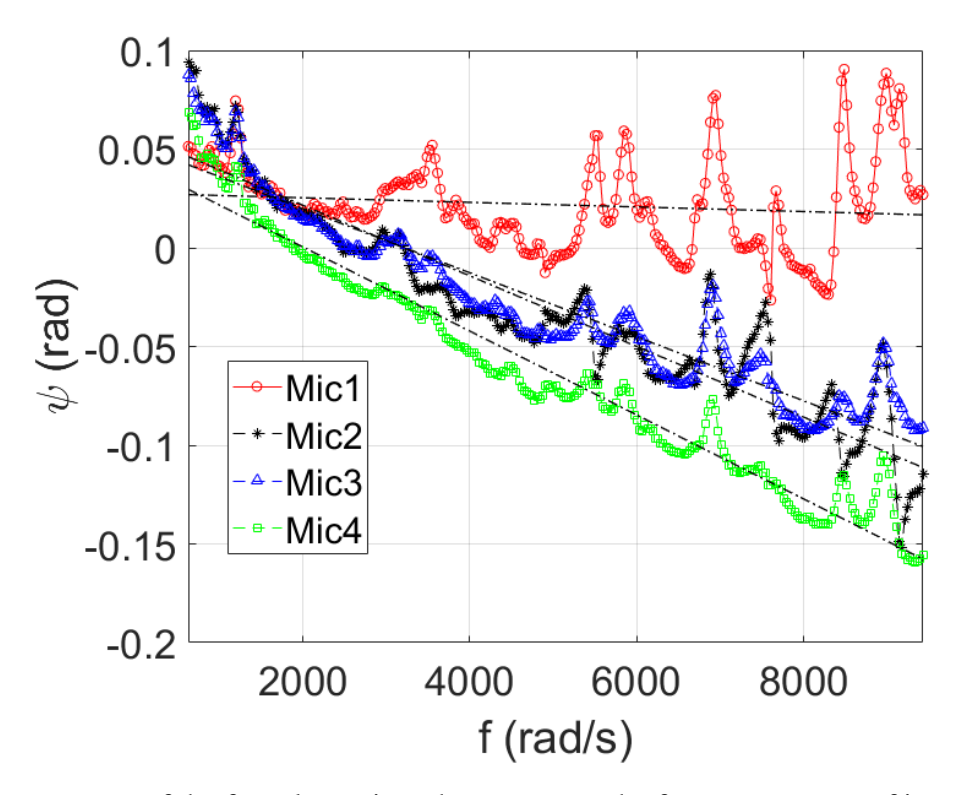


Figure 19 Phase response of the faceplate microphones versus the frequency range of interest. See inset in Figure 18 for the layout of the microphones

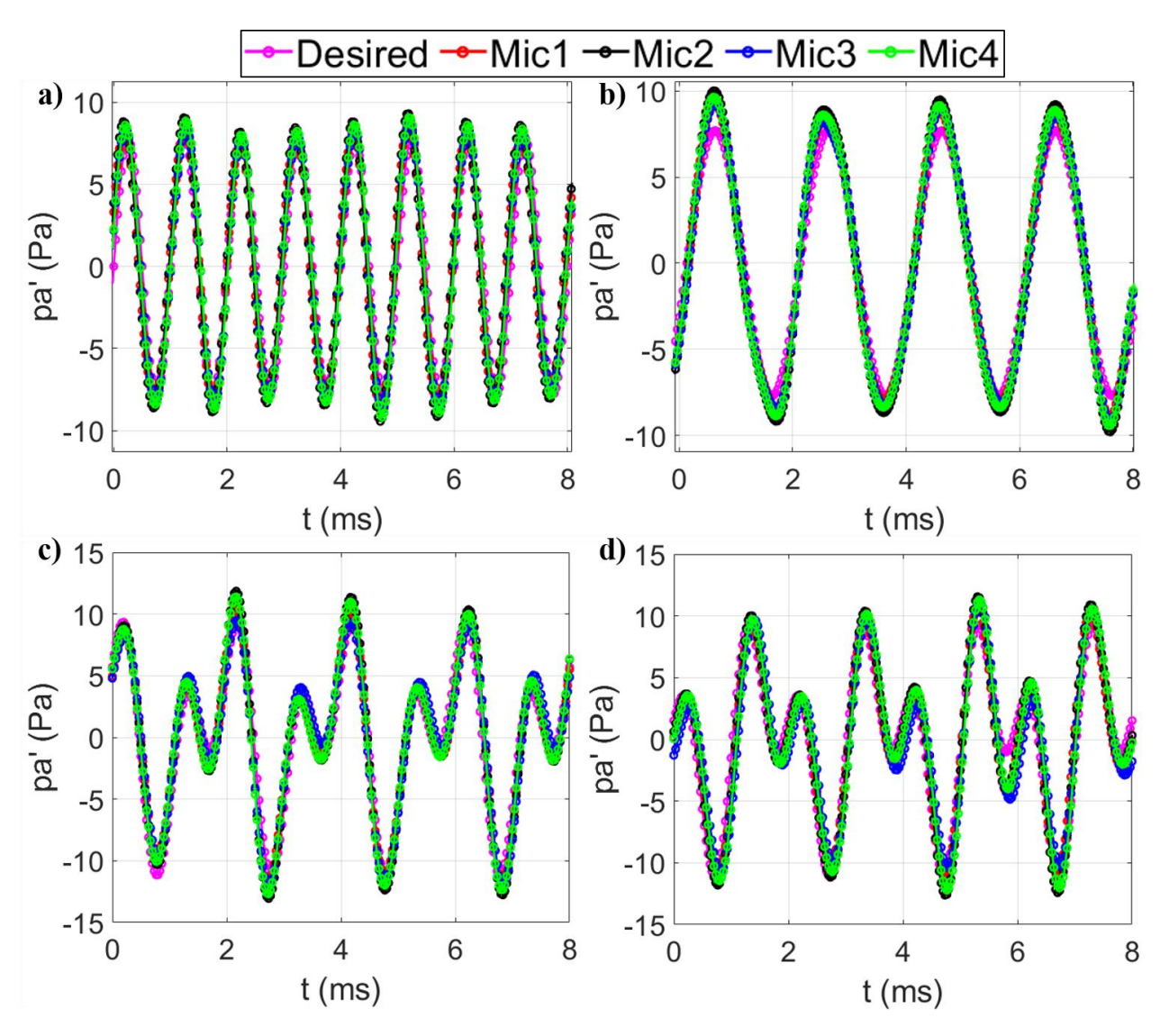


Figure 20 Comparison between the desired acoustic forcing signal and the measured forcing signal from the four microphones mounted in the faceplate, a) pure fundamental forcing, b) pure subharmonic forcing, c) bi-modal forcing at $\phi = 105^{\circ}$, and d) bi-modal forcing at $\phi = 165^{\circ}$

2.3 Experimental Procedures, Parameters and Data Analysis

2.3.1 Velocity profiles

To acquire profiles of the mean and fluctuating streamwise velocity, a single hot-wire probe is mounted on a 3-axis stepper-motor-controlled traversing system. For these profiles, the wire is oriented such that its length is along the azimuthal direction of the jet; i.e. the wire spatial resolution in the y direction is equal to the wire diameter $(5\mu m)$. The y-direction movement

resolution of the traverse (Velmex A2515C-52.5) and stepper motor (TMG 5618S-0105) combination is 0.8 μm/step. The *y*-direction motion is monitored with a LVDT (Omega LDI-119-100-A010A) to record the location of the hot wire due to the lack of feedback circuit on the *y*-axis stepper motor. The x-direction motion is monitored using a dial gauge with 0.0005" accuracy and 0.001" resolution. The streamwise direction movement resolution of the traverse (Velmex BiSlid) and stepper motor (TMG 5618S-0105) combination is 2.5 μm/step. The stepper motor is controlled by a motor-drive circuit, which is connected to a PC computer with a serial bus cable.

Before the experiment, the wire is brought very close to the faceplate (within approximately 0.5 mm), then a top view image is captured using a Sony CCD camera (N50) with a scale grid in the field of view. Using the scale and the number of pixels between the hot wire and the faceplate, the distance between the faceplate and the hot wire is determined. Subsequently, the dial gauge mentioned above is set to monitor the x-direction motion. Another Sony CCD camera (N50) is used to capture an image in the side plane with a scaling grid in the field of view. Using the scale and the number of pixels on both sides of the hot wire with respect to the jet exit, the hot wire is centered in the z-direction.

To capture data across the entire width of the jet, the hot wire is initially moved from y = 0 to y = 7.5 mm then the measurement commences in the negative y-direction. The number of steps in the traverse for a given profile varies between 80 and 120 steps according to the x/D location, separated by 0.125 mm/step (0.01D) for the shear-layer zone and 0.25mm/step (0.02D) for the jet core zone. This yields a profile spanning a y-direction domain between 12.7 and 16 mm (1D and 1.26D). The profile width is large enough to capture the jet shear layer fully at least on one side of the jet core. Table 2 lists the different experiments implemented with the current setup. The first two column from the left depicts the flow conditions, and the column on the right depicts

the forcing condition. At each wire location, The ADC board discussed in Section 2.2.3 is used to acquire the hot-wire signal using MatLab. The acquisition frequency is 10 kS/s ($f_sD/U_j=25.4$), and the time series is 30 seconds long ($TU_j/D=11,811$). The acquisition frequency is 10 times the fundamental frequency (1000 Hz; $St_D=2.54$). For computation of spectra, like those shown in Figure 13 and Figure 14, the time series is partitioned into 1500 records, each containing 200 points. The spectrum for each record is computed by taking the Fast Fourier transform (FFT) of the record and multiplying the result with its complex conjugate. The spectra from all records are then averaged to obtain the spectral estimate. The resulting spectrum uncertainty is 5% of Δf (based on confidence interval 95%) and the frequency resolution is $\Delta f=50$ Hz ($\Delta St=0.127$).

Table 2 Summary of the hot-wire experiments

Flow conditions		Forcing conditions		
U_j =5 m/s Re_D =4,223	H/D=2	 Natural jet Pure harmonic forcing Bi-modal forcing 		
		$f = 1000 Hz (St_D = 2.54)$ $f_{SU} = 500 Hz (St_D = 1.27)$		
		$\phi = 105^{\circ} \& 165^{\circ}$		
		Forcing amplitude $(\%U_j)=0.3\%$		
		$AR = \frac{a_f}{a_{f_{SU}}} = 1$		

2.3.2 Flow visualization

To start the flow visualization procedure, the acoustic forcing system is calibrated as described in Section 2.3.3 below, to enable setting the amplitude ratio of the fundamental and subharmonic modes and the intermodal phase ϕ to the desired values. The CMOS camera is

focused on a target in the visualization plane and the laser light is turned on. The laser power is set to low level to align the laser sheet with the focus target. Subsequently, the laser is set to full power, the jet flow is set to the desired velocity by setting the stagnation pressure to a predetermined value, and the seeding is activated by turning on the atomizer as discussed in Section 2.2.2. Image capturing is initiated using a PC program (Phantom Camera Control), while a MatLab code runs simultaneously to record the stagnation pressure, the four faceplate microphones, the jet inlet flow temperature and the ambient temperature. The stagnation pressure is used to check the consistency of the jet velocity during the experiment, while the faceplate microphones are used to check the acoustic forcing signal during the experiment.

A total of 20,000 images are captured over a time period of two seconds ($TU_j/D = 787$) and saved as mp4 files. Table 3 lists a summary of the parameters used in the impinging jet experiments.

Table 3 Summary of the flow visualization experiments

Flow conditions				Forcing conditions							
			f = 1000Hz		$f_{su} = 500Hz$		Bi-modal f and f_{su} $\phi = 0^{\circ} - 165^{\circ}$ at $\Delta \phi = 15^{\circ}$				
				Forcing amplitude $(\%U_j)$							
$U_{j} = 5 \text{ m/s} $ $Re_{D} = 4,223 $ H $/D$		2	Natural jet	0.1	0.3	0.1	0.3	0.3		0.1	
								AR A			AR
								0.5	1	2	1
							0.3				
	/D	/D 3		0.3		0.3		AR			
								1			
				0.3		0.3		0.3			
		4						AR			
								1			

2.3.3 Acoustic Forcing

An important aspect in the acoustic forcing experiments is to ensure that the forcing parameters a_f , a_{fsu} (the modal amplitudes) and ϕ (the intermodal phase) as measured by the faceplate microphones at the jet exit match their target values. To this end, a procedure is implemented to "calibrate" the amplitudes and phase required in creating the forcing signal. This calibration is implemented by using one of the faceplate microphones while the jet flow is turned on. For the calibration process an acoustic signal with $\phi = 0^{\circ}$ at a given $AR = \frac{a_f}{a_{fsu}}$ is created in a MatLab program. The resulting acoustic signal is acquired with one of the faceplate microphones (microphone #1 in this case) and analyzed to determine the a_f , a_{fsu} and ϕ of the actual sound signal at the jet exit. If the a_f and a_{fsu} of the measured sound are different from required value,

then an adjustment of the amplitude values in the MatLab code is made, and the process is reiterated until the required sound level and amplitude ratio (AR) is reached. An example of the spectrum of the acoustic forcing signal after matching the modal amplitudes is shown in Figure 21.

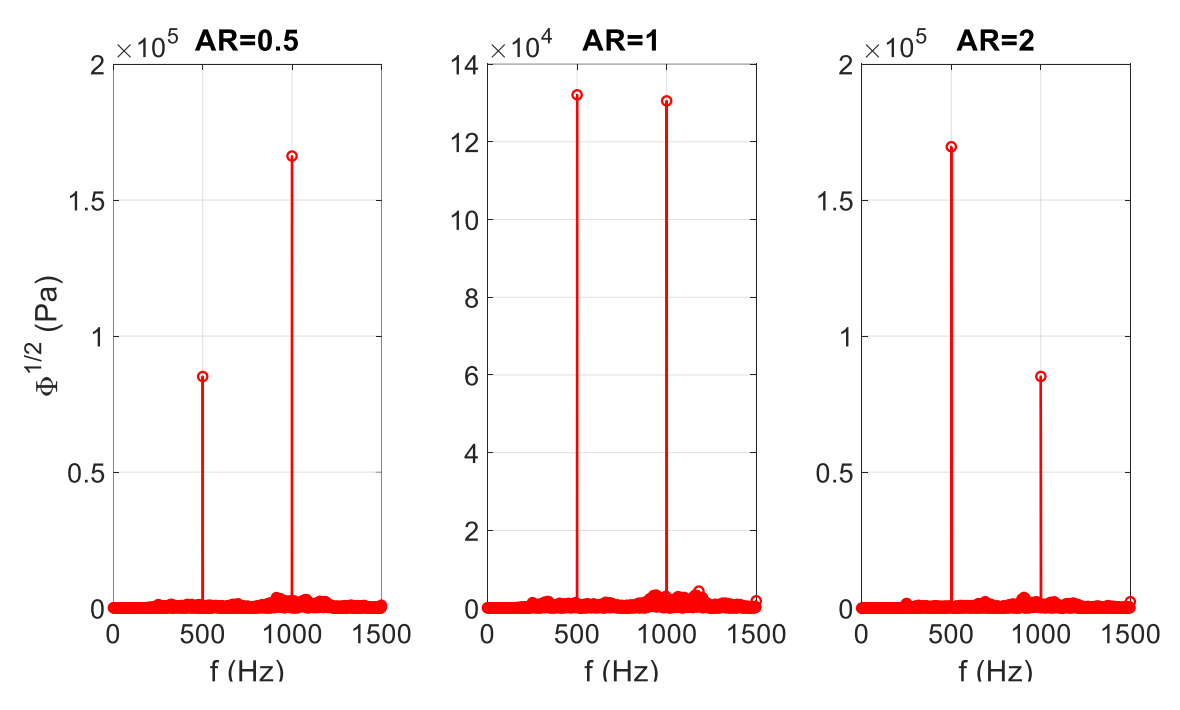


Figure 21 Forcing signal FFT amplitude for faceplate microphone #1 using different amplitude ratios: AR=0.5 (left), 1 (middle), and 2 (right)

For the intermodal phase, the measured phase shift between the modes is used as a phase angle offset in the MatLab code. This ensures that the acoustic intermodal phase is the same as desired at the jet exit. This can be verified from the comparison between the actual and the target acoustic signals shown earlier in Figure 20 (parts c and d).

CHAPTER 3. FLOW VISUALIZATION

Flow visualization images are analyzed in this chapter using qualitative and quantitative approaches. The qualitative method includes analyses of both time-averaged and time-resolved images to investigate the effect of forcing on the vortical structures of the jet and their subsequent interaction with the wall. On the other hand, the quantitative methods include measuring the particle-free core width, finding the minimum core width, and estimating the percentage of the time certain organized structures are present. The effect of different forcing parameters on the outcome of the analyses is studied and presented as follows: Section 3.1 discusses the effect of the intermodal phase shift (ϕ) on the flow structure. Section 3.2 discusses the effect of the forcing amplitude level, and Section 3.3 examines the amplitude ratio (AR) influence. The focus of the analysis is on H/D=2 with some consideration for H/D=3 and 4 in Section 3.4 to study the effect of the impingement plate location.

3.1 Intermodal Phase (ϕ) Effect

3.1.1 <u>Time-averaged analysis</u>

Time-averaged images are obtained by taking the average of all images for a given case and normalizing it by the maximum intensity in the image. Figure 22 shows an example of an averaged flow visualization image, where it is clear that the seeding particles predominantly reside in the shear layer (jet perimeter), leaving the jet core free of particles. The minimum width of this particle-free core, denoted by $C_{w,min}$ is indicated in Figure 22. Since particles are injected into the vortical fluid (the boundary layer upstream of the jet exit), a narrower particle-free core is assumed to correspond to a larger spread of the shear layer, at least in the qualitative sense. That is, the particle-free core is not expected to correspond exactly to the width of the potential core, but a

smaller $C_{w,min}$ is expected to correspond to a narrower potential core. This point is used in the following to compare the shear layer spread under different forcing conditions.

The average images are displayed in Figure 23 using a color map for all cases at H/D=2and both pure harmonic as well as bi-modal forcing (AR = 1 and forcing level of 0.3%). Visually, the images show a significant effect from the forcing on the width of the core of the jet that is free of particles. For example, bi-modal forcing with $\phi = 165^{\circ}$ shows a significant reduction in $C_{w,min}$ in comparison to the unforced jet. To examine the $C_{w,min}$ variation between the different cases more systematically, the particle-free core width is found in the average image by measuring the smallest particle-free width over the streamwise extent of the image. The measurement is implemented from the centerline to the first pixel with an intensity higher than the particles-free core intensity in the top and the bottom shear layer. The two values are then added to determine the full width. The threshold above which the intensity is considered to be higher than the core is 20 % of the maximum pixel intensity. The process is demonstrated in Figure 24, which shows the cross-stream (y/D) normalized pixel intensity profiles at different x/D locations for the natural case. As demonstrated in the figure, the profiles near the core are smooth and do not exhibit random fluctuation. Therefore, the uncertainty of measuring the particle-free core width is estimated to be the same as the image pixel resolution, or \pm 0.127mm (0.01D). It is also noted that the actual value of C_w will depend on the threshold chosen. However, the true value of C_w is not important. The main objective is to apply the selected threshold consistently to be able to compare the trend in C_w for the different cases.

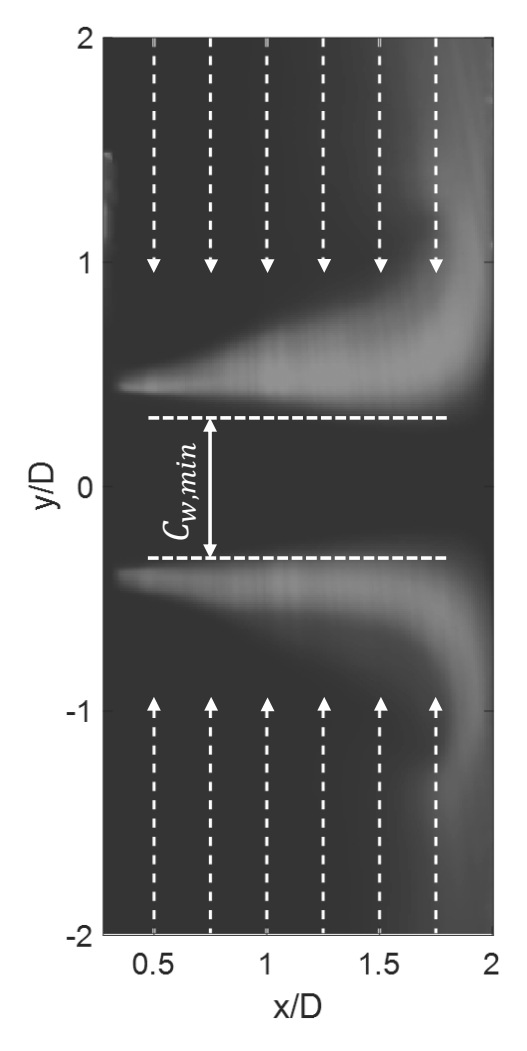


Figure 22 An average image of the natural case demonstrating the minimum particle-free core width. Arrows mark streamwise locations at which intensity profiles are extracted for analysis in Figure 24

Examination of Figure 24 shows that the particle-free core width generally decreases and the thickness of the seeded region increases with distance downstream of the jet exit. The thinnest shear-layer thickness (seeded region width) is found close to the faceplate in Figure 24b and it increases in thickness in the streamwise direction. This is indicative of the shear layer development from the jet exit to the impingement wall. It is notable that the intensity profiles generally depict a single intensity peak on a given side of the jet centerline except close to the impingement plate. At x/D = 1.75 (and one one side of x/D = 1.5), a second peak is found farther away from the jet centerline. Comparison of these "double-peaked" profiles with the colormaps in Figure 23 shows

that while the inner peak corresponds to the jet shear layer, the outer peak relates to the seeding particles upwelling from the wall after impingement. As will be seen from the observations of the time-resolved visualization, this upwelling is the result of the well-known vortex-wall interaction and subsequently boundary layer separation and vortex ejection away from the wall.

The detailed streamwise evolution of the particle-free core is determined from the normalized intensity profiles as those shown in Figure 24 at every single column in the image (i.e. at every pixel in the streamwise direction). Subsequently, a 5-point average (equivalent to 0.05D of streamwise increment) is used to smooth the function C_w in the streamwise direction (x/D) to remove any scatter without affecting the outcome. Examples of such profiles may be seen in Figure 26 for selected cases. These profiles show that the particle-free core decreases with downstream distance up to the vicinity of x/D = 1.6 before widening close to the impingement plate.

Figure 25 shows the minimum width of the particle-free core for all cases, which is generally found close to the impingement plate. The natural jet is found to have the widest $C_{w,min}$. Harmonic and bi-modal forcing cause a reduction in $C_{w,min}$ relative to the natural jet with interesting effects seen for the intermodal phase of bi-modal forcing. Specifically, a non-monotonic phase effect is found with the widest particle-free core found at $\phi = 90^{\circ}$ and 105° , and the narrowest at $\phi = 165^{\circ}$. The difference between the maximum and minimum core widths for bi-modal forcing can be seen clearly in the enlarged average images in Figure 26.

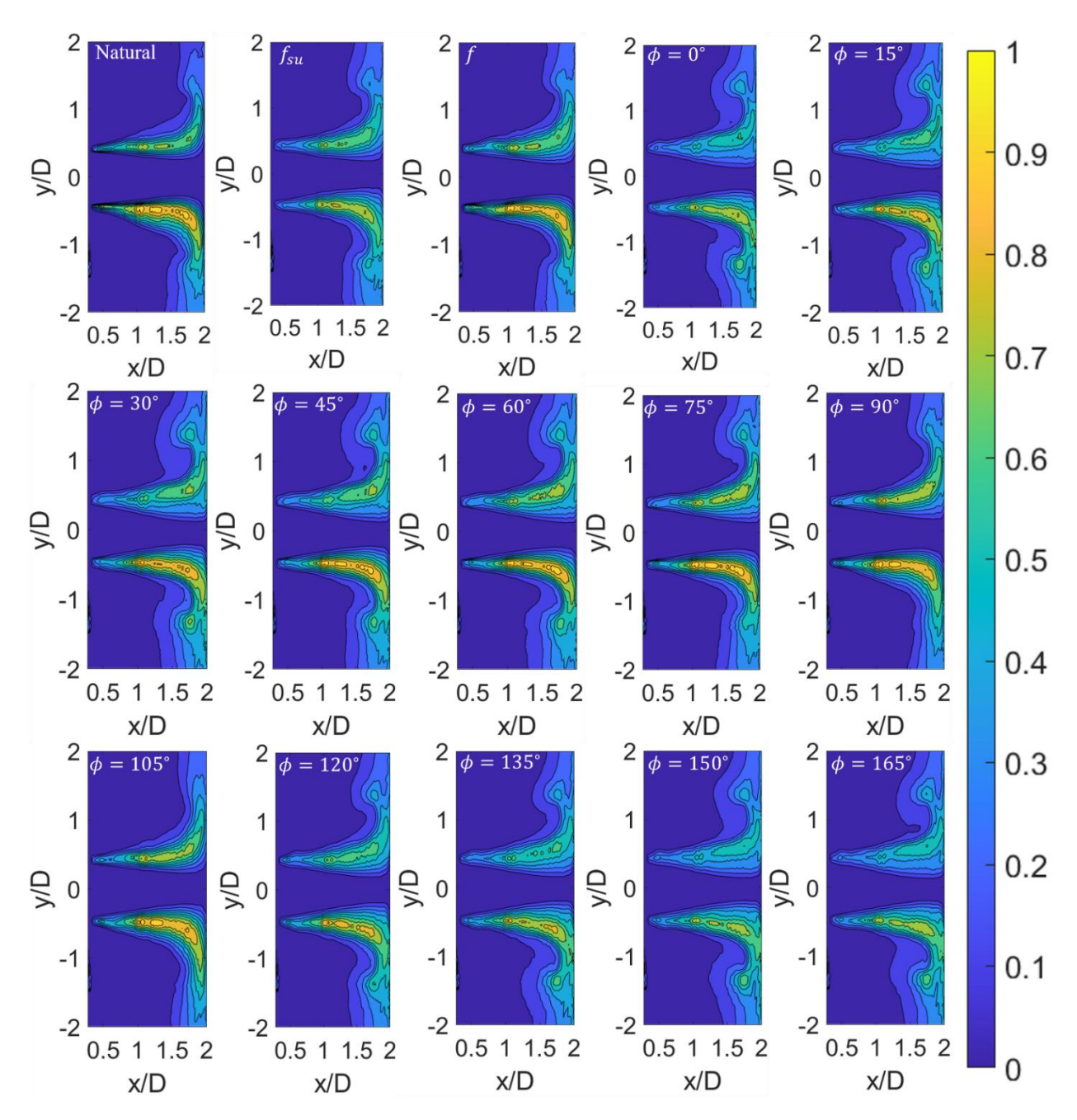


Figure 23 Time-averaged images for the natural and all forcing cases at H/D=2, AR = 1 and 0.3% forcing level. The flow is from left to right, and the leftmost edge of the image corresponds to x/D=0.47, while the right edge corresponds to the impingement wall (f_{su} refers to pure subharmonic forcing, and f to pure fundamental forcing). Color scale indicates normalized pixel intensity

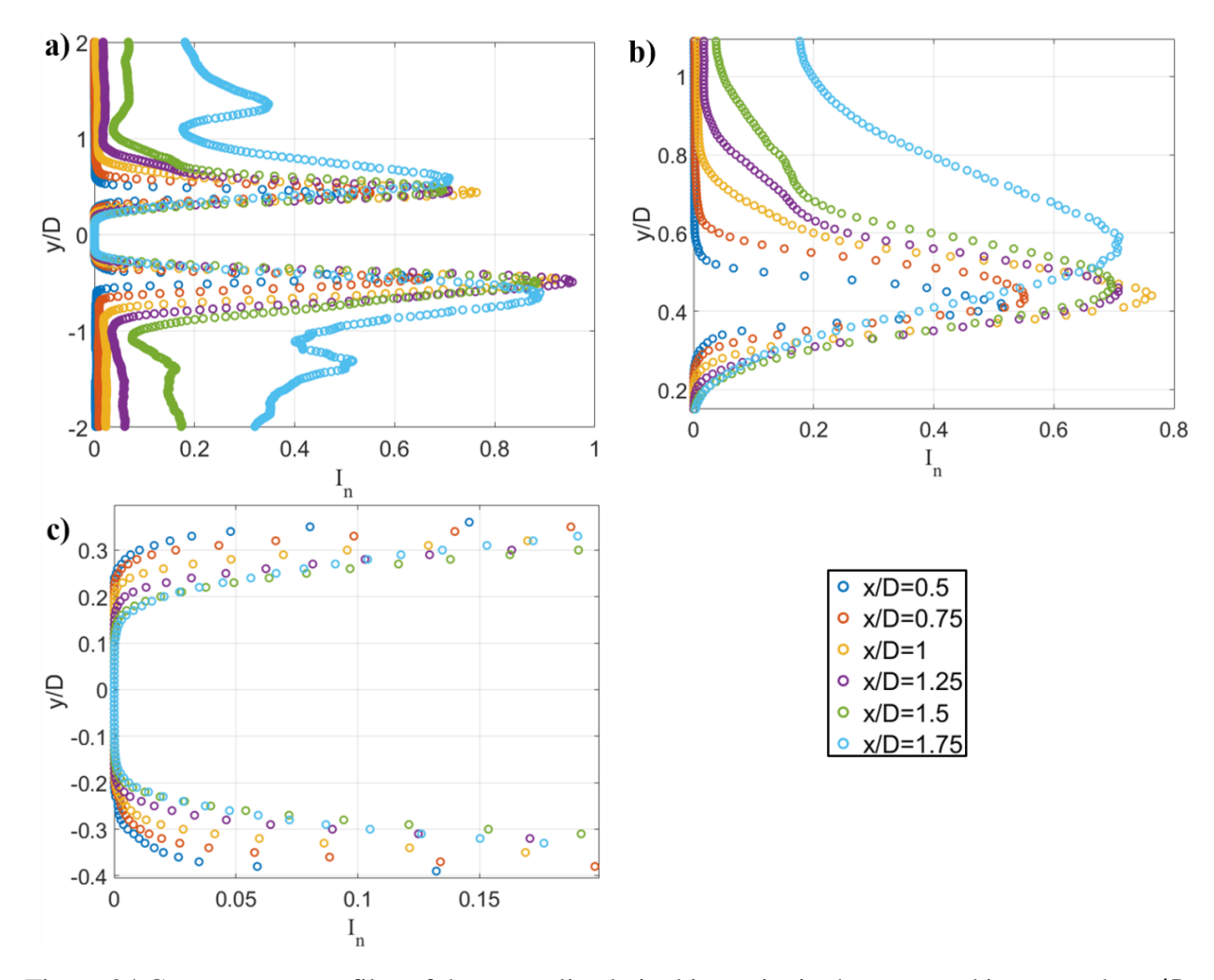


Figure 24 Cross-stream profiles of the normalized pixel intensity in the averaged image at the x/D locations indicated with arrows in Figure 22. The case shown is for the natural jet; a) complete profile, b) zoomed view for the upper shear layer, and c) zoomed view of the jet centerline

Figure 25 also shows that pure-harmonic forcing cannot reduce the potential core width to the extent that bi-modal forcing can do. The largest reduction of C_w through pure-harmonic forcing, which is accomplished with forcing at the fundamental frequency, is comparable with the smallest reduction using bi-modal forcing. This shows that bi-modal forcing is more effective in changing the jet behavior than pure harmonic forcing.

Figure 27a depicts the streamwise evolution of the particle-free core width normalized by the jet diameter for the natural case compared to the cases involving pure harmonic forcing and the bi-modal forcing cases resulting in the widest ($\phi=105^\circ$) and narrowest ($\phi=165^\circ$) $C_{w,min}$. Inspection of the figure shows that the minimum core width is smaller for the forced cases in comparison to the natural jet. This indicates a larger spread of the shear layer in the presence of forcing, as would be expected. For the harmonic forced cases, it appears that forcing at the fundamental frequency leads to slightly narrower core than forcing at the subharmonic. However, as will be seen from the time-resolved visualization analysis in Section 3.1.2, forcing at the subharmonic frequency accelerates/enhances vortex pairing, and hence leads to faster spread of the shear layer. This is not inconsistent with the results in Figure 27a since the subharmonic forcing case shows the steepest slope of C_w in the streamwise direction; i.e. the fastest development of the shear layer between the two harmonic cases. This can be seen more clearly in Figure 27b, where C_w is normalized by its most upstream value (C_{wu}) within the observation domain. The results show that forcing at the subharmonic not only leads to the fastest shear layer development in comparison to the natural and the fundamental case, but also to the largest shear layer growth between the most upstream and most downstream observation locations. Bi-modal forcing at $\phi =$ 105° shows similar behavior to forcing at the fundamental forcing, while bi-modal forcing at $\phi =$ 165° shows the smallest particle-free core width and the fastest shear development of all cases. It presents the narrowest particle-free core from the beginning to the end of the domain.

Another interesting observation in Figure 23 relates to the behavior of the boundary layer subsequent to the impingement of the jet on the wall. In all cases, upwelling in the boundary layer is seen in the range 1 < r/D < 2. This upwelling, which is connected to the unsteady separation of the boundary layer (as will be seen later), is least pronounced for the natural jet and the bi-modal jet forced at $\phi = 105^{\circ}$ (cases with the widest $C_{w,min}$). In comparison, the upwelling is most

pronounced for cases with a narrow particle-free core, including the case having the narrowest $C_{w,min}$: $\phi = 165^{\circ}$. This is most evident in Figure 26.

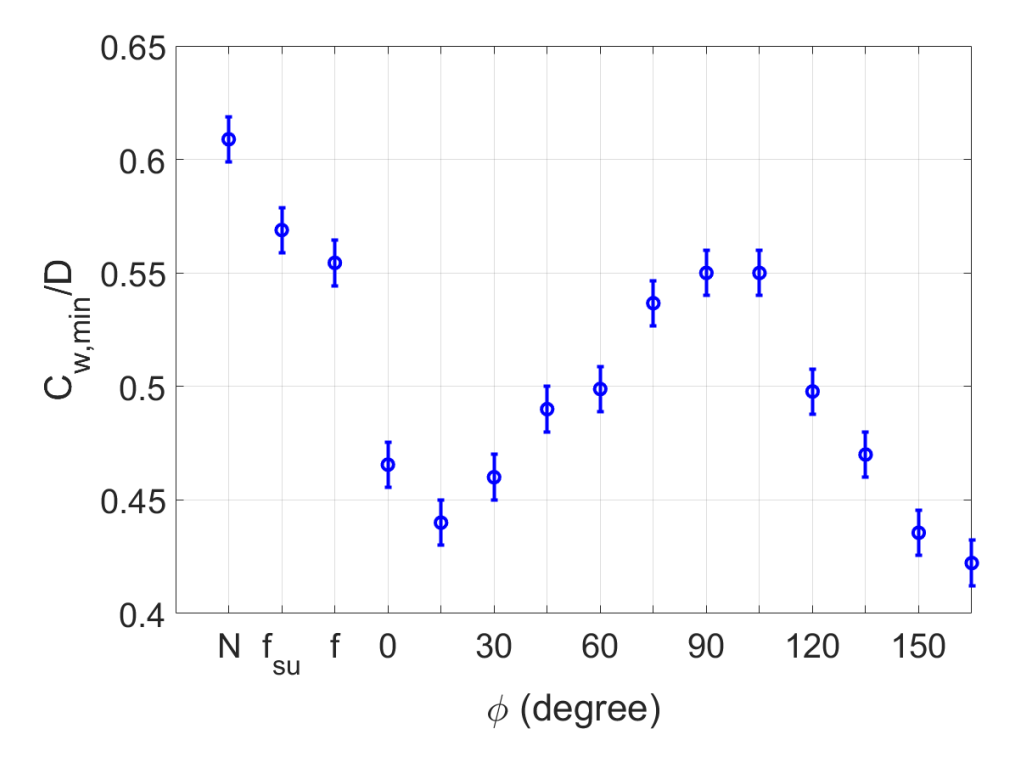


Figure 25 Minimum particle-free core width for the natural jet and all forcing cases at H/D=2, AR=1 and 0.3% forcing level (N refers to the natural case, f_{su} to pure subharmonic forcing and f to pure fundamental forcing)

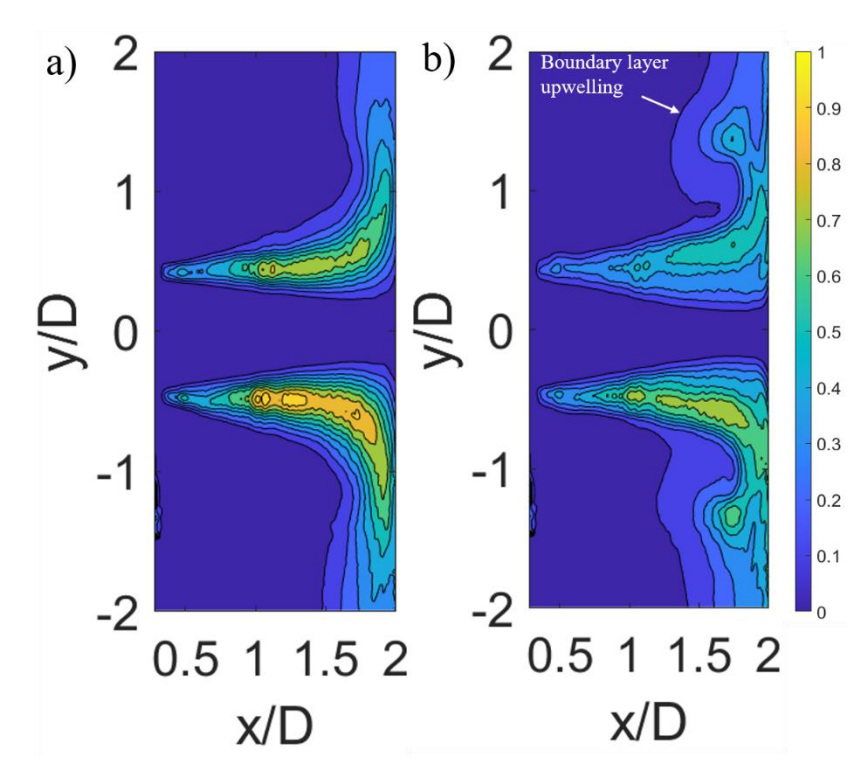


Figure 26 Time-averaged images depicted as color maps of the normalized intensity at a) $\phi = 105^\circ$ and b) $\phi = 165^\circ$, H/D = 2, AR = 1 and 0.3% forcing level

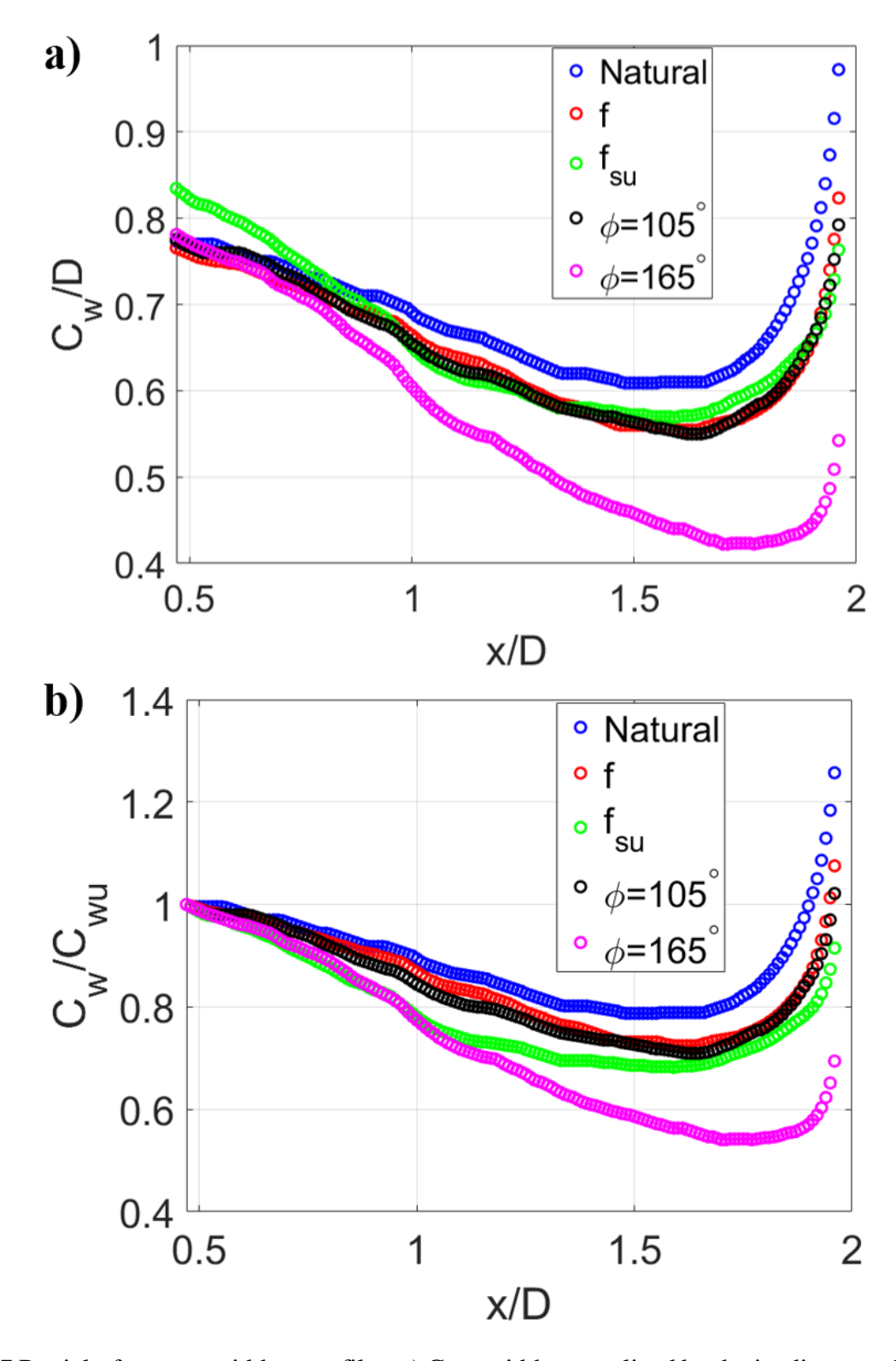


Figure 27 Particle-free core width x-profiles. a) Core width normalized by the jet diameter. b) Core width normalized by the core width at x/D = 0.47

3.1.2 Time-resolved analysis

To gain a deeper understanding of the jet vortical structure behavior associated with the observations seen in the time-averaged images, an analysis of the instantaneous flow in the timeresolved visualization images is made here. Figure 28 and Figure 29 depict two types of vortex evolutions that are predominantly seen in the natural jet. Broadly speaking, the figures show that despite the absence of forcing, the natural jet shows symmetry in the vortex evolution between the top and the bottom shear layer. This is taken to reflect the natural flow axisymmetry (although confirmation of full axisymmetry would require observations along the full perimeter of the jet). In both Figure 28 and Figure 29, vortices emerge into the left side of the images at the fundamental frequency (1000 Hz, $St_D = 2.54$) while they are rolling up and growing in size. Subsequently, two (Figure 28) or three (Figure 29) of these vortices merge before reaching the impingement wall. In the former scenario, the vortex passage frequency reduces to the subharmonic frequency (500 Hz, $St_D = 1.27$), and in the latter to one-third of the fundamental frequency (≈ 333 Hz, $St_D = 0.845$), while the vortex structure becomes bigger. Aside from these two vortex evolution scenarios in the unforced jet, on rare occasions double pairing of vortices (two subsequent merging events of two vortices) occurs, leading to the lowest vortex passage frequency (250 Hz, $St_D = 0.635$) and the largest vortex structure prior to, or at the beginning of, the interaction of the merged vortex with the wall. The vortex evolution details in Figure 28 (single pairing event) and Figure 29 (single merging event of three vortices) are described next.

Figure 28 depicts the vortical evolution of a single vortex merge between the jet exit and the impingement plate. The red and green arrows in image 1 point at two vortices at the upstream end of the visualized flow field. To start the pairing, the trailing vortex (pointed to with the red arrow in image 2) slightly shifts towards the jet centerline, hence the vortex gets pulled into the

vicinity of the leading vortex (pointed to with the green arrow in image 2), and then the two vortices start rolling around each other and complete the pairing process, forming one vortex (image 3). After the pairing is completed, the paired vortex keeps convecting downstream (images 4 and 5) up to the impingement plate. When the vortex gets very close to the plate (image 7), the vortex shifts away from the jet centerline, and the vortex convection starts to change from the streamwise to the radial direction, along the impingement plate (image 8).

The most prominent scenario with the natural jet is the occurrence of the first pairing only, as demonstrated in Figure 28. However, the other scenario that is also observed is that of threevortex merging (Figure 29). In Figure 29, the leading vortex pointed to with a yellow arrow in image 1 convects downstream while the other two vortices (indicated with red and blue arrows) interact together. The leading vortex has the largest size, which pulls the other two vortices into its vicinity. The second vortex (blue arrow) and the third vortex (red arrow) shift slightly toward the jet centerline to start the merging process (image 2). The second and the third vortex start merging together first before rolling around the first vortex (image 3) and shifting toward the jet centerline (image 4). The purple arrow points at the resulting vortex from the three-vortex merging (red, blue, and yellow). The merged vortex travels downstream until it gets closer to the impingement plate (image 6). Finally, the vortex starts to change the direction of convection from the streamwise to the radial direction and hence convects parallel to the impingement plate. The three-vortex merging scenario excludes the opportunity for another pairing to occur before impingement; i.e. without external control of the jet, H/D=2 leaves a streamwise fetch that allows the jet vortices to exhibit three-vortex merging at best, with single pairing being the more common event. Since vortex merging leads to the growth of the shear layer, the number of vortex merging events occurring ahead of impingement is connected to the rate of shear layer growth.

Also, the switching between the different vortex merging modes (including the rare double-pairing, and also the occasional passage of the initial vortices without any pairing) reflects an inconsistency (disorganization) of the natural jet behavior.

With the application of acoustic forcing, the rare case of double merging (250 Hz, St_D = 0.635 vortex passage frequency) in the natural jet is enhanced, leading to larger vortex structures before impingement, a narrower particle-free core, and faster shear layer growth. The doublepairing vortex evolution is demonstrated in Figure 30 for the case of pure harmonic forcing at the fundamental frequency (1000 Hz, $St_D = 2.54$). The white and orange arrows in Figure 30 (image 1) point at the first two vortices emerging from the jet faceplate into the flow field, these two vortices roll around each other close to the faceplate. Then the trailing vortex (pointed with the white arrow) shifts slightly to the centerline to initiate pairing (image 2). The paired vortices result in a bigger vortex (pointed with the blue arrow in image 3). Image 4 shows the newly paired vortex (pointed with the blue arrow) and another emerging vortex from the faceplate (pointed with the green arrow). The vortex pointed with the green arrow convects downstream while another vortex emerges from the jet faceplate (pointed with the red arrow in image 4). The red and the green arrows in (image 4) show the second two vortices convecting downstream while undergoing the initial roll. Image 5 shows the second two vortices after convecting downstream while they interact together. The vortex interaction between the two vortices initiates pairing. The two vortices start to roll together and convect downstream, completing the pairing process. This results in a bigger vortex (pointed with the yellow arrow in image 6). The newly paired vortex (pointed to by the yellow arrow in image 6 and 7) start interacting with the leading vortex (pointed with the blue arrow) right after the first pairing is completed to initiate the second pairing.

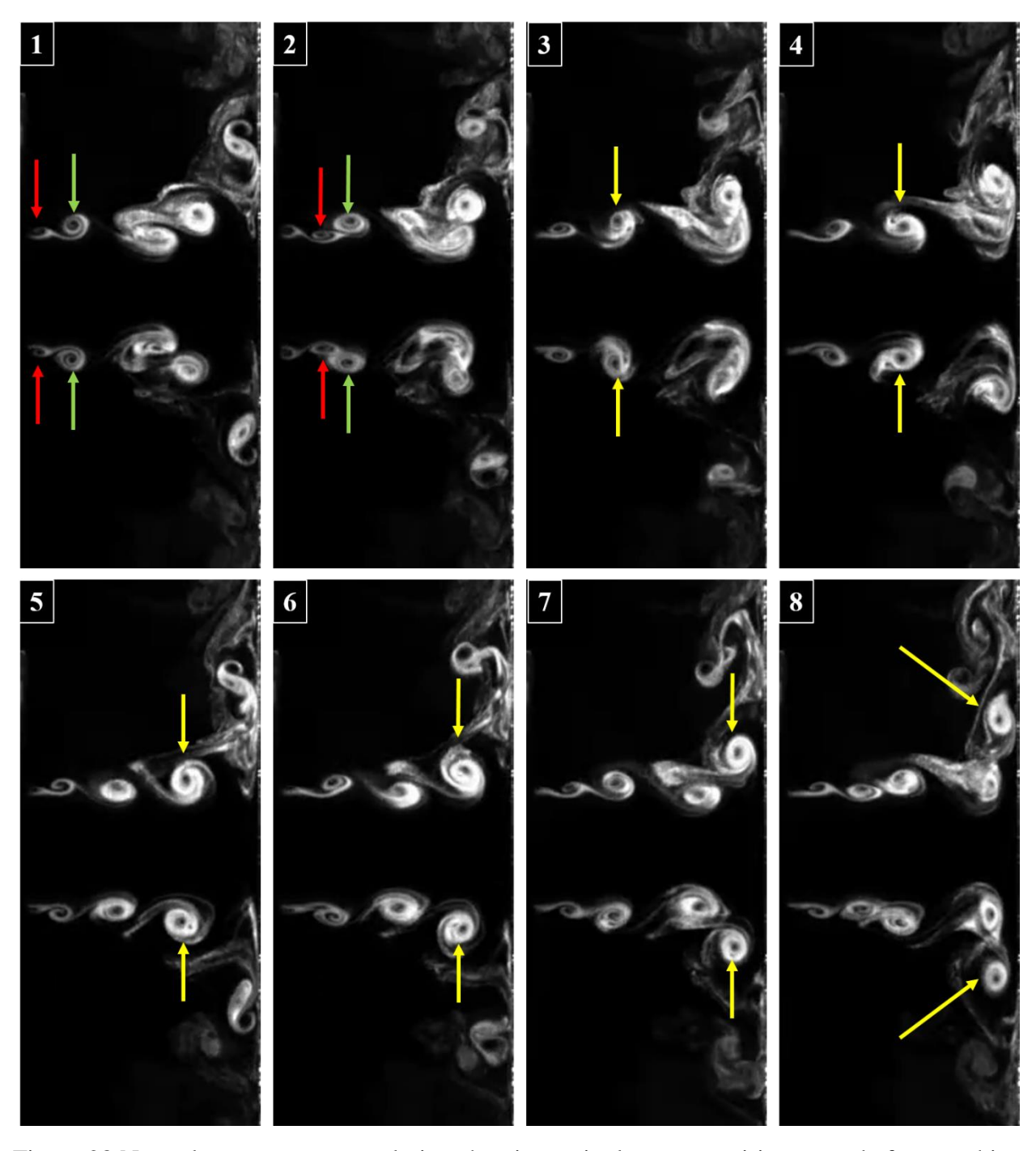


Figure 28 Natural case structure evolution showing a single vortex-pairing event before reaching the impingement plate for H/D=2. Flow is from left to right and the time between images is $0.8 \ ms$, $\Delta t U_j/D=0.31$. Arrows indicate particular vortex structures

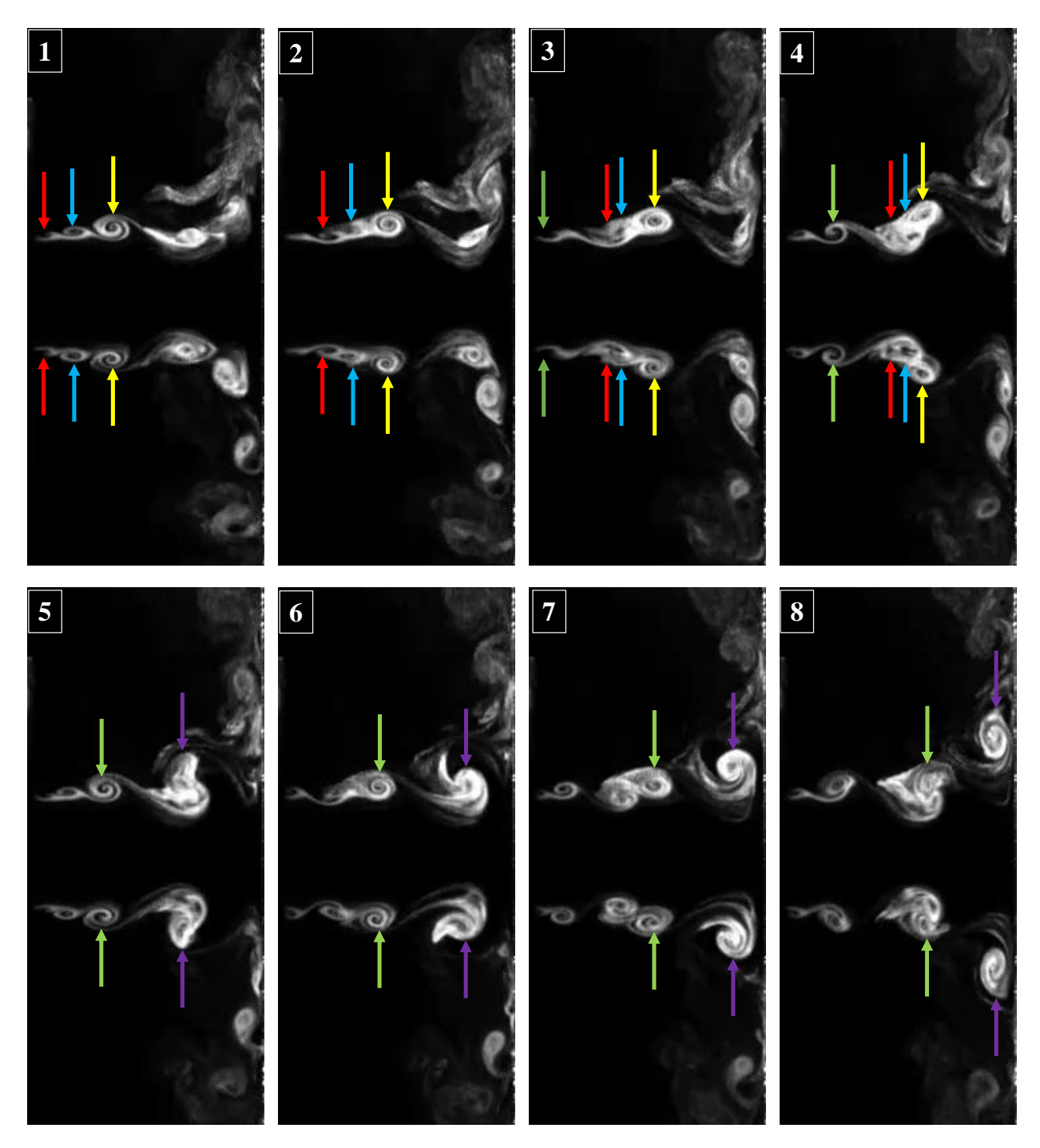


Figure 29 Natural case structure evolution showing three-vortex merging before reaching the impingement plate for H/D=2. Flow is from left to right and the time between images is $0.8 \, ms$, $\Delta t U_i/D=0.315$. Arrows indicate particular vortex structures

Likewise, the second pairing starts (image 7), between the two vortices by an initial roll around each other until the second pairing is completed (image 8) resulting in a bigger vortex (pointed with the purple arrow) near the impingement plate. Hence the newly paired vortex

convects downstream until it gets very close to the impingement wall. Afterward, the vortex starts impinging on the wall and changing its convection direction from streamwise to radial direction.

The promotion of double pairing by acoustic forcing clarifies the narrowing of the particlefree core $C_{w,min}$, seen in Figure 25, with the application of the forcing. This does not, however,
explain why the narrowing is more effective with bi-modal than pure-harmonic forcing, and why
the narrowing depends on the intermodal phase in bi-modal forcing. Inspection of the images
obtained for all cases shows that the introduction of the subharmonic frequency in forcing, either
in the pure-harmonic or bi-modal form, causes the presence of a different type of asymmetric
vortex structure, in addition to the promotion of the double-paired symmetric structure. This
asymmetry is not seen for the unforced jet, or the jet forced at the fundamental frequency only. An
example demonstrating the evolution of the asymmetric vortex structure may be seen in Figure 31.

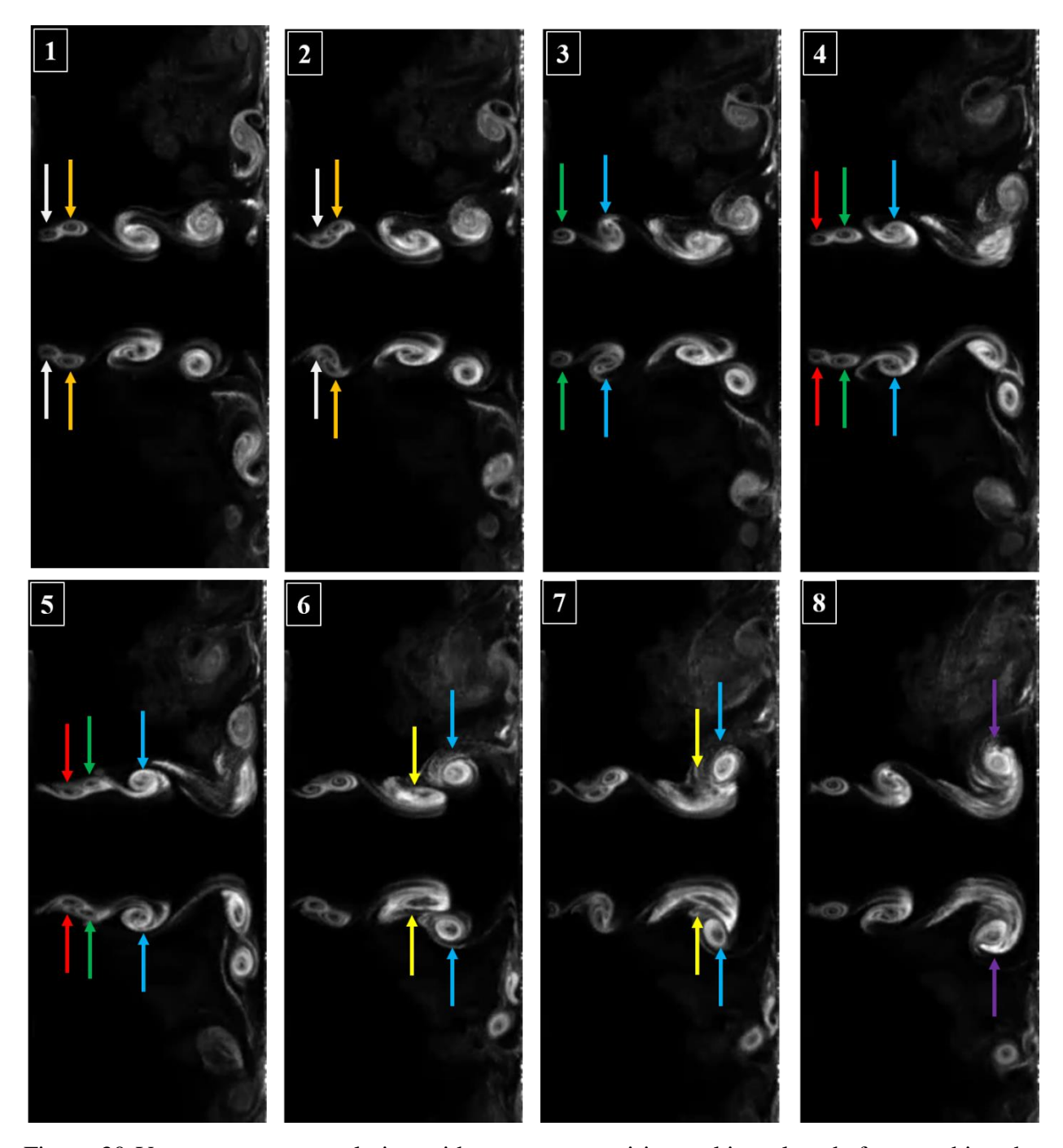


Figure 30 Vortex structure evolution with two vortex pairings taking place before reaching the impingement plate for H/D=2 and pure harmonic forcing at the fundamental frequency with a forcing level of 0.3%. Flow is from left to right and the time between images is 0.6ms, $\Delta t U_j/D=0.236$. Arrows indicate particular vortex structures

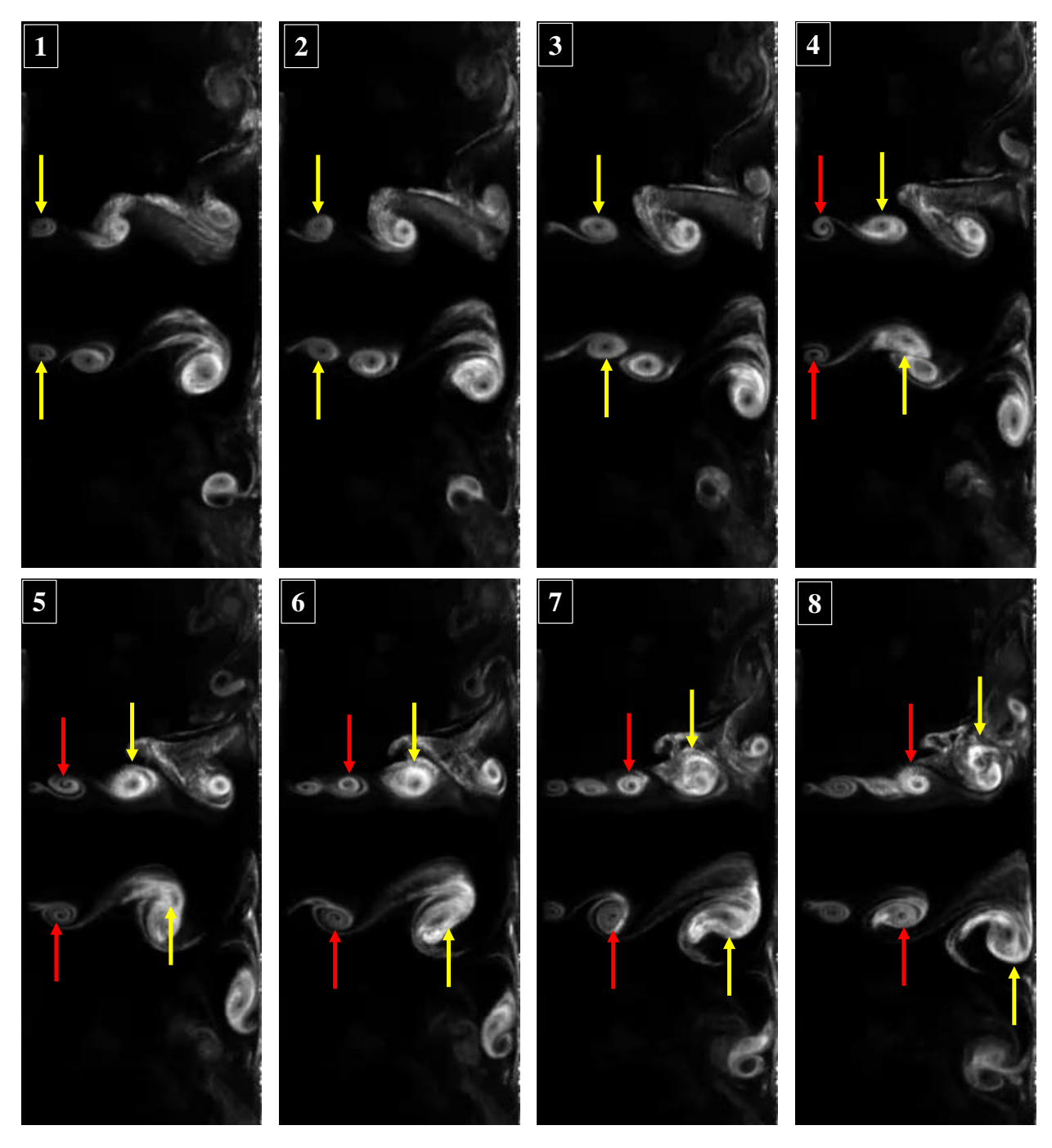


Figure 31 Asymmetric structure evolution before reaching the impingement plate for H/D=2 and bi-modal forcing $\phi=90^\circ$, AR=1, and forcing level of 0.3%. Flow is from left to right and the time between images is 0.7 ms, $\Delta t U_j/D=0.27$. Arrows indicate particular vortex structures

Figure 31 shows the different evolution of the vortical structure between the upper and the lower shear layer. The yellow arrow (image 1) points at the first vortex emerging into view, while

image 2 shows the same vortex as it convects downstream. Interestingly, the vortex core in the lower shear layer is closer to a leading vortex than the core in the upper shear layer. Hence, the lower core starts to interact with the leading vortex, which starts paring in the lower shear layer. Meanwhile, the core of the same vortex in the upper shear layer does not undergo significant vortical interaction or pairing (image 3). The two interacting cores in the lower shear layer pair and convect downstream, while the core in the upper shear layer does not undergo pairing (Figure 31 images 4, 5, and 6). Afterward, the paired vortex in the lower shear layer reaches the plate first and convects in the radial direction before the respective vortex core in the upper shear layer reaches the plate. The associated staggered arrangement of the vortex cores between the upper and lower shear layers is evident (also see the following vortex structure indicated with the red arrow in Figure 31).

The asymmetric flow structure evolution demonstrated in Figure 31 leads to the formation of a smaller structure in the upper shear layer and a larger structure in the lower shear layer. In other instances, the asymmetry can also be observed with the larger structure on top rather than on the bottom. Hence, this flip-flopping between the double-paired symmetric and the asymmetric structure would lead, on average, to a coarser particle-free core, and thinner shear layer in comparison to a jet where the double-paired symmetric structure occurs consistently. Visual observations of all cases involving subharmonic forcing suggest that the difference in the consistency of the presence (i.e. persistence) of the double-paired symmetric structure is the key to explaining the variation of the particle-free core width seen in Figure 25.

In addition to the vortex evolution upstream of the impingement plate, the interaction of the vortex structure with the impingement plate is an important phenomenon. It is well known that such interactions leads to unsteady boundary layer separation and formation of a secondary vortex of opposite sign of vorticity [45]–[49]. Figure 32 shows the vortex-wall interaction during impingement for the natural case. Image 1 shows the vortex near the impingement plate before impingement, then the vortex starts to interact with the plate (image 2), leading to a change in the vortex convection velocity from the streamwise to the radial direction (images 2 and 3). At the same time, the secondary vortex (pointed with the red arrow) starts to develop (image 3 and 4). During the development of the secondary vortex, the primary and secondary vortices (pointed with the orange arrow) start to eject from the impingement plate (images 5 and 6). This ejection, or eruption, is the reason for the "upwelling" discussed at the end of Section 3.1.1 in connection with Figure 23 and Figure 26. As conveyed from these figures, the upwelling is strongest for cases that are now understood to produce the most consistent symmetric double-paired vortex structure.

In conclusion, the natural jet shows a less organized but symmetric structure exhibiting a single pairing or merging of three vortices ahead of reaching the impingement plate. Rarely, double pairing might take place, or the initial vortices may not pair or merge at all. Forcing in the pure-harmonic or bi-modal form leads to the promotion of a double-paired symmetric vortex structure, and hence reduction in the particle-free core width, faster development of the shear layer, and stronger vortex-wall interaction. However, the introduction of the subharmonic frequency in forcing leads to a switch between the double-paired symmetric structure and an asymmetric structure. The switching (intermittency) between these two modes is suspected to be the reason for the sensitivity of the effect of forcing to the intermodal-phase in the bi-modal forcing scheme. This sensitivity is expected to be such that the intermittency is minimized with the symmetric mode being dominant when the particle-free core is narrowest ($\phi = 165^{\circ}$) and is maximized for the thickest core (subharmonic forcing and bi-modal forcing at $\phi = 90^{\circ} - 105^{\circ}$). This hypothesis is examined quantitatively in the following section.

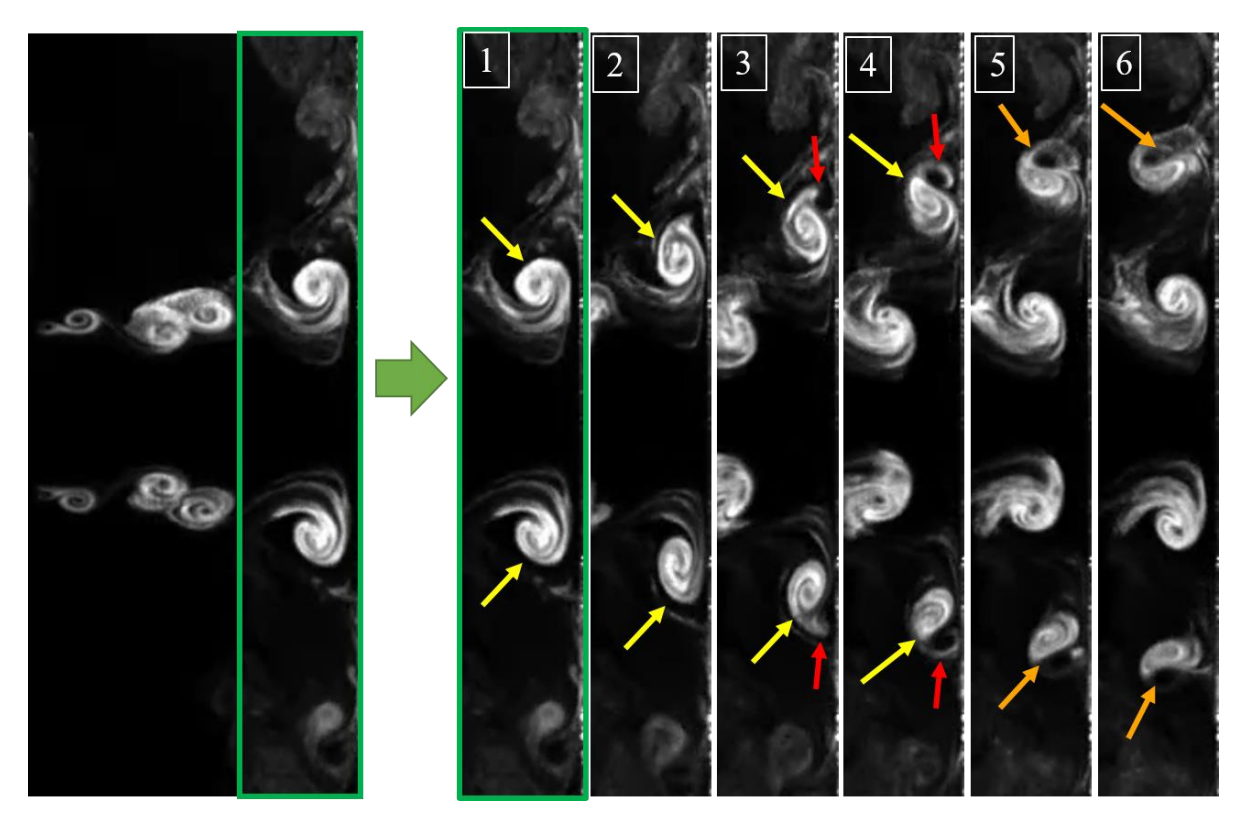


Figure 32 Vortex-wall interaction at H/D=2 for the natural case: full image at one instant (left) and time sequence of the near-wall view (right). Flow is from left to right and the time between images is 0.5 ms, $\Delta t U_i/D=0.19$. Arrows indicate particular vortex structures

3.1.3 Quantitative analysis

To quantify the occurrence frequency of the double-paired symmetric vortex structure, a pattern recognition scheme is used. To implement this scheme, an image frame that represents this structure is selected as a template (e.g. see the "reference" image in Figure 33). Because the double-paired structure occurs at a frequency of 250 Hz ($St_D = 0.635$), the entire frame sequence for a given case is partitioned into cycles with a period of 250 Hz. The template is first correlated with all images in the first cycle in the sequence to find the highest correlation. The value of this correlation coefficient ($0 \le R_{xy} \le 1$, with unity representing perfect matching) and its time of occurrence in the cycle is recorded. Subsequently, the template is correlated with the image that occurs at the same point in the cycle for all subsequent cycles. However, given that there is some jitter in the periodicity of the vortex structures, the correlation is done for a few images centered

around the expected time of occurrence of the template vortex pattern in the cycle (spanning $\pm 17.5\%$ of the cycle period). The image with maximum correlation and its occurrence time within the cycle are then recorded.

To quantify the occurrence frequency, a threshold is set on the correlation coefficient to identify time instances where the structure is the double-paired symmetric vortex (R_{xy} higher than the threshold). Using visual inspection of many images, the threshold is set to a cross-correlation coefficient of 0.7. Visually, images with a cross-correlation of less than 0.7 show clear divergence from the reference image, while images with cross-correlation of more than 0.7 show good correspondence with the reference image. This is exemplified in Figure 33 and Figure 34, which show a comparison between the reference image and the first three images with $R_{xy} < 0.7$, and the first three images with $R_{xy} > 0.7$ for bi-modal forcing at $\phi = 105^{\circ}$. Figure 35 and Figure 36 show the same comparison as the previous two figures but for $\phi = 165^{\circ}$.

Figure 33 clearly shows the asymmetric structure identified by correlation coefficients below the threshold. The images depict pairing or at least interaction between two vortices leading to a larger flow feature near the wall in the top shear layer. In the bottom shear layer, the vortex cores remain relatively smaller and clearly staggered in formation relative to the top shear layer. For $R_{xy} > 0.7$ (Figure 34), the structures are more, but not perfectly, symmetric and they exhibit vortex interactions that lead to a larger structure near the wall in both the top and the bottom shear layer. It is noted here that the images have R_{xy} that are not much higher than the threshold, where some ambiguity in identifying the type of the structure is expected. Moreover, the case examined in Figure 34 corresponds to bi-modal forcing at $\phi = 105^{\circ}$, where the largest values of $C_{w,min}$ are observed in Figure 25 for this type of forcing. Thus, it is expected that this is the case with the least

occurrence of the double-paired symmetric structures and some of the identified structures of this type could be more precisely labeled as *quasi* double-paired symmetric.

Figure 35 and Figure 36 lead to similar conclusions as Figure 33 and Figure 34 but with a notable difference. Since in this case $\phi=165^\circ$, the forcing condition corresponds to the narrowest particle-free core, it is expected that the most persistent double-paired symmetric structures will be observed. Thus, unlike Figure 34 for $\phi=105^\circ$, images identified with R_{xy} higher than the threshold (Figure 36) exhibit a clear symmetric double-paired structure. On the other hand, images identified below the threshold (Figure 35) do not depict an asymmetric structure. However, they are taken not to represent the double-paired symmetric state as pairing is clearly not complete prior to the vortices reaching the wall (which is most relevant to the shear layer spread). This is a significant point to note, particularly when including the natural jet and the jet forced at the fundamental frequency only in the analysis, that structures identified by $R_{xy} < 0.7$ indicates the absence of a double-paired symmetric structure. The actual structure that is present, however, could be asymmetric, or symmetric with no vortex pairing or merging leading to the vortex size seen in double pairing.

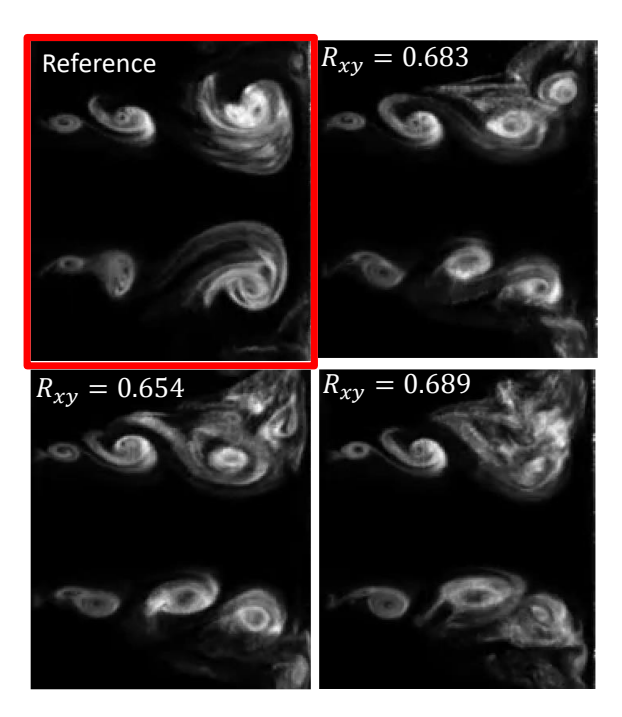


Figure 33 A comparison between the reference image and the first three images with $R_{xy} < 0.7$ for bi-modal forcing at H/D = 2 and $\phi = 105^{\circ}$ and forcing level of 0.3%

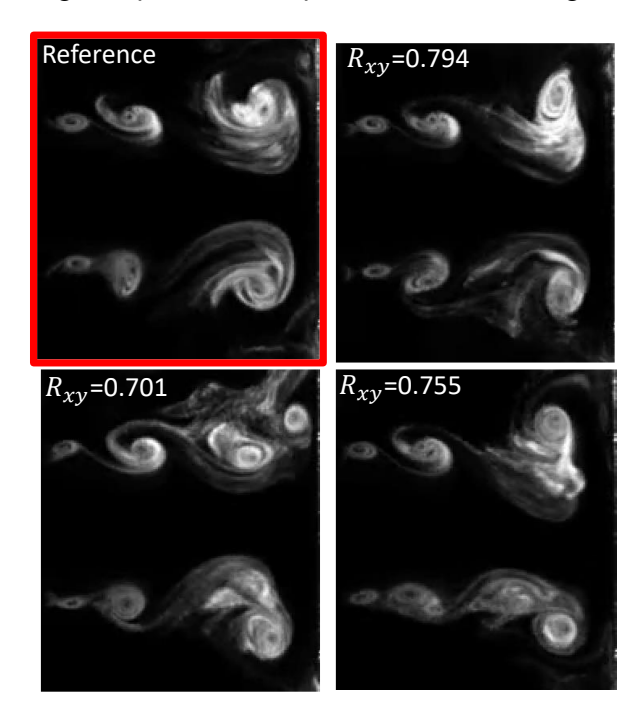


Figure 34 A comparison between the reference image and the first three images with $R_{xy} > 0.7$ for bi-modal forcing at H/D = 2 and $\phi = 105^{\circ}$ and forcing level of 0.3%

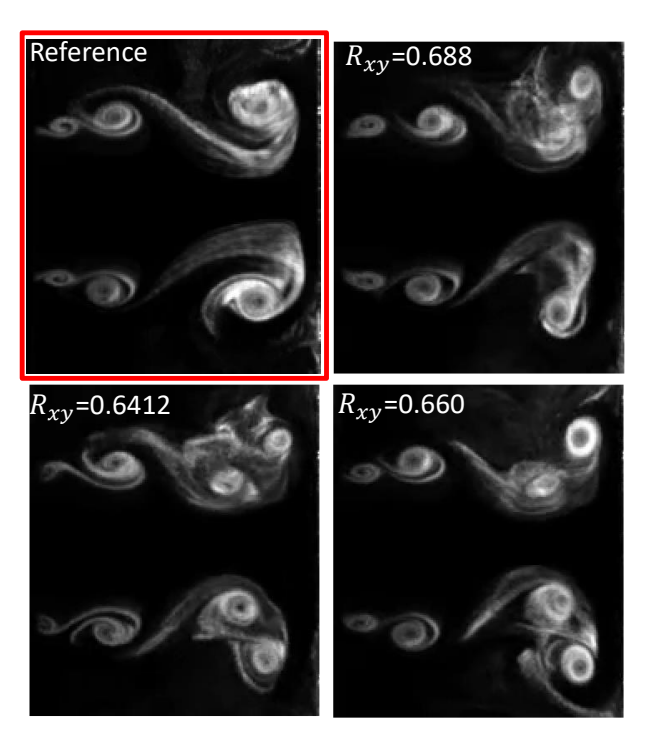


Figure 35 A comparison between the reference image and the first three images with $R_{xy} < 0.7$ for bi-modal forcing at H/D = 2 and $\phi = 165^{\circ}$ and forcing level of 0.3%

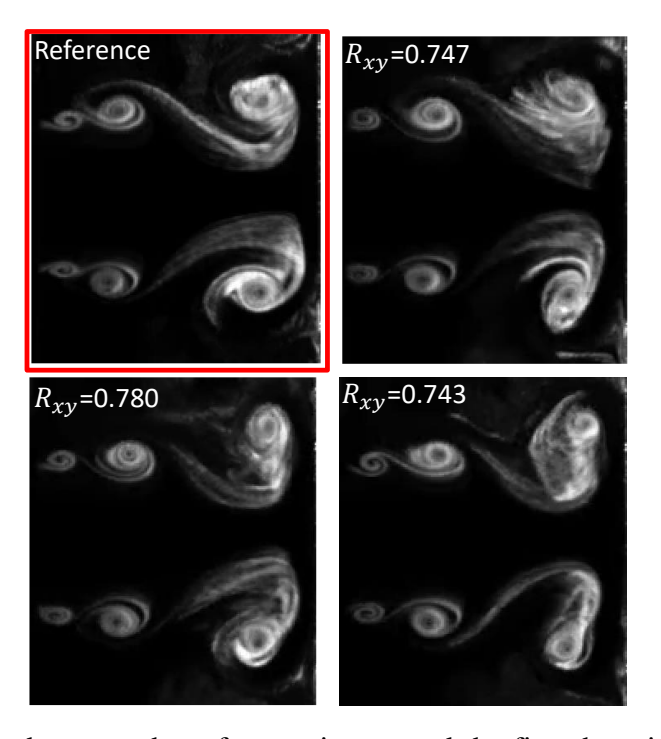


Figure 36 A comparison between the reference image and the first three images with $R_{xy} > 0.7$ for bi-modal forcing at H/D = 2 and $\phi = 165^{\circ}$ and forcing level of 0.3%

The probability density function (pdf) is utilized to quantify the distribution of the crosscorrelation (R_{xy}) values for different cases. Figure 37 shows the pdf for the natural case compared with the pure-harmonic forcing cases. The bin width of the pdfs is selected to provide a balance between minimizing data scatter and revealing the pdf shape. Too narrow of a bin width leads to large data scatter and too large of a bin obscures the pdf shape. For all cases, the number of pdf bins is 20 and the total number of data points distributed among the bins is approximately 495. Figure 37 shows that the pdf for the natural jet is clearly biased towards values below the 0.7 threshold, indicating the relative rarity of the double-paired symmetric structure, as discussed previously. This bias is reduced by forcing at the fundamental or the subharmonic frequency, consistent with the visually observed promotion of the double-paired symmetric structure via forcing in the images. The pdf shape is quite different, however, depending on the frequency of forcing. For the fundamental frequency, the pdf becomes broad-peaked (ignoring the scatter in the data), with a substantial area of the pdf occupying the range $R_{xy} > 0.7$. On the other hand, with subharmonic forcing, the pdf becomes dual-peaked (i.e. bi-modal; not to be confused with the bimodal mode of forcing) and also exhibits a substantial area that corresponds to the double-paired symmetric structure. The bi-modal distribution presumably corresponds to the switching between the symmetric and asymmetric structures identified visually earlier. This switching is cpatured in the pdf supposedly since the peak probability for both of these modes is of similar magnitude.

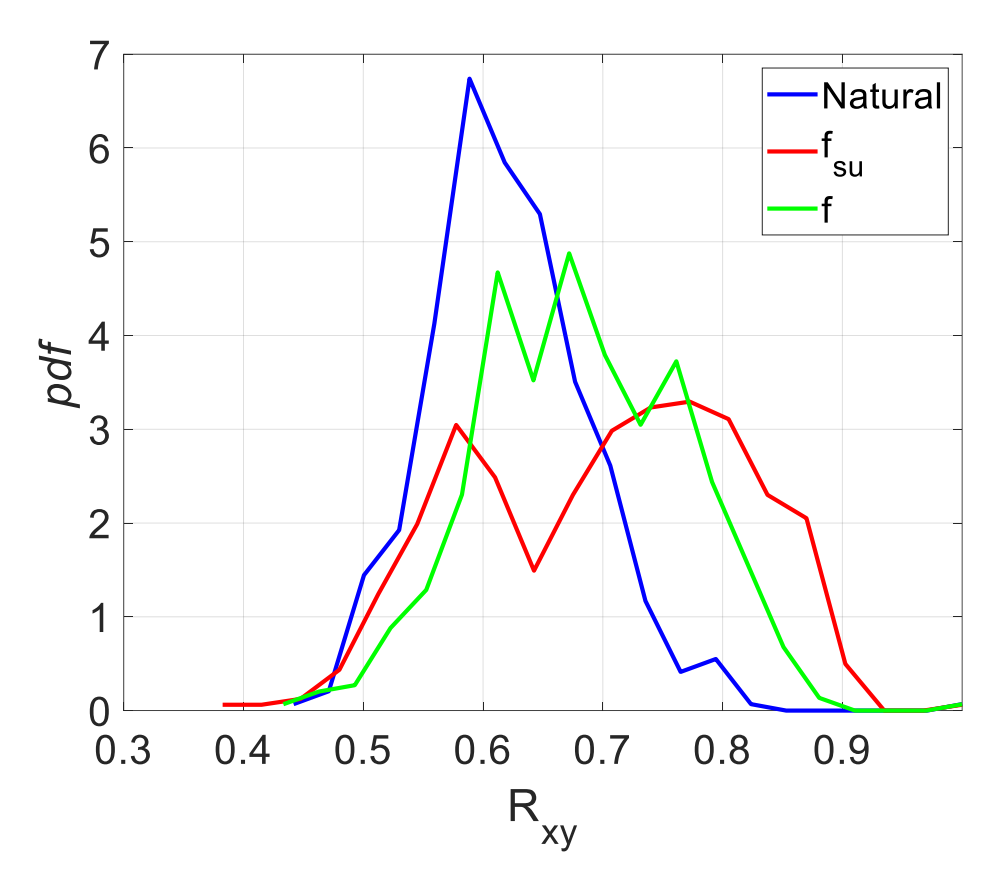


Figure 37 Probability density function of the cross-correlation coefficient resulting from pattern recognition applied to the visualization images of the natural jet and the jets forced using pure harmonic forcing at H/D=2 and forcing level of 0.3%

To inspect the pdfs of the cases with bi-modal forcing, the pdfs are first curve-fitted to make it easier to compare many pdfs on the same plot despite data scatter. Because the pdfs generally exhibited some skewness, a Gaussian distribution function is not a good candidate to represent the pdfs. Several distribution types are examined and the one that provides the best fitting quality is a "t location-scale distribution". According to MatLab, which is used for distribution fitting, the "t location-scale distribution" is useful for modeling pdf distributions with heavier tails and is related to the Student's t distribution. The distribution type is, however, selected here purely empirically based on the quality of the fit across all cases. It is not intended to imply something about the underlying physics. Figure 38 demonstrates the quality of the pdf fits by depicting a

comparison between the pdf data points and the pdf fit for the two cases exhibiting the narrowest and widest $C_{w,min}$. The circles represent the pdf data points and the solid line represents the pdf fit. The data points and the fit show a similar trend, which makes the pdf fit comparison reliable.

Figure 39 displays the pdf fits for the forced jet with the bi-modal scheme for every other intermodal phase tested (i.e. ϕ increments of 30°). The pdf is predominantly focused on the range $R_{xy} < 0.7$ for $\phi = 90^{\circ}$, and on the range $R_{xy} > 0.7$ for the cases of $\phi = 0^{\circ}$, 30°, 60°, 120°, and 150°. This indicates that at $\phi = 90$ °, the jet rarely exhibits the double-paired symmetric vortex structure. Instead it is dominated by the disorganized asymmetric structure discussed in Figure 31. As the intermodal phase is increased from 90° towards 150°, the pdf peak shifts gradually towards the range $R_{xy}>0.7$ with $\phi=150^\circ$ producing the highest peak, and narrowest pdf for all cases. This indicates the best organization and better cycle-to-cycle consistency for $\phi = 150^{\circ}$ case among all cases, and the dominance of the double-paired symmetric vortex structure in this case. Further increase in the phase (back to $\phi = 0^{\circ}$ then up to 90° given the uniqueness of ϕ only in the interval $0^{\circ} \le \phi \le 180^{\circ}$) leads to reduction in the peak and widening of the pdf (i.e. more cycleto-cycle variation of the vortex structure), and gradual shift of the pdf peak towards $R_{xy} < 0.7$ (i.e. less occurrence of the double-peaked symmetric structure). It is also noteworthy that while the pdf for the natural case (Figure 37) and $\phi = 90^{\circ}$ (Figure 38) look similar, the underlying structure in one case is dominated by a symmetric structure that rarely exhibits double pairing (natural case), while for $\phi = 90^{\circ}$, the dominant structure is the disorganized asymmetric one.

The pdfs are used to compute the time percentage (T_p) for which the double-paired symmetric structure is present for all cases. This is accomplished by integrating the pdfs to find the area under the curve in the range $R_{xy} > 0.7$. The larger the time percentage, the more persistent

the double-paired symmetric structure, and hence the narrower the particle-free core and the faster the shear layer spread. Figure 40 shows the resulting T_p values for all cases, while

Figure 41 shows only the cases with bi-modal forcing, along with a smoothing spline fit that is used to only highlight the trend of the data. Figure 40 shows that indeed the natural jet exhibits the least double-paired symmetric structure, comparable with the bi-modal forcing cases at $\phi = 90^{\circ}$ and 105° . These cases also exhibit a wide particle-free core. For all bi-modal cases, the variation of T_p with ϕ is almost a mirror image of the variation of $C_{w,min}$ (Figure 25). This supports the hypothesis made earlier that the intermodal phase changes the fraction of the time for which the double-paired symmetric vortex structure is present. The larger this fraction is (i.e. the more persistent the double-paired symmetric structure is), the narrower the particle-free core, and the faster the spread of the shear layer on average.

It is interesting to compare Figure 41 to Figure 42, taken from the study of Husain and Hussain [7]. The latter figure displays the streamwise velocity fluctuation root mean square normalized by the jet exit velocity versus the intermodal phase of bi-modal forcing of a non-impinging jet. Because the jet conditions (Reynolds number, geometry, etc.) in Husain and Hussain [7] are different from the present study, the value of the intermodal phases cannot be compared on a one-to-one basis. However, in both studies, the phase is varied over the full range of $0^{\circ} \leq \phi < 180^{\circ}$. The qualitative similarity between the results in

Figure 41 and Figure 42 (for the subharmonic frequency f_{su}) is striking. In both cases, the data indicate bi-modal forcing promotes vortex pairing over a relatively wide intermodal phase range with attenuation occurring in a narrow range.

It is important to note that the results in Figure 41 while relevant to double pairing; i.e. f/4, the behavior for f/2 is expected to be the same. Specifically, accelerated second pairing goes hand in hand with accelerated first pairing (which is seen visually in the videos). It follows, that the present study is qualitatively consistent with the earlier work by Husain and Hussain [7]. More importantly, the present work adds deeper insight into the findings of Husain and Hussain [7]. The latter study interprets the promotion of pairing through the overall fluctuation energy, which is an integrated quantity. The present study examines pairing through a pdf of the evaluation of the instantaneous structural features. This enables us to postulate that the energy enhancement (or attenuation) of the subharmonic mode in Husain and Hussain reflects the increase (or decrease) in the time fraction in which vortex pairing occurs, and not necessarily an increase in the strength of the paired vortex structures.

Another interesting way of viewing the current results is to compare pure-harmonic excitation at the subharmonic frequency to that with bi-modal forcing at $\phi=150^\circ$ or 165° . It is well known that forcing a jet at the subharmonic frequency promotes vortex pairing. However, it is evident from the current results that the promoted structure is not stable and it flip-flops between the symmetric and asymmetric states. It is not known if this flip-flopping is a feature of the impinging jet, or if it is also relevant to the non-impinging jet. What is clear, though, is that for the impinging jet, the structure can be stabilized by adding the fundamental frequency to the subharmonic forcing scheme with a carefully selected intermodal phase. Specifically, in this work, it is found that at $\phi=165^\circ$, a consistent and stable symmetric double-paired structure is produced with a small variation from cycle to cycle. This is reflected in the narrowness of the pdf in Figure 39 and its focus in the range $R_{xy}>0.7$.

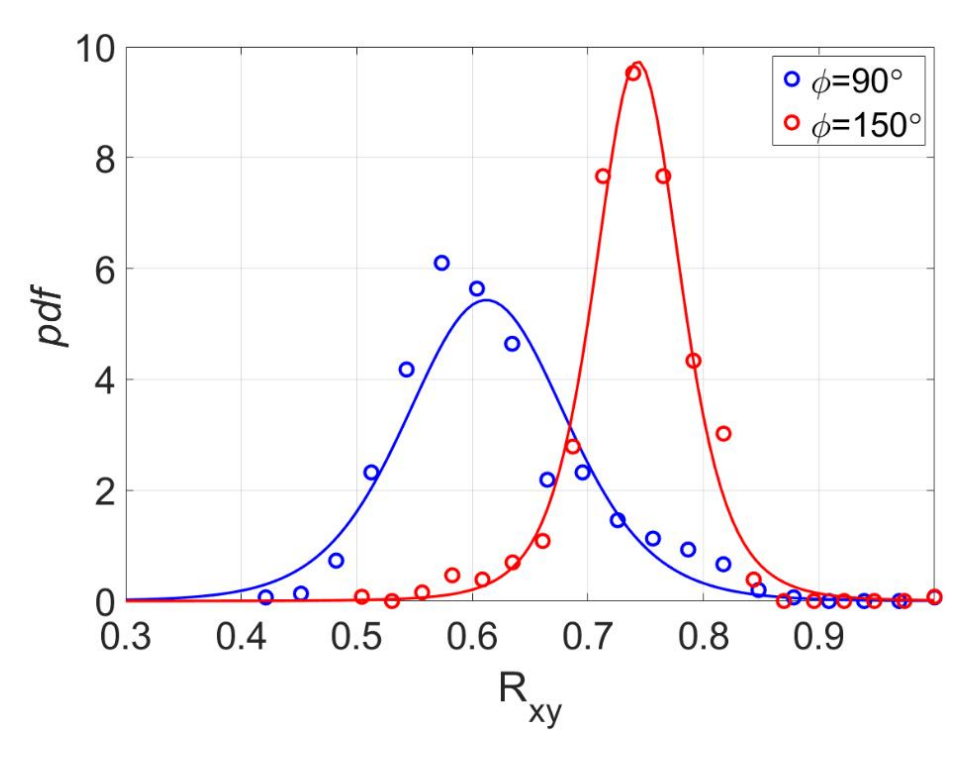


Figure 38 Probability density function fit with data for bi-modal forcing at H/D=2 and $\phi=105^\circ$ and 165° and forcing level of 0.3%

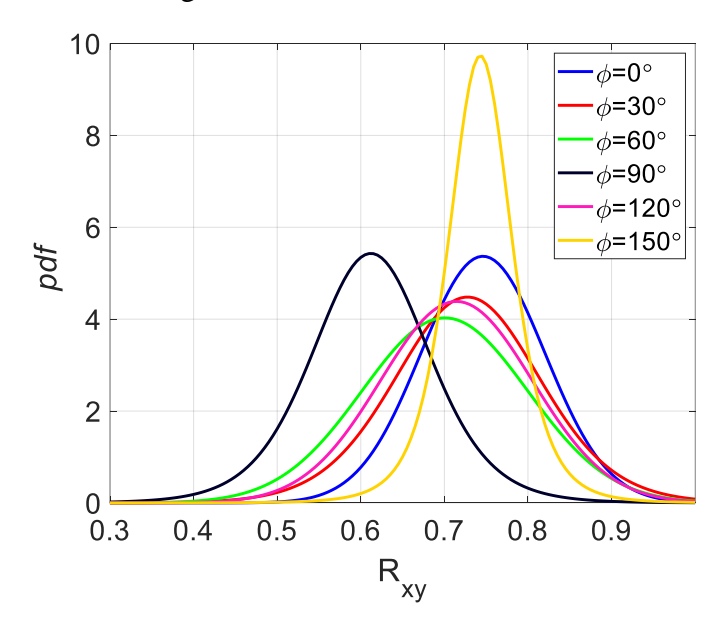


Figure 39 Probability density function fit for bi-modal forcing at H/D=2, AR=1 and 0.3% amplitude, and different bi-modal phases spanning the range $0^{\circ} \le \phi < 180^{\circ}$

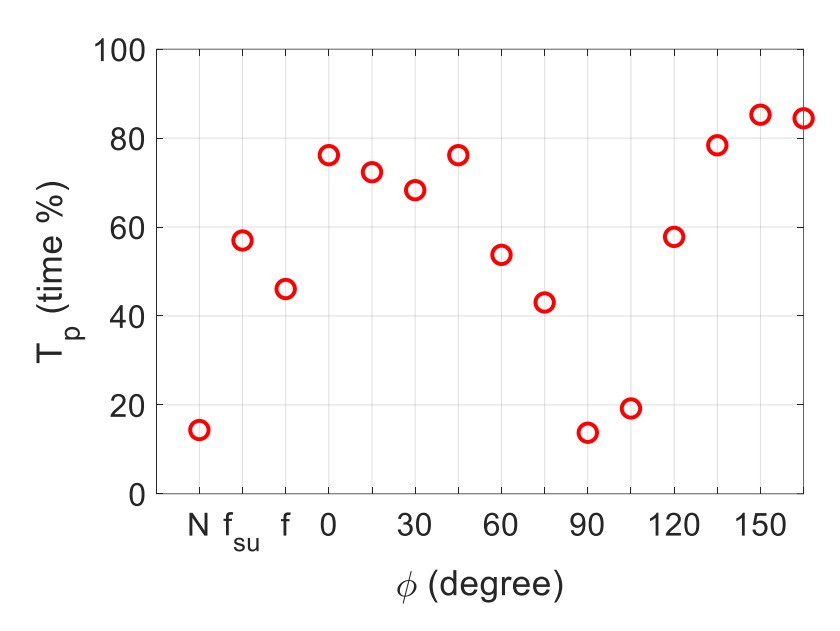


Figure 40 Time percentage when the double-paired symmetric vortex structure is present for all cases at H/D=2: N represents the natural case, f_{su} forcing at the subharmonic frequency, f forcing at the fundamental frequency, and ϕ the intermodal phase for bimodal forcing with AR=1, and 0.3% amplitude

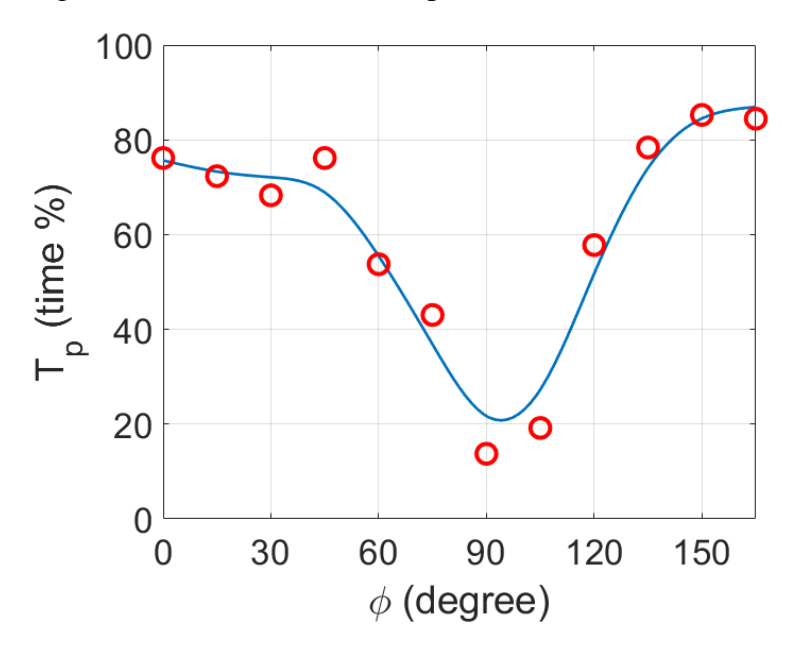


Figure 41 Time percentage when the double-paired symmetric vortex structure is present for bimodal forcing at H/D=2, AR=1, and 0.3% amplitude. The solid line is a smoothing spline curve fit used to capture the overall trend of the data

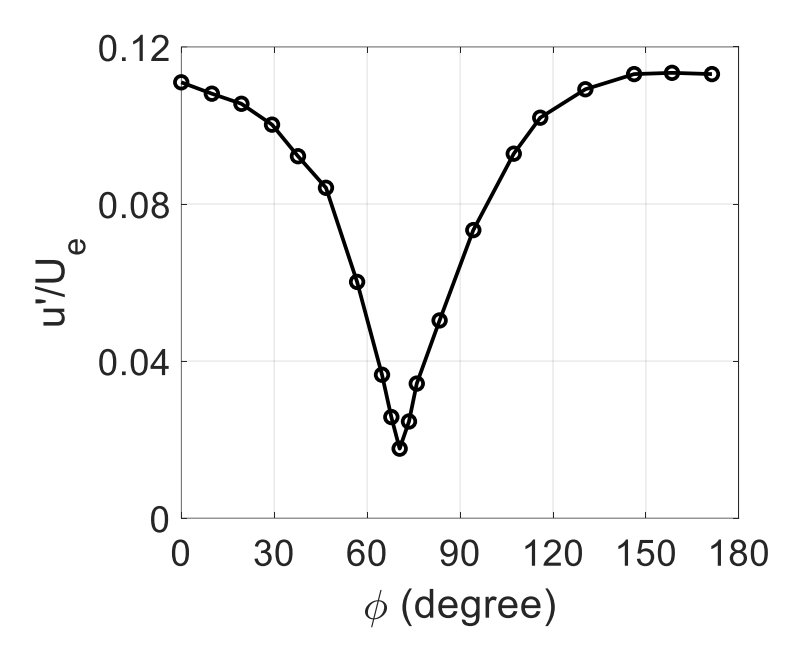


Figure 42 Subharmonic RMS streamwise velocity fluctuation at $x/\theta_e = 8$ versus intermodal phase, replotted from the work of Husain and Hussain [7]. U_e and θ_e are the exit jet velocity and boundary layer momentum thickness respectively

3.2 Forcing Amplitude Level

The forcing amplitude can have a significant effect on the jet structure development. Due to the speaker becoming hot and the limited dynamic range of the microphones used to determine the forcing level, an amplitude higher than the 0.3% utilized so far is not possible to achieve. Therefore, a smaller forcing amplitude of 0.1% is used to check the effect of forcing amplitude on the flow structure and organization, and compare the effect to the higher forcing amplitude (0.3%).

Figure 43 depicts the time percentage of the double-paired symmetric structure plotted versus the intermodal phase for bi-modal forcing at H/D=2, AR=1, and a forcing level of 0.1%. The figure shows significantly less time percentage of the organized structure in comparison to Figure 41 for the higher forcing amplitude. The time percentage dependence on ϕ in Figure 43 does not show a clear trend like the higher amplitude case. The time percentage approximately varies between 10% and 40 % at a forcing amplitude of 0.1%, while the time percentage of all cases at 0.3% approximately varies between 10% and 90%. This shows significantly less effect

of the intermodal phase on the persistence of the double-paired symmetric structure, and depicts a less organized structure at a smaller forcing amplitude.

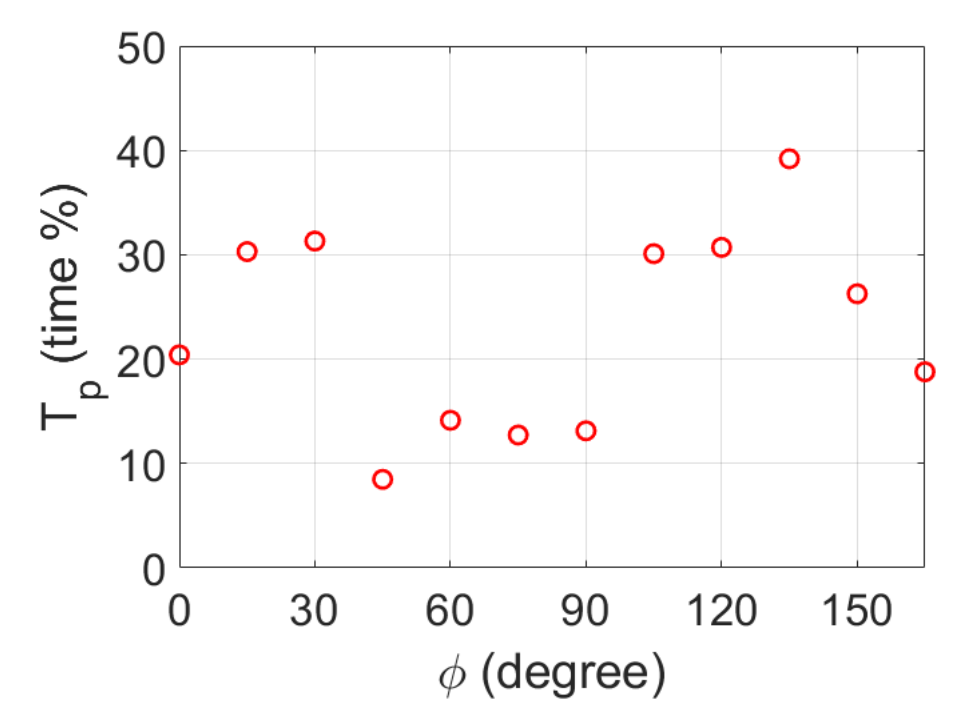


Figure 43 Time percentage when the double-paired symmetric vortex structure is present for bimodal forcing at H/D = 2, AR = 1, and 0.1% amplitude

What is not captured in Figure 43, but seen in the time-resolved visualization, is the nature of the vortex structure in the reduced presence of the double-paired symmetric structure. Intermodal phase values in the vicinity of 150° and 165°, while showing much less double pairing, maintain a generally symmetric and organized structure. The reduced double-pairing events correspond to flip flopping between double pairing and other states. The latter include vortices that only pair once prior to reaching the wall, single-paired vortices that interact but not pair as they reach the wall, and some vortex shredding (where a single-paired vortex grabs a portion of the trailing vortex; see [7]). On the other hand, as seen for forcing at 0.3% amplitude, at ϕ values in the vicinity of 90°, the jet also flip-flops between symmetric and asymmetric states and generally looks more disorganized than at 150° and 165° for forcing at 0.1% amplitude. Thus, while the

lower amplitude forcing reduces the ability of bi-modal excitation to hasten the development of the vortex structure, the intermodal phase still has an effect on the jet structure symmetry and organization.

3.3 Amplitude Ratio (AR)

In addition to the intermodal phase and the forcing level effect, the influence of the amplitude ratio ($AR = a_f/a_{f_{su}}$) of bi-modal forcing on the flow structure of the jet is examined. Figure 44 depicts the time percentage of the double-paired symmetric structure dependence on the intermodal phase at H/D = 2, AR = 0.5, and the higher forcing level of 0.3%. Qualitatively, the dependence on ϕ is similar to that at AR = 1 (Figure 41) but the time percentage shows a narrower intermodal phase range of the less organized asymmetric structures at AR = 0.5 compared to AR = 1; i.e. in the vicinity of $90^{\circ} - 105^{\circ}$. On the other hand, relative to AR = 0.5, the intermodal phase range leading to the less organized asymmetric structure becomes broader with increasing AR to 2 (Figure 45).

Figure 46 displays the results for all amplitude ratios tested on the same plot. As seen from Figure 46, the smallest amplitude ratio (highest subharmonic amplitude relative to the fundamental amplitude) corresponds to the narrowest intermodal phase range producing attenuation of the double-paired symmetric structure. As the amplitude ratio is increased, this range becomes broader but appears to reach a limit as the results for AR = 1 and 2 seem to be similar within the data scatter. It is important to note that, based on the results in Section 3.2, the observed behavior will likely be different at lower forcing amplitudes. Additionally, the behavior outside the range of examined AR values is unknown.

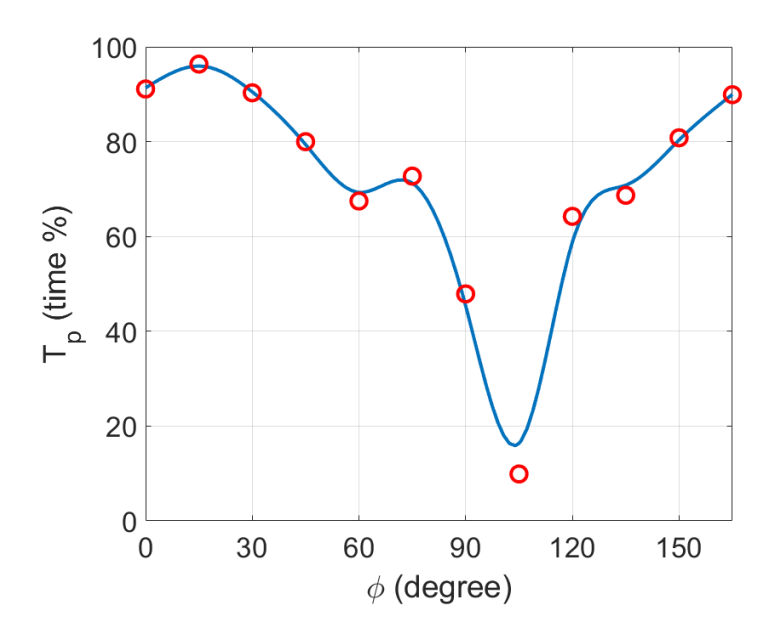


Figure 44 Time percentage when the double-paired symmetric vortex structure is present for bimodal forcing at H/D=2, AR=0.5, and 0.3% amplitude. The solid line is a smoothing spline curve fit used to capture the overall trend of the data

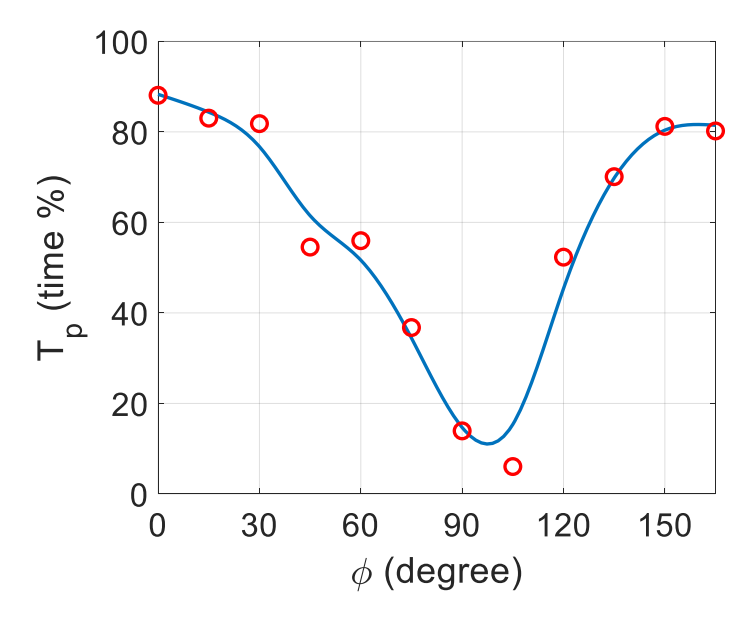


Figure 45 Time percentage when the double-paired symmetric vortex structure is present for bimodal forcing at H/D=2, AR=2, and 0.3% amplitude. The solid line is a smoothing spline curve fit used to capture the overall trend of the data

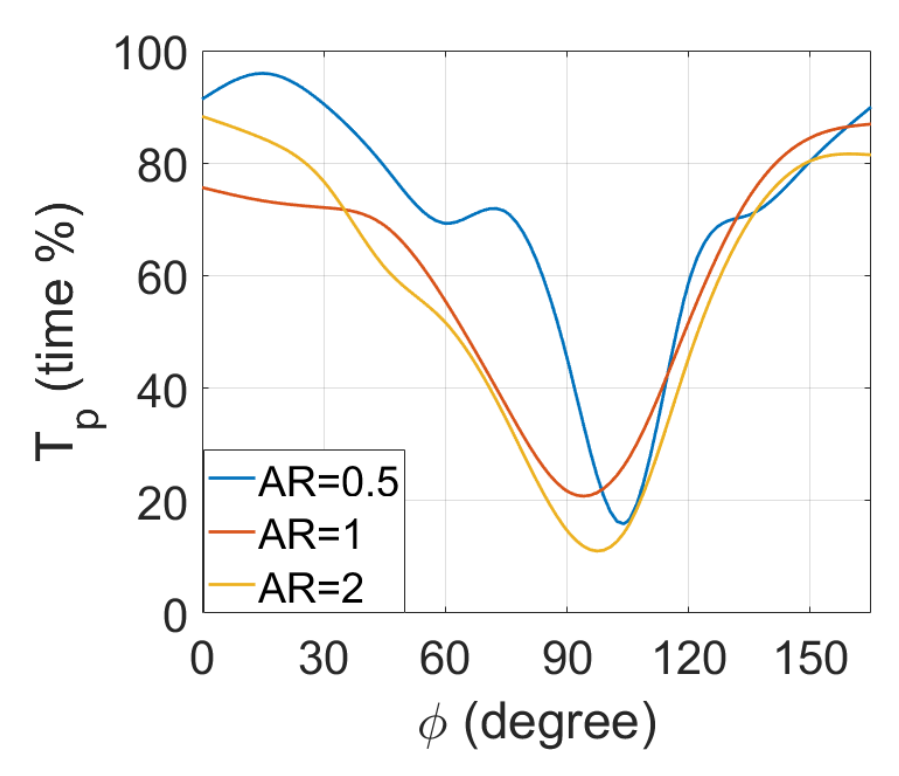


Figure 46 Time percentage when the double-paired symmetric vortex structure is present for bimodal forcing and different AR values at H/D=2 and 0.3% amplitude. The solid line is a smoothing spline curve fit used to capture the overall trend of the data as shown in Figure 41, Figure 44 and Figure 45

3.4 <u>Impingement Plate Location</u>

The location of the impingement plate affects the flow structure development and consequently affects the response of the flow to the forcing. Forcing at H/D=2, 3, and 4 at the same amplitude level and amplitude ratio allows to examine the effect of the impingement plate location on the flow development. Figure 47 and Figure 48 depict the time percentage of the organized structure with respect to the forcing condition. Similar to the results at H/D=2, the natural case shows the least development of the double-paired symmetric structure in both cases (H/D=3) and 4). Interestingly, pure subharmonic forcing exhibits significantly higher organization at H/D=4 than H/D=2 and 3 (Figure 48). This is also seen in the flow visualization videos, where with subharmonic forcing, the double-paired symmetric structure is more consistent from cycle to cycle with increasing H/D with less flip-flopping seen between flow

states. This might suggest that the inermittent behavior seen at H/D=2 is related to the presence of the plate and hence is a unique feature of the impinging jet. With increasing H/D, the plate influence becomes less and the jet behavior through the first two vortex pairings is more like a free jet.

When it comes to bi-modal forcing, similar behavior is observed among H/D=2,3, and 4. This may be seen in Figure 49, where the spline fits of $T_p(\phi)$ are shown. All three cases undergo a rise in the time percentage the double-paired symmetric structure is present with increasing phase $(0^{\circ} < \phi < 45^{\circ})$, followed by a decline $(60^{\circ} < \phi < 90^{\circ})$ and another rise $(105^{\circ} < \phi < 165^{\circ})$.

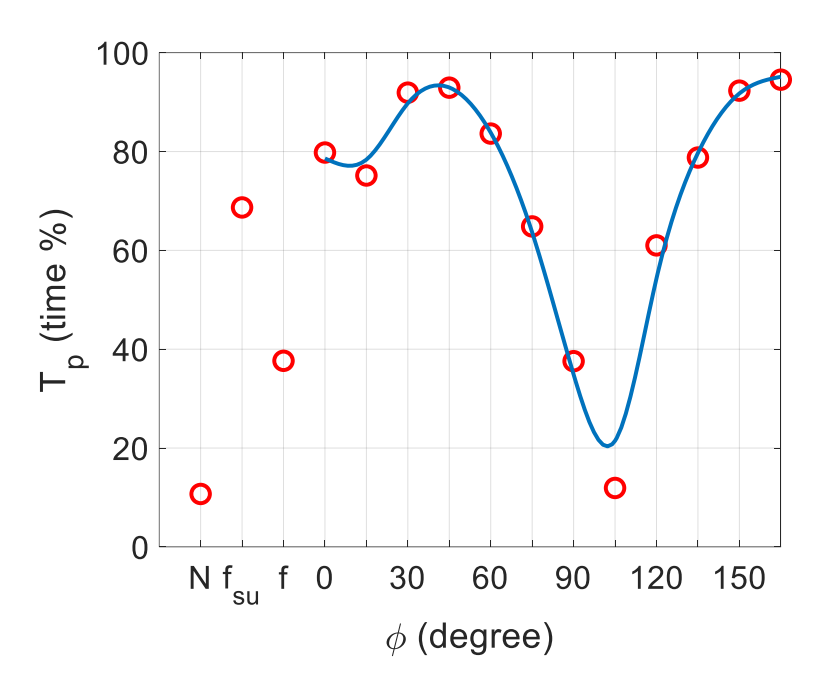


Figure 47 Time percentage when the double-paired symmetric vortex structure is present for all cases (N represents the natural case, f_{su} forcing at the subharmonic frequency, f forcing at the fundamental frequency) at H/D = 3, AR = 1, and 0.3% amplitude

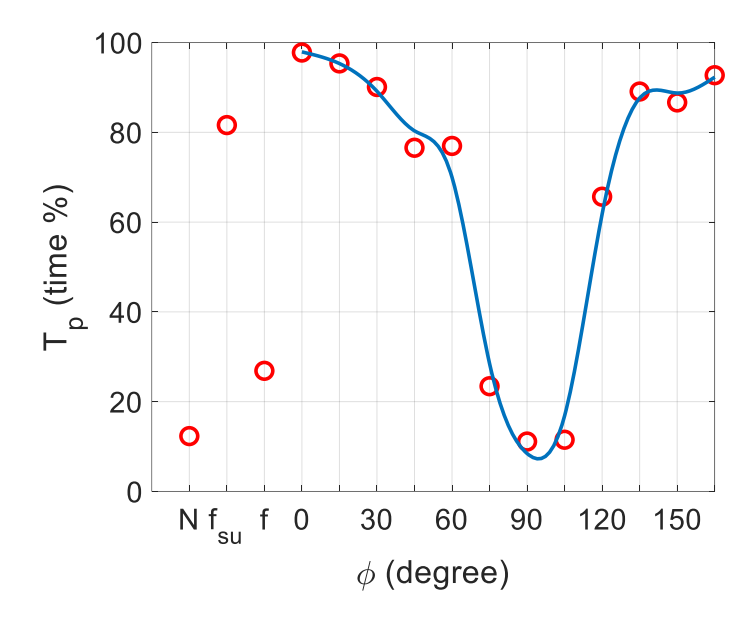


Figure 48 Time percentage when the double-paired symmetric vortex structure is present for all cases (N represents the natural case, f_{su} forcing at the subharmonic frequency, f forcing at the fundamental frequency) at H/D = 4, AR = 1, and 0.3% amplitude

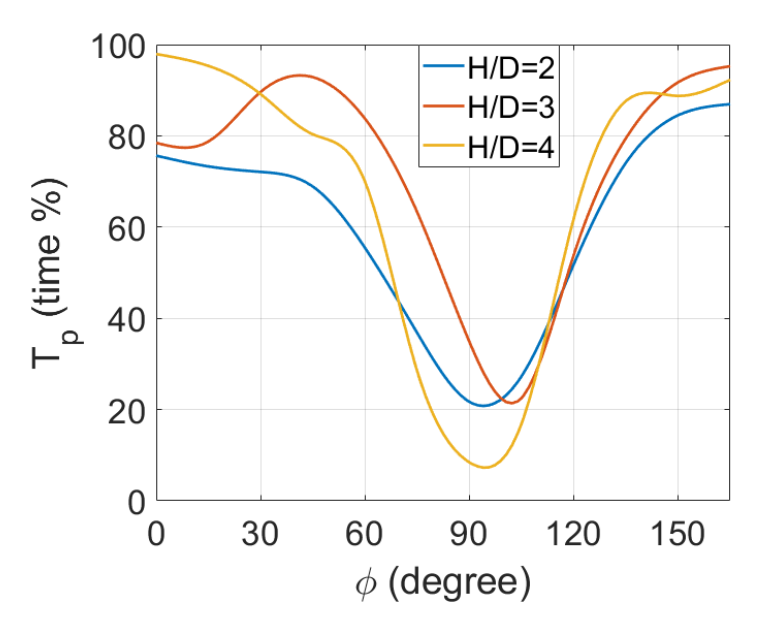


Figure 49 Effect of H/D on the time percentage when the double-paired symmetric vortex structure is present for bi-modal forcing cases at AR = 1, and 0.3% amplitude. Curves are spline fits to the data in Figures 41, 47 and 48

CHAPTER 4. HOT-WIRE MEASUREMENTS

Hot wire is utilized to measure the mean and the unsteady streamwise velocity component in the jet. Results from these measurements are reported in this chapter, which consists of three parts. The first part discusses radial profiles and streamwise evolution of the mean velocity and the broadband fluctuating velocity. The second part presents the streamwise evolution of the power spectra and the energy of the excited modes. The third section focuses on analysis of the modal coherence and phase as they evolve with downstream distance. In all cases, the streamwise evolution is considered along the shear layer center and/or the jet centerline. At a given streamwise location, the shear layer center is selected at the *y* position where the RMS velocity fluctuation is maximum. Information along the shear layer center is relevant to analyzing the evolution of the shear layer instability. On the other hand, the jet centerline measurements are influenced by the far-field induced velocity of the jet vortex structures, and hence are best used to analyze the development of the jet vortices.

The focus of the discussion in this chapter is to compare the effect of the different forcing conditions on the jet evolution, its instability, and vortex structure behavior. The forcing conditions considered in the hot-wire measurements are the natural jet (no forcing), fundamental mode forcing, subharmonic mode forcing, and bi-modal forcing at $\phi = 105^{\circ}$ and $\phi = 165^{\circ}$ at AR = 1. The two particular phases of bi-modal forcing are selected based on the results from CHAPTER 3, where it is demonstrated that, over the full intermodal phase range, these two phases correspond to the widest and narrowest particle-free core (i.e. slowest and fastest developing shear layer), respectively. These, in turn, are also found to be associated with the most asymmetric/disorganized, and the most persistent double-paired symmetric vortex structure. The measurements are only focused on the 0.3% forcing level and H/D = 2. Additionally, due to

limitations in the setup, measurements are carried out from the jet exit up to x/D = 1.22 only. Within this domain, there is no directional ambiguity of the flow velocity due to flow turning and vortex interaction with the wall.

4.1 Mean and RMS Radial and Streamwise Velocity Profiles

The radial profiles for all cases are captured over steps of 0.125 mm ($\approx 0.01D$) covering a span of $\pm 0.5 \text{ y/D}$ at x/D = 0.059, 0.118, and 0.275. At x/D = 0.5 and 1, the profiles span is $\pm 0.6 \text{ y/D}$. Figure 50 displays the mean velocity profiles for all five cases and streamwise locations. The mean profile very close to the jet presents a curved velocity profile in the jet core due to the streamline curvature associated with the vena-contracta. This curve flattens gradually in the streamwise direction until it becomes almost flat at x/D = 1. Concurrently, the profile width gets larger with increasing streamwise distance, which reflects the jet spread. The forcing does not seem to affect the mean profiles to any visible extent in Figure 50. This might seem contradictory to the flow visualization results which show an effect on the particle-free core due to the forcing. However, consultation of Figure 26b shows that, within the streamwise range of the hot-wire measurements $(x/D \le 1.22)$, differences in the particle-free core width due to forcing only start to appear around x/D = 1 for subharmonic and bi-modal $\phi = 165^{\circ}$ forcing. These differences do not seem to lead a visible difference in the mean velocity profiles in Figure 50. However, as will be seen later, these two forcing cases do exhibit subtle but detectable effect when it comes to the mean velocity development in x direction on the jet centerline. These differences are not easy to see in Figure 50 given the plotting scale and the limited x locations of the measurements. In addition, the biggest effects on the particle-free core width in Figure 26b is near the location of the $C_{w,min}$, which are not possible to capture in the mean-velocity data within the limited streamwise measurement domain of the hot wire.

Figure 51 depicts the RMS profiles at the same forcing conditions and streamwise locations as in Figure 50. Figure 52 provides a zoomed view of the plots in Figure 51 to reveal the details of the profiles in the shear layer. The RMS profiles very close to the jet lip show different behavior among the different forcing conditions. The natural jet and the fundamental forcing case show a flatter profile in the jet core very close to the jet exit. This profile stays at the low u' value of the jet centerline up to $(r/D \approx 0.4)$, and then u' starts to increase. For, the subharmonic forcing and the bi-modal forcing modes ($\phi = 105^{\circ}$ and 165°), u' starts to increase at a smaller radial location at r/D = 0.1. The wider region of high u' in the latter cases is indicative of the earlier development of the shear layer in response to forcing modes that include the subharmonic. Specifically, in CHAPTER 3 was observed that in these cases, larger vortex structures emerge into the upstream end of the flow visualization domain at the subharmonic frequency, in comparison to the smaller structures at the fundamental frequency. Thus, the wider u' distribution for the subharmonic and bi-modal forcing cases is consistent with the flow visualization observations.

For all cases, the shear layer RMS profiles grow wider with downstream distance, as expected from the growth of the vortical structures and associated spread of the shear layer. Generally, the subharmonic forcing case shows the highest peak and centerline RMS at all streamwise locations. In the streamwise direction, the u' profile at the jet core changes from being flat to parabolic-like while the magnitude of u' increases. This indicates the increasing unsteadiness in the jet core associated with the vortex development. At x/D = 0.5 and 1, the bimodal forcing at $\phi = 165^{\circ}$ and the subharmonic forcing show higher jet centerline and shear layer u' than the rest of the cases (Figure 51d and Figure 51e). This higher RMS value is consistent with the faster and more consistent development of the larger double-paired vortex structures seen for these two cases.

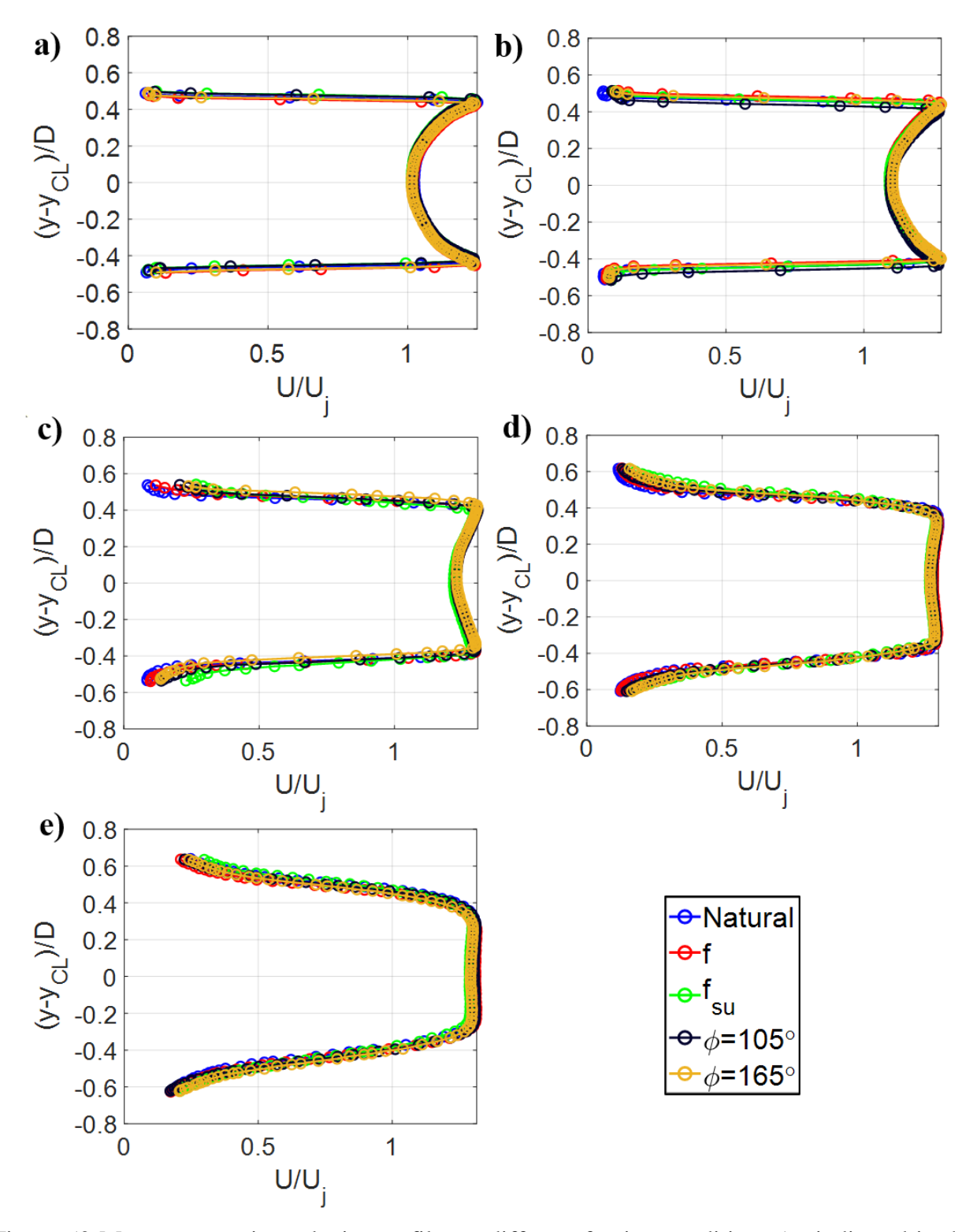


Figure 50 Mean streamwise velocity profiles at different forcing conditions (as indicated in the legend) and streamwise locations. a) x/D = 0.059, b) x/D = 0.118, c) x/D = 0.275, d) x/D = 0.5, e) x/D = 1

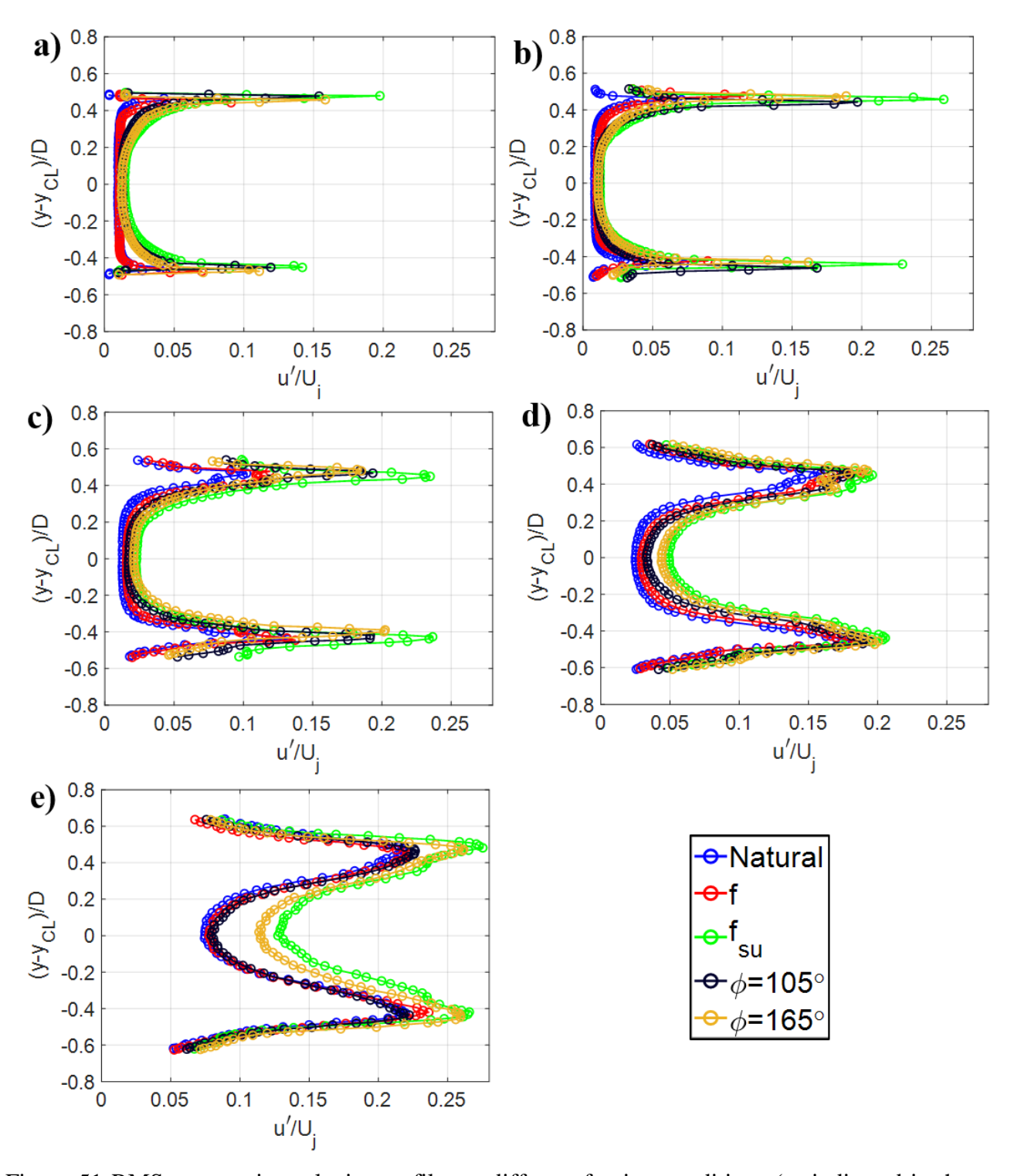


Figure 51 RMS streamwise velocity profiles at different forcing conditions (as indicated in the legend) and streamwise locations. a) x/D = 0.059, b) x/D = 0.118, c) x/D = 0.275, d) x/D = 0.5, e) x/D = 1

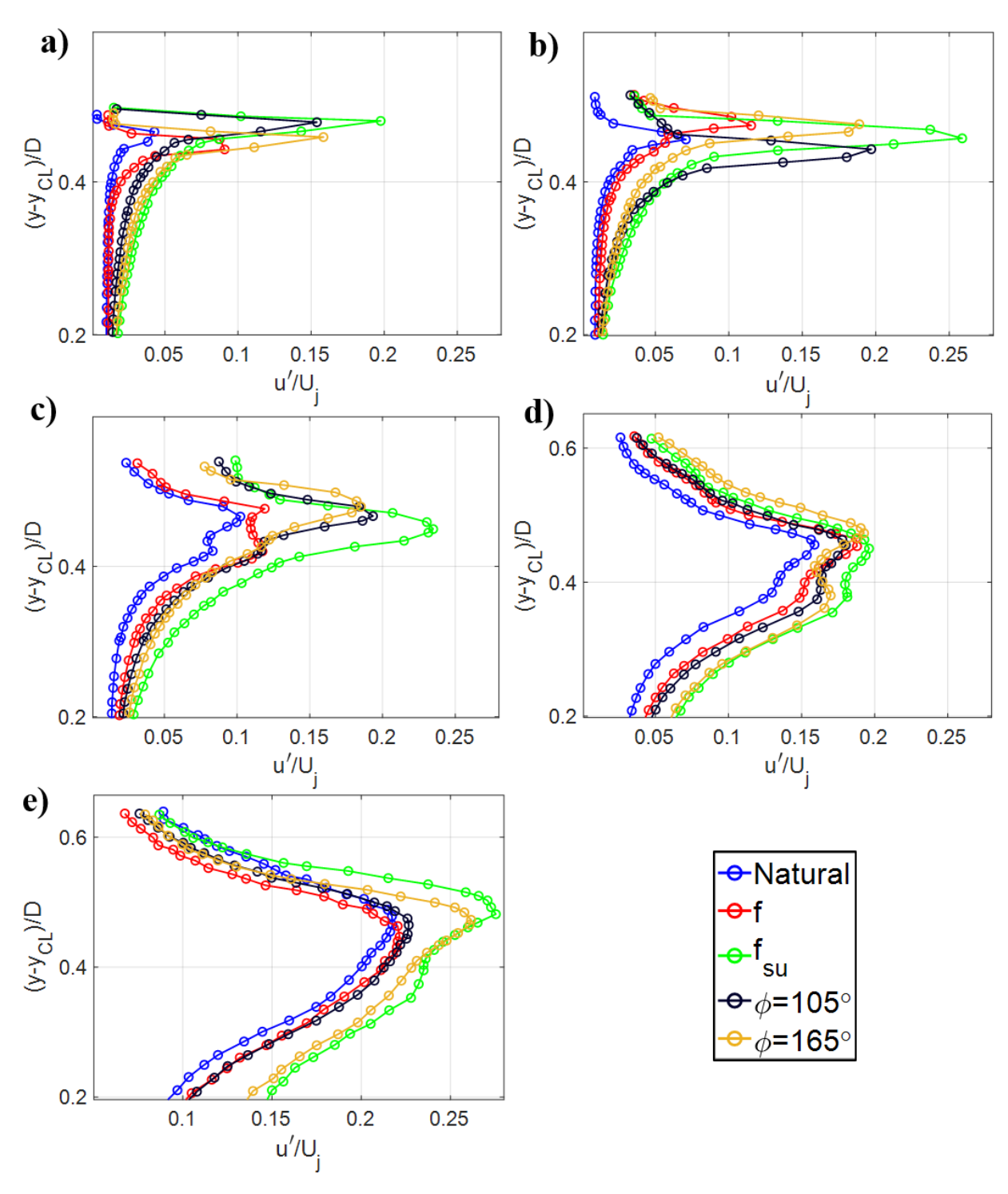


Figure 52 Zoomed RMS streamwise velocity profiles at different forcing conditions (as indicated in the legend) and streamwise locations. a) x/D = 0.059, b) x/D = 0.118, c) x/D = 0.275, d) x/D = 0.5, e) x/D = 1

To examine the streamwise development of the velocity in more detail, data are acquired in small x/D increments of 0.0394 over the range $0 \le x/D < 0.354$, and 0.0787 over the range

 $0.354 \le x/D \le 1.22$ at two cross-stream locations: the shear layer center and the jet centerline. Figure 53 shows the evolution of the RMS velocity along the shear layer centerline in response to the different forcing conditions. The natural jet case and the fundamental forcing case show a generally similar response that is distinctly different from the cases involving the subharmonic frequency in the forcing. The latter cases, which include the pure subharmonic forcing and the two bi-modal cases show a much-accelerated growth of the fluctuation energy with streamwise distance, reaching a local maximum in the vicinity $x/D \approx 0.25$. This maximum, the x location and strength of which are typically used to assess the effectiveness of the forcing [27], is not reached until $x/D \approx 0.6$ in the case of the natural and fundamental forcing jets. This highlights the significance of the presence of the subharmonic frequency in hastening the development of the underlying vortex structure to become maximally energetic closer to the jet exit. Additionally, it is seen that pure harmonic forcing at the subharmonic frequency leads to the largest peak in the fluctuation energy. The local peak magnitude is otherwise compatible between all other cases. Downstream of the first local u' peak, all cases exhibit slow u' growth with downstream distance with the subharmonic forcing case remaining the most energetic for most of the domain. Based on the flow visualization results, bi-modal forcing at $\phi = 165^{\circ}$ leads to a more consistent organized structure while forcing at the subharmonic frequency only is associated with intermittency between symmetric and asymmetric structures. Thus, while forcing at the subharmonic frequency alone causes the strongest energization of the structures and accelerates their development, imposing the fundamental and subharmonic frequency simultaneously at the right intermodal phase leads to equally accelerated development with the most structure organization.

Aside from the growth of the fluctuation energy in the shear layer, the streamwise profile of the velocity along the jet centerline is another indicator that is typically used to examine the

effect of forcing on jet development. For a jet emerging from a contoured nozzle, the *mean* velocity along the jet centerline remains unchanged in the streamwise direction until the end of the potential core, when the shear layer spreads across the full jet width. Farther downstream from the end of the potential core, the mean velocity decays monotonically with downstream distance. If forcing leads to accelerated development of the potential core then the mean jet centerline velocity starts to decay closer to the jet exit. With this in mind, the streamwise evolution of the jet centerline mean velocity is shown in Figure 54 for the different forcing conditions. Unlike the jet exiting from a contoured nozzle, the mean centerline velocity exhibits immediate rise downstream of the jet exit in the range 0 < x/D < 0.75. This rise in the mean velocity is due to the acceleration effect of the vena-contracta, which is a known behavior of the sharp-edged jets. The centerline mean velocity increases until it reaches a maximum at x/D = 0.75, and then it starts to drop at x/D > 0.750.75. The drop with downstream distance is not an indication of the end of the potential core as evident from the mean velocity profiles in Figure 50, where the shear layer clearly remains outside of the jet core. Instead this drop is partially due to an overshoot in the centerline velocity acceleration observed in the non-impinging jet for $Re_D \le 6,000$ (see Figure 78 in Appendix A). In addition, it is expected that the jet may already start to decelerate as it feels the presence of the impingement wall at H = 2D.

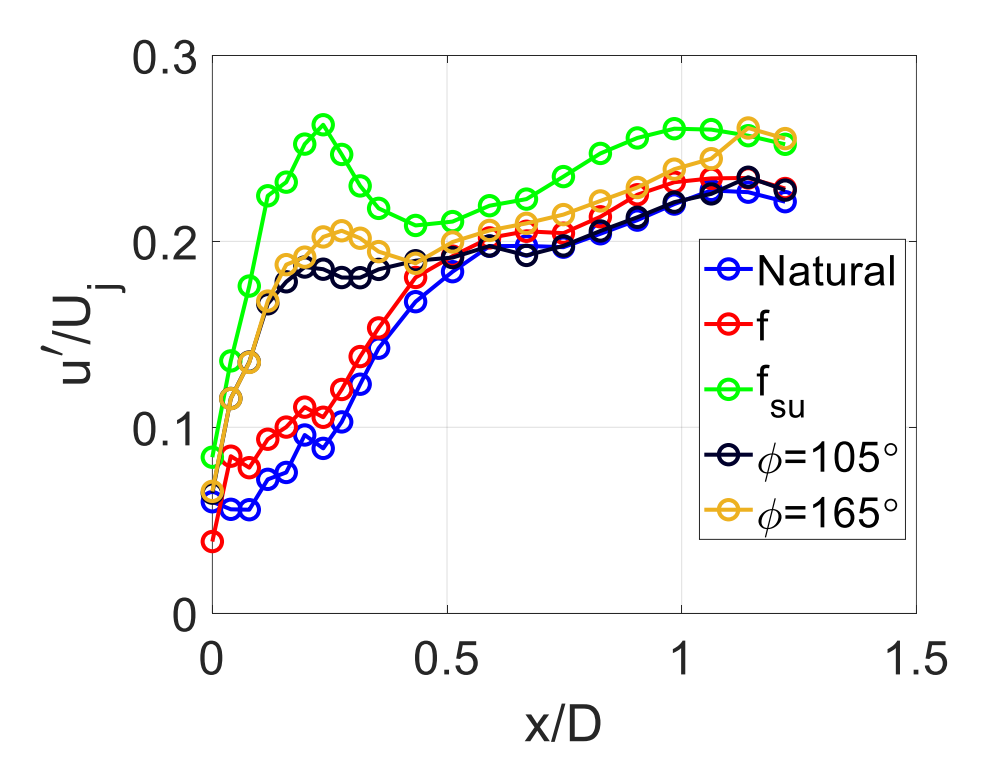


Figure 53 RMS streamwise velocity progression along the streamwise direction on the shear layer center at different forcing conditions

Overall, Figure 53 indicates that jet centerline mean velocity is behaving the same for all cases. This is consistent with the observations made earlier in relation to Figure 50, where it was concluded that the effect on the mean velocity from the different cases is not expected to be significant until the vicinity of the impingement plate, which is outside the domain of the present velocity measurements. As mentioned earlier, there does seem to be a subtle effect, however, on the centerline velocity for the subharmonic forcing and the bi-modal forcing at $\phi = 165^{\circ}$ cases, where the velocity starts to drop below the rest of the cases at around $x/D \approx 0.5$. These are the two cases that exhibit the largest shear layer growth rate of all five cases based on the flow visualization (Figure 26b) and u' results in Figure 51.

While the potential core has not terminated by the end of the hot-wire measurement domain, the centerline velocity fluctuation rises, as seen in Figure 55. This is interpreted as an indication that the centerline velocity fluctuations are connected to the "far field" influence of the

vortical structures as they grow in size and strength with downstream distance. The larger and stronger the vortices are, the larger is their influence. Thus, the RMS magnitudes on the jet centerline are indictive of vortex development, growth and pairing. As illustrated in Figure 55 the subharmonic forcing mode and the bi-modal forcing mode at $\phi = 165^{\circ}$ show the quickest energy growth on the jet centerline with the steepest growth slope. This is consistent with the flow visualization observation of these two cases leading to the best promotion of the double-paired symmetric structure among the five cases considered. The bigger size, strength and persistence of these structures is interpreted as causing the stronger fluctuation energy growth on the jet centerline.

It is worth noting that in both nozzle and sharp-edged *non-impinging* jets, u' on the jet centerline increases to a maximum then subsequently decays. It is known that for a sharp-edged jet without forcing, the maximum is reached around $x/D \approx 8$ [27]. With the application of pure harmonic forcing at the preferred mode frequency, the development of the peak is accelerated such that it forms in the range x/D = 2 - 3. In the present results, the impingement plate at H/D = 2 would be reached before such a peak is formed. Hence, it is not surprising that no maximum is observed in the u' results along the jet centerline in Figure 55.

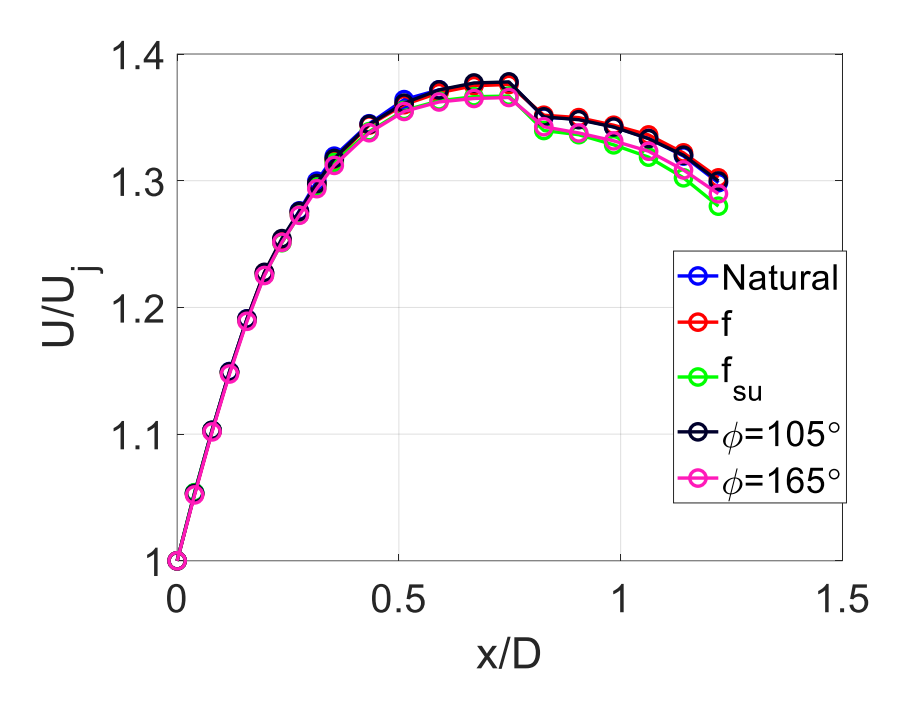


Figure 54 Mean streamwise velocity progression along the streamwise direction on the jet centerline at different forcing conditions

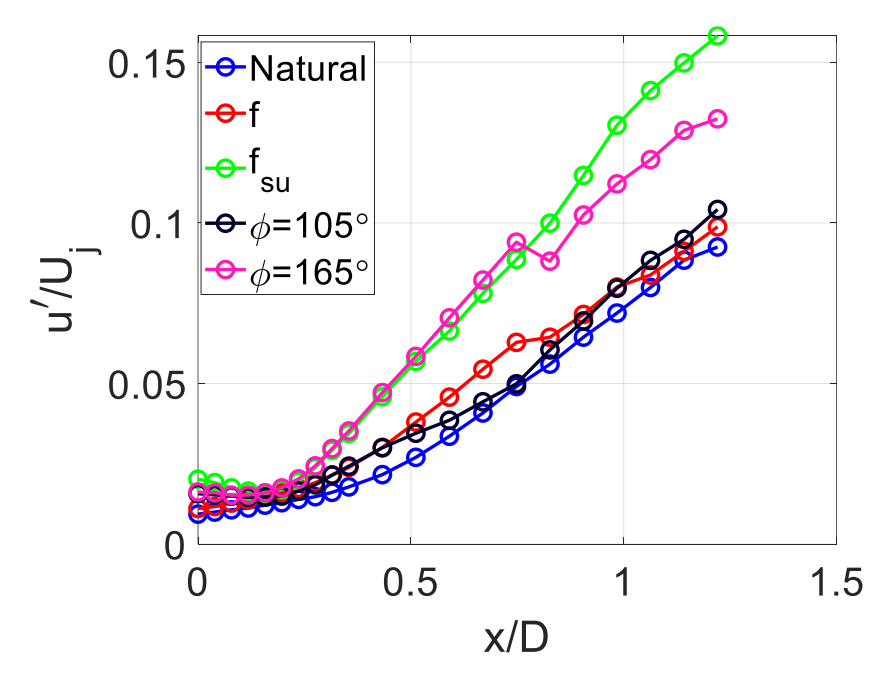


Figure 55 Root mean square streamwise velocity progression along the streamwise direction on the jet centerline at different forcing conditions

4.2 <u>Modal Energy Evolution</u>

The fluctuating velocity receives contributions from the forced modes; (i.e. the fundamental and/or the subharmonic). Additionally, as discovered in the flow visualization analysis, a second pairing event leads to the formation of a significant large-scale vortex structure at a frequency half that of the subharmonic mode. The mode associated with the double pairing is referred to as the second subharmonic and its frequency is denoted by f_{2su} . In this section, the fluctuating streamwise component of each of the aforementioned modes is analyzed to track the modes growth and decay. To this end, the energy of each of the modes is extracted from power spectra, such as those shown in Figure 59, at the modes' respective frequency. Figure 59, which includes an indication of where the modal peaks are, also depicts an additional low-frequency peak at $St_D = 0.457$ that is most visible at the upstream locations. This peak decays with downstream distance, as discussed in CHAPTER 2, and is likely related to unsteadiness contributing to the jet facility's background turbulence level.

4.2.1 Radial modal RMS profiles

Figure 56 depicts the streamwise evolution of the radial profiles of u' for the fundamental mode (u'_f) at five streamwise locations for all five test cases. The plots are zoomed on one of the shear layers to see the details. The RMS profiles are qualitatively consistent with those shown in the literature for a non-impinging jet [7]. Specifically, near the jet exit, the profiles possess a single peak that is aligned in the approximate vicinity of the jet lip $((y - y_{cl})/D = 0.5)$. With increasing downstream distance, this peak shifts towards the jet centerline and a second peak starts to be observed at a larger radial location at x/D = 0.275, for some cases, and x/D = 0.5 for others. Initially, the inside (initial) peak is stronger than the outside one but this relative strength switches with increasing downstream distance. As one might expect, the case where all the forcing energy

is concentrated in the fundamental mode (red symbols) exhibits the largest modal RMS fluctuation at the fundamental frequency. However, the development of the outer peak seems to be happening fastest in the case of the subharmonic and bi-modal $\phi = 165^{\circ}$ forcing, which have been found to lead to the fastest vortex structure development. The fundamental mode energy in the natural jet is much lower than that for all the forced cases. All cases exhibit a growth in the fundamental mode RMS followed by a decay within the range of the measurements.

Not surprisingly, for forcing schemes not including the subharmonic frequency (Natural case in blue symbols and fundamental forcing case in red symbols), the fluctuation velocity at the subharmonic frequency is initially (x/D=0.059) practically zero relative to the other schemes. The fluctuation level grows with downstream distance but remains significantly lower for the natural jet and fundamental forcing cases than the other three cases. The overall shape of the profiles is qualitatively consistent with those reported in the literature [7] for the subharmonic mode. As in the profiles of the fundamental mode (Figure 56), a second peak in u'_{fsu} develops at an outer radial location but it never becomes as significant as the initial/inner peak as seen for the fundamental mode case. The outer peak is particularly observable for the subharmonic and bimodal forcing approaches. These approaches lead to significant growth in the subharmonic energy with the subharmonic scheme yielding the highest energy followed by the bi-modal forcing at $\phi = 165^{\circ}$ then the $\phi = 105^{\circ}$.

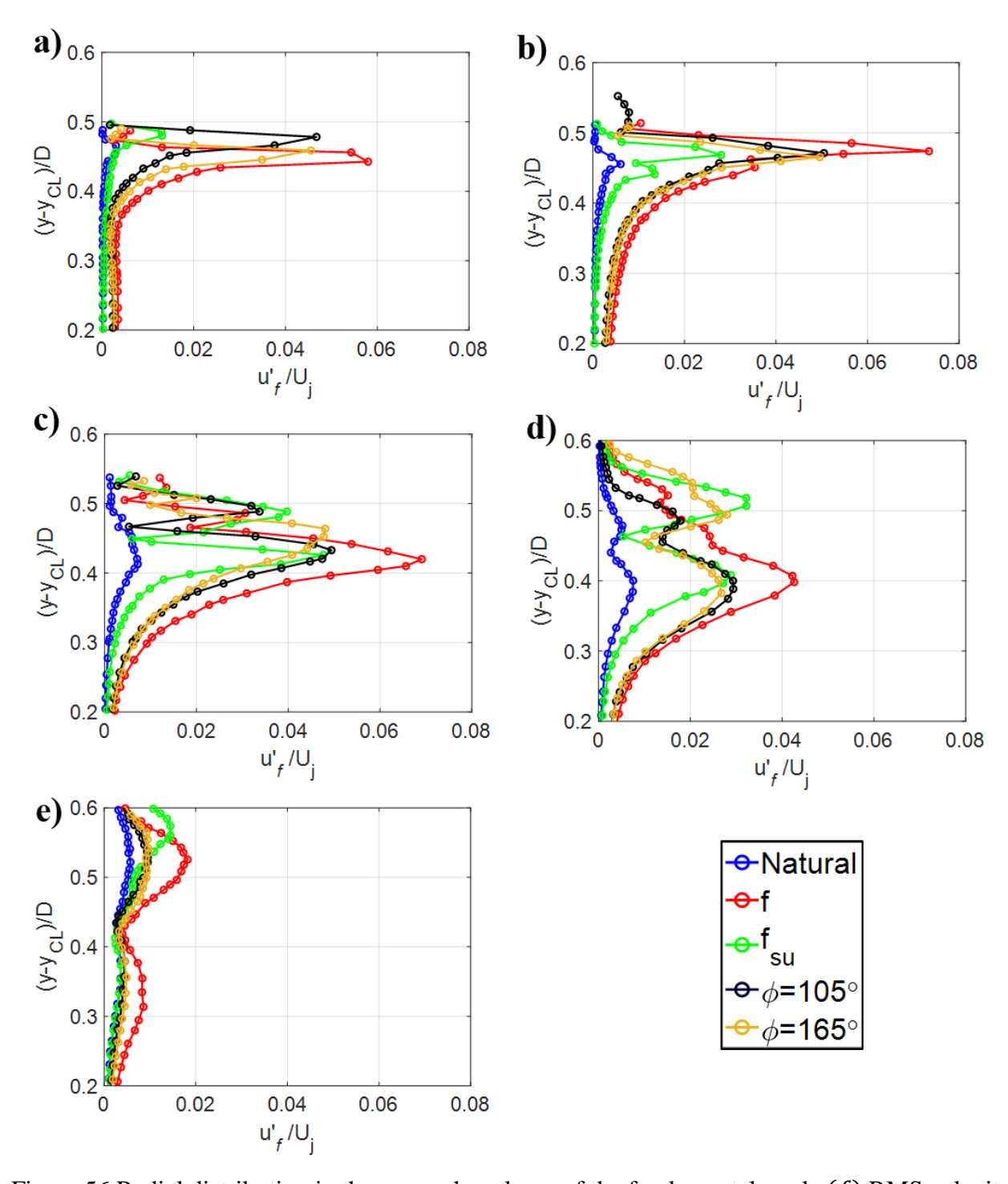


Figure 56 Radial distribution in the upper shear layer of the fundamental mode (f) RMS velocity at different forcing conditions (as indicated in the legend) and streamwise locations. a) x/D = 0.059, b) x/D = 0.118, c) x/D = 0.275, d) x/D = 0.5, and e) x/D = 1

Figure 57 shows similar modal u' profiles as in Figure 56 but for the subharmonic mode $(u'_{f_{su}})$. For the second subharmonic mode, the $u'_{f_{2su}}$ profiles (shown in Figure 58) show the most

fluctuation energy in the case of subharmonic and $\phi=165^\circ$ bi-modal forcing. Recall that of all five cases, these two produce the highest frequency of occurrence of the double-paired symmetric vortex structure and the fastest vortex structure development (Figure 40). Thus, it is not surprising that these two cases exhibit the highest fluctuation energy and growth rate of the second subharmonic mode. An interesting aspect of the radial profiles for these two cases (that is not seen in the other three cases) is the presence of a local peak in the radial profile on the jet centerline at the upstream locations near the exit of the jet (Figure 58a). This peak is of comparable magnitude to that seen in the shear layer at x/D=0.059, a feature that is not seen in the profiles of the fundamental and subharmonic modes. Moreover, unlike the fundamental and subharmonic mode profiles for which the bi-modal case $\phi=105^\circ$ generally exhibits comparable behavior to the subharmonic and bi-modal $\phi=165^\circ$ cases (Figure 56 and Figure 57), when it comes to $u'_{f_{2su}}$, the $\phi=105^\circ$ case behaves more like the natural jet and fundamental forcing cases.

The relatively high fluctuation energy of the second subharmonic mode at the jet exit for the subharmonic forcing and bi-modal $\phi=165^{\circ}$ cases is believed to be the key factor that leads to the most promotion of the double-paired symmetric structure. Since none of the forcing schemes introduces the frequency of the second subharmonic into the jet, the presence of elevated levels of this mode near the jet exit on the jet centerline is hypothesized to originate from a feedback mechanism. One physically plausible mechanism, although still hypothetical, is that as the double-paired symmetric structure reaches the impingement wall, it induces a strong downwash on the stagnation point, increasing momentarily the stagnation pressure. The unsteadiness in the stagnation pressure would then produce corresponding fluctuation in the jet centerline velocity on the stagnation streamline (a "Bernoulli effect"). For the other three cases, the interaction is weaker due to the less frequent double-paired structure (for the natural jet and the fundamental forcing

cases) and the asymmetry and disorganization of the structure (for the bi-modal $\phi=105^{\circ}$). This hypothesis might also clarify the subtle effect on the mean jet centerline velocity distribution of the subharmonic and bi-modal at $\phi=165^{\circ}$ cases dropping below that of the other cases in Figure 53. Specifically, with the stronger interaction of the vortex structure with the stagnation point for these two cases, the peaks in the unsteady stagnation pressure will be higher than the other two cases and the stagnation pressure on average will be higher. This would lead the mean centerline velocity to start slowing earlier once the static pressure on the stagnation streamline reaches the ambient pressure.

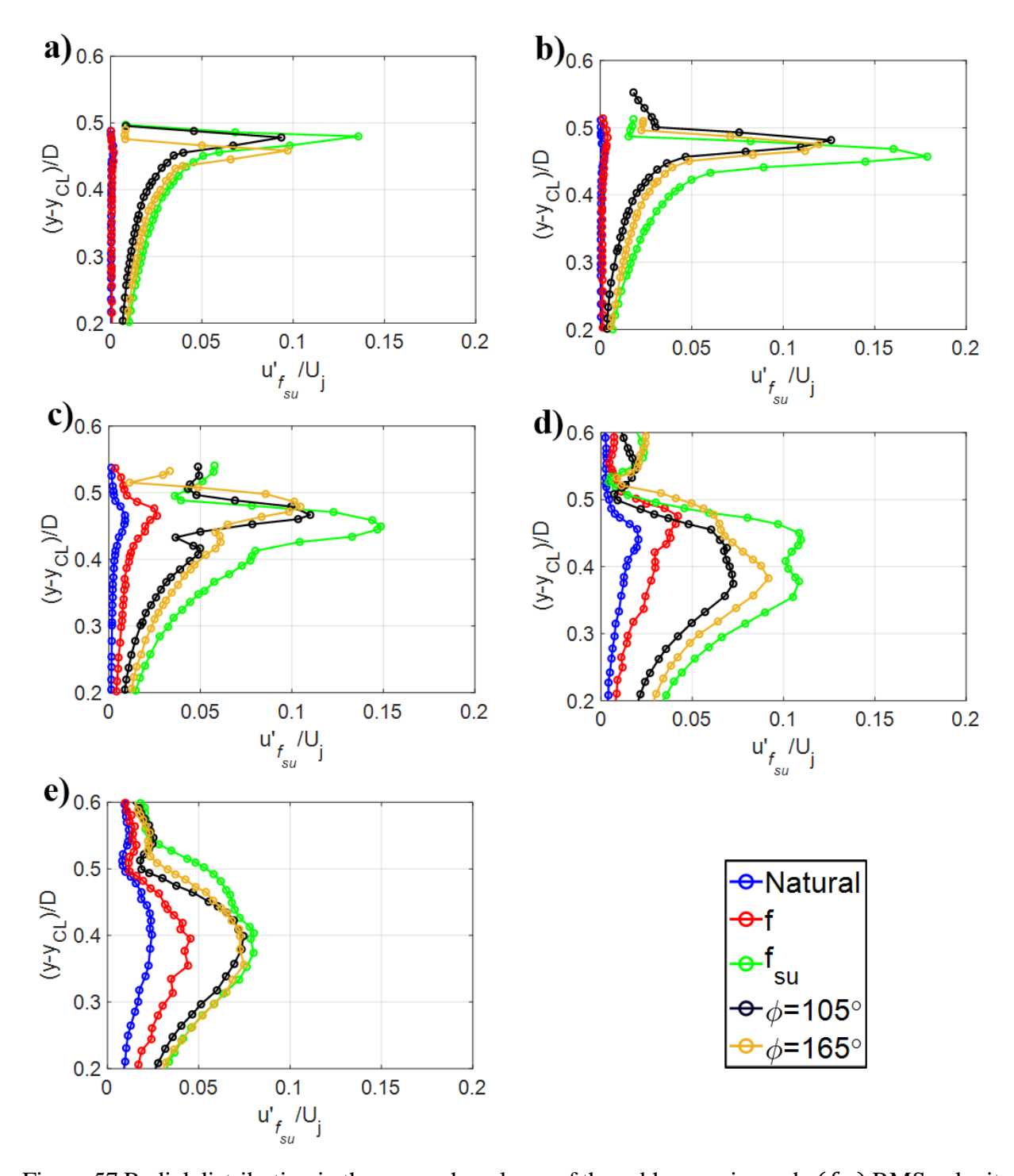


Figure 57 Radial distribution in the upper shear layer of the subharmonic mode (f_{su}) RMS velocity at different forcing condition (as indicated in the legend) and streamwise locations. a) x/D = 0.059, b) x/D = 0.118, c) x/D = 0.275, d) x/D = 0.5, and e) x/D = 1

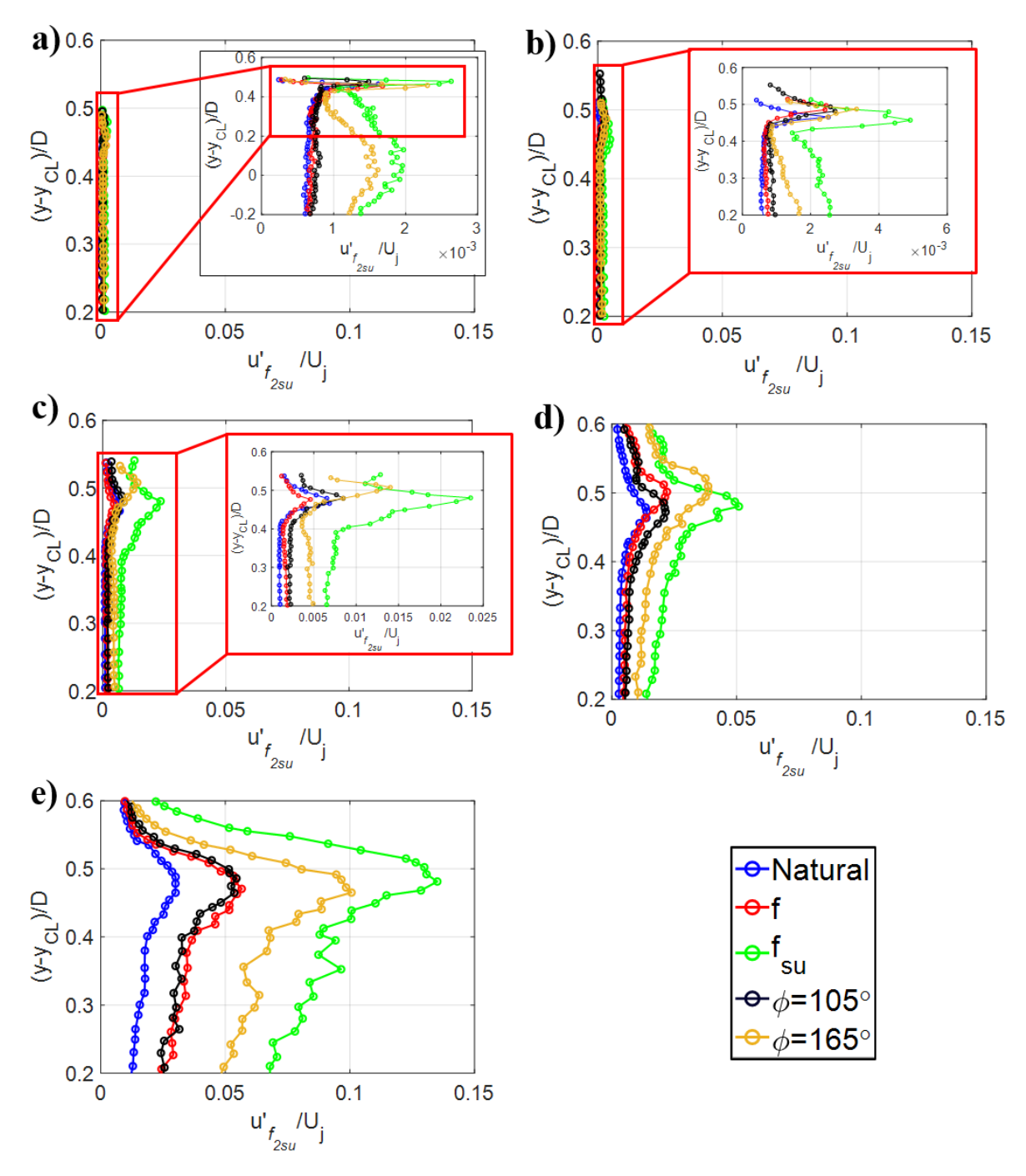


Figure 58 Radial distribution in the upper shear layer of the second subharmonic mode (f_{2su}) RMS velocity at different forcing condition (as indicated in the legend) and streamwise locations. a) x/D = 0.059, b) x/D = 0.118, c) x/D = 0.275, d) x/D = 0.5, and e) x/D = 1

4.2.2 Streamwise development of modal energy in the shear layer

Figure 59 depicts the spectral progression of the shear layer in the streamwise direction at different forcing conditions. Each plot corresponds to a different forcing mode (including the natural jet). Within a given plot, results at every streamwise location are plotted in a different color and shifted by one order of magnitude relative to one another to make all spectra visible. The fundamental frequency, the subharmonic frequency and the second subharmonic frequency are indicated with the red, green and blue vertical dashed lines respectively. Considering Figure 59a, which presents the spectra for the natural jet, at x/D = 0 (blue line), the spectrum shows a peak around $St_D = 2.54$ (1000 Hz), which is considered as the fundamental mode of the shear layer. Farther downstream, the fundamental mode peak weakens and at x/D = 0.433 (yellow line) the spectra show a new peak at the subharmonic frequency. Additional increase in x leads to the development of another peak at x/D = 0.748 (purple line) at the second subharmonic frequency. All peaks in the natural spectra are broad, and the peaks at the subharmonic and second subharmonic frequencies are not particularly prominent. The low-frequency peak at $St_D=0.45$, which is only seen at the most upstream locations but decays with downstream distance is believed to be part of the facility background fluctuation, as discussed in CHAPTER 2. This peak is not considered further in this work.

The fundamental forcing case (Figure 59b) shows a sharp peak at the fundamental frequency in the upstream spectra, as expected. The general evolution of the spectra with downstream distance is similar to the natural jet, but now the subharmonic and second subharmonic peaks start to develop earlier and are more pronounced/narrower than for the natural jet. This is consistent with the expectation that forcing organizes the vortex development and hastens its development.

The spectra for the subharmonic forcing case (Figure 59c) show a sharp peak at the subharmonic frequency throughout the measurement domain. A peak at the second subharmonic frequency is also seen and it is more prominent and well defined than for the two cases considered earlier. In fact, for the first time, the peak in the subharmonic frequency is observed across the entire domain of measurement and it can be tracked all the way to x/D = 0 (blue line), where a spectrum "blip" is seen. No special fundamental-mode peak is observed in the upstream spectra, but farther downstream, sharp peaks can be found. These late development, or redevelopment of the fundamental mode when other lower-frequency modes are growing are not an indication of mode amplification but rather a regrowth of the mode as a higher harmonic of the lower-frequency mode [7]. In other words, when a lower frequency mode oscillates in a non-pure harmonic mode as it grows (e.g. due to non-linear growth), this gives rise to higher harmonics.

The bi-modal forcing spectra (Figure 59d and Figure 59e) show two sharp peaks at the fundamental and the subharmonic modes, consistent with the presence of the two frequencies in the forcing scheme. The bi-modal forcing at $\phi = 105^{\circ}$ shows different development for the second subharmonic from that at $\phi = 165^{\circ}$. At $\phi = 105^{\circ}$ the second subharmonic mode starts to develop at x/D = 0.433 (yellow line), while at $\phi = 165^{\circ}$ it seems to start to develop at x/D = 0.236 (black line). Significantly, as in the case of subharmonic forcing, at $\phi = 165^{\circ}$ the second subharmonic peak can also be seen as early as x/D = 0 (blue line). As discussed earlier, the presence of the second subharmonic early in the shear layer development is believed to distinguish the jet response to the subharmonic forcing and bi-modal forcing at $\phi = 165^{\circ}$ from the other cases. This presence is likely due to a feedback mechanism since the second subharmonic frequency is not imposed on the jet. In Section 4.2.1, one possible physical mechanism for feedback was discussed in relation to interaction of the double-paired symmetric vortex structure with the stagnation zone of the

impingement plate. Other possible feedback mechanisms include direct acoustic radiation from the paired vortex structure as well as interaction of the vortex structure with the impingement wall in the wall-jet zone. Such interaction leads to vortex ejection and significant disturbance that maybe fed acoustically and/or hydrodynamically to the jet exit.

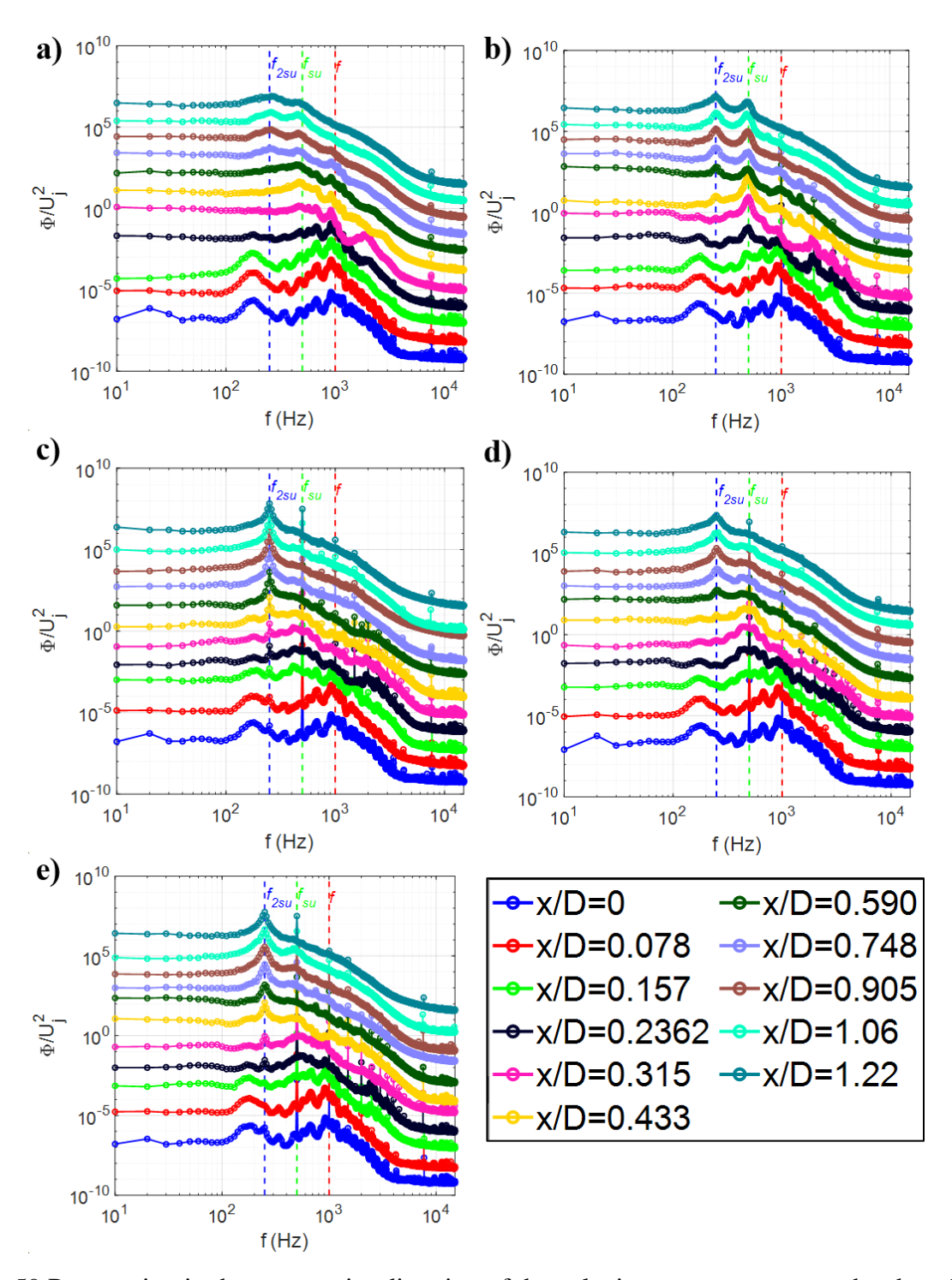


Figure 59 Progression in the streamwise direction of the velocity power spectra on the shear layer center at different forcing conditions. a) Natural jet, b) fundamental forcing, c) subharmonic forcing, d) bi-modal forcing $\phi = 105^\circ$, and e) bi-modal forcing $\phi = 165^\circ$. Spectra are shifted relative to one another to make the spectra progression visible

More detailed streamwise evolution of the different modes under different forcing conditions is examined by plotting the power spectrum magnitude at the modes' frequencies versus x/D. Figure 60 (linear scale) and Figure 61 (logarithmic scale) depicts this modal energy progression of the fundamental, the subharmonic and the second subharmonic mode in the streamwise direction. The figure is organized as in Figure 59, where each subplot corresponds to a given forcing condition. The natural jet results (Figure 60a) show the typical progression of instability. The fundamental mode is the first to grow, reaching a peak (i.e. saturating). As the fundamental mode saturates, the growth rate of the subharmonic mode steepens and the mode grows significantly stronger than the fundamental mode before peaking. With the saturation of the subharmonic, the second subharmonic starts to grow rapidly until it also reaches a peak. As the subharmonic grows, the fundamental mode experiences regrowth, which as discussed earlier, is a manifestation of the subharmonic wave form becoming non-pure harmonic; (i.e. the fundamental is growing as a harmonic of the subharmonic). Similarly, as the second subharmonic grows, the subharmonic regrows as its harmonic.

The fundamental forcing case leads to the same modal energy evolution as the natural jet, but the modal energy is significantly larger than that of the natural jet (compare Figure 60a and Figure 60b). On the other hand, the subharmonic and the bi-modal forcing cases lead to a significantly different development, with an initial dominance of the subharmonic instead of the fundamental mode. The accelerated development of the subharmonic for these cases is further emphasized by the subharmonic reaching its peak at $x/D \approx 0.23$, in comparison to $x/D \approx 0.5$ for the natural, and fundamental forcing cases.

In Figure 60c through Figure 60d, the fundamental mode, while having negligible energy compared to the subharmonic, is seen to grow simultaneously with the subharmonic early in the

development. This growth is not an inherent modal growth, but rather as a harmonic of the subharmonic. The energy of the fundamental mode is substantially larger for the bi-modal schemes compared to subharmonic forcing. This is expected given that the forcing energy is split equally between the fundamental and subharmonic modes in bi-modal forcing, while no forcing energy goes into the fundamental mode for the subharmonic forcing case. What is particularly surprising though is that in the bi-modal forcing, despite forcing the two frequencies at the same level, the initial energy of the fundamental mode is found to be less than one quarter of the subharmonic mode (this can be seen from the inset in Figure 60d and Figure 60e). This means that the actual *AR* within the shear layer is approximately 0.4 rather than unity as enforced by the excitation sound field. The reason for this difference is not known but one possibility is that feedback from the first vortex pairing [8], [50], which is enhanced significantly under bi-modal forcing, can add more energy to the subharmonic mode at the jet exit. This possibility can be particularly true because, as discussed above, the subharmonic mode saturates very close to the jet exit with bi-modal forcing (Figure 60d and Figure 60e).

Another unexpected outcome is that the streamwise modal evolution of the fundamental and the subharmonic modes does not present any evidence of subharmonic resonance. Resonance is characterized by the initial growth of the fundamental mode only, and when the fundamental mode saturates, the subharmonic mode exhibits significant growth enhancement leading to the subharmonic mode dominating over the fundamental mode. What is observed in Figure 60d and Figure 60e is immediate subharmonic growth with simultaneous growth of a much weaker fundamental mode. Thus, while the initial intent of the bi-modal forcing scheme is to cause subharmonic resonance between the fundamental and subharmonic modes, there is no evidence that this resonance did materialize. It is important to know that, despite not creating resonance

between the fundamental and subharmonic, the bi-modal scheme is able to enhance vortex pairing with the bi-modal phase having an important influence on the scheme's ability to do so, as already demonstrated.

In spite of the absence of subharmonic resonance between the fundamental and the subharmonic in bi-modal forcing, for the cases involving subharmonic forcing frequency, an apparent resonance seems to take place between the subharmonic and the second subharmonic modes. Examining the subharmonic forcing in Figure 60c, as the subharmonic mode reaches saturation, the second subharmonic mode starts to exhibit slight growth. Then, the subharmonic mode starts to drop followed by a significant increase in the second subharmonic growth rate. A similar behavior is seen for bi-modal forcing at $\phi = 165^{\circ}$ (Figure 60e) with the second subharmonic growth rate increasing while the subharmonic mode saturates. The enhancement of the growth rate of the second subharmonic is recognized from the upward curvature of the modal energy growth curve in the semi-log plots, indicating amplification beyond linear growth. For the subharmonic and $\phi = 165^{\circ}$ bi-modal forcing case, the upward curvature is evident for the second subharmonic once the subharmonic saturates. In contrast, for the bi-modal case at $\phi = 105^{\circ}$, no such upward curvature (i.e. enhance growth) is evident for the second subharmonic.

The distinction in the behavior of the second subharmonic mode between the subharmonic and $\phi = 165^{\circ}$ bi-modal forcing cases, on one hand, and the rest of the cases, on the other, is hypothesized to be related to the initial amplitude of the second subharmonic at the jet exit. As discussed previously in connection with the modal energy radial profiles (Figure 58), and spectra (Figure 59), the former cases exhibit substantially larger initial energy of the second subharmonic mode. This extra energy is assumed to relate to a feedback mechanism since the second subharmonic frequency is not included in any of the forcing schemes. The results in Figure 60c

and Figure 60e, show that this in turn could lead to subharmonic resonance that enhances the development of the second subharmonic. This enhancement is consistent with the strong promotion of double pairing events in the subharmonic and $\phi = 165^{\circ}$ bi-modal forcing cases, as seen from the flow visualization analysis.

The modal energy streamwise development can also be linked to vortex development. More specifically, the x location of the saturation of the initially growing mode defines the location of the initial vortex rollup [50]. Based on this, the fundamental mode is the initially growing mode for the natural jet and the fundamental forcing case. While the subharmonic mode is the initially growing mode for the subharmonic forcing and the bi-modal forcing cases. Referring to Figure 60, the initial vortex roll-up location is identified at x/D = 0.16, 0.16, 0.24, 0.24, and 0.28 for the natural jet, the fundamental forcing case, the subharmonic forcing case, the bi-modal forcing case at $\phi = 105^{\circ}$, and the bi-modal forcing case at $\phi = 165^{\circ}$ respectively. These observations are consistent with the videos obtained from the flow visualization in teRMS of the initial vortex frequency at the upstream side of the images. Yet, the video images also show that cases involving the subharmonic tone in the forcing continue to roll-up for a short distance into the images. Thus, in the case of the subharmonic forcing, the vortex roll-up location based on the modal energy peak in the shear layer is a good indication of the start rather than the completion of the vortex roll-up. As discussed earlier, the far-field fluctuating induced velocity of the vortex structures is expected to be a better indicator of the overall vortex evolution than the fluctuating velocity in the shear layer. To this end, the streamwise evolution of the modal energy along the jet centerline is analyzed next.

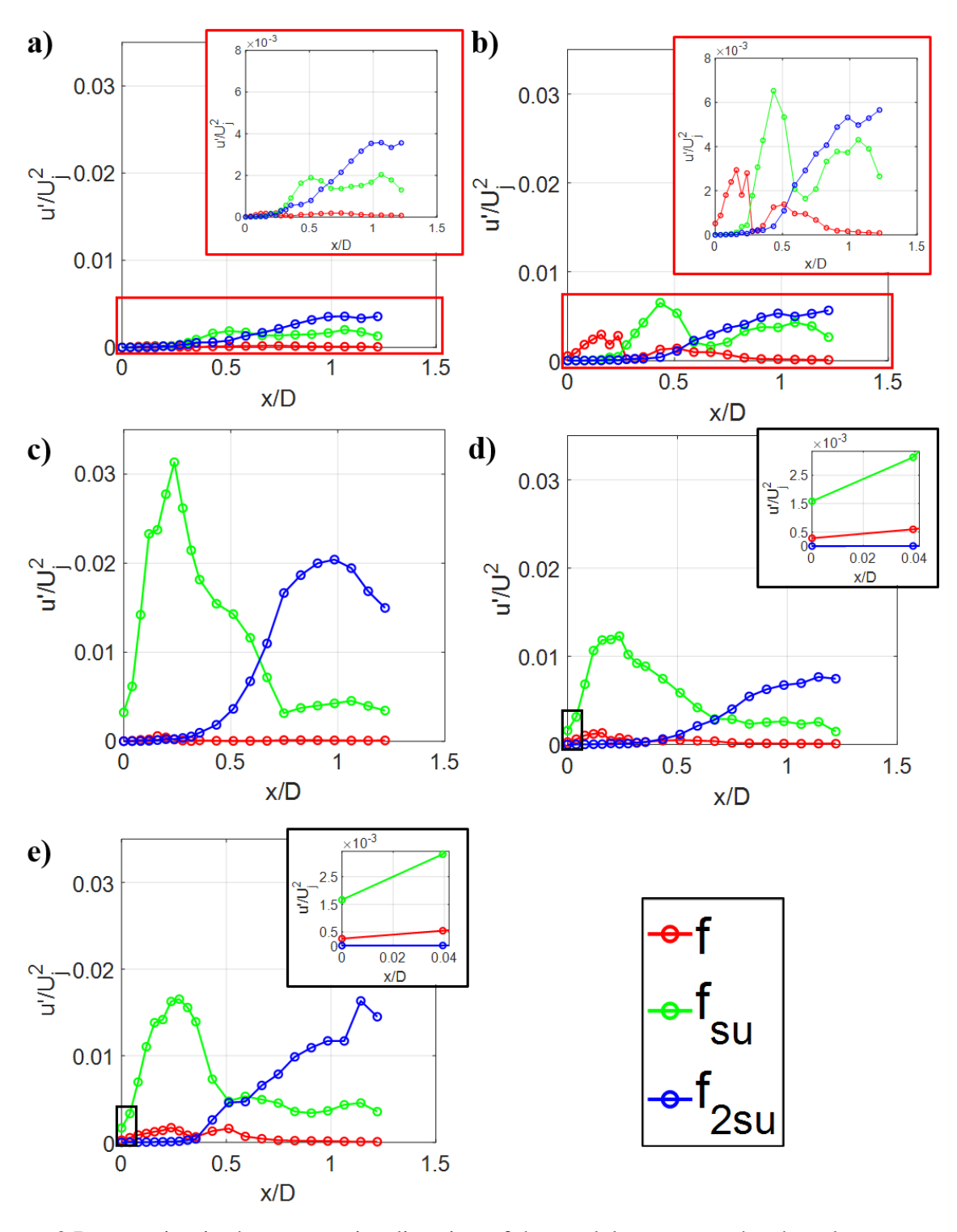


Figure 60 Progression in the streamwise direction of the modal energy on the shear layer center at different forcing conditions. a) Natural jet, b) fundamental forcing, c) subharmonic forcing, d) bi-modal forcing $\phi = 105^{\circ}$, and e) bi-modal forcing $\phi = 165^{\circ}$

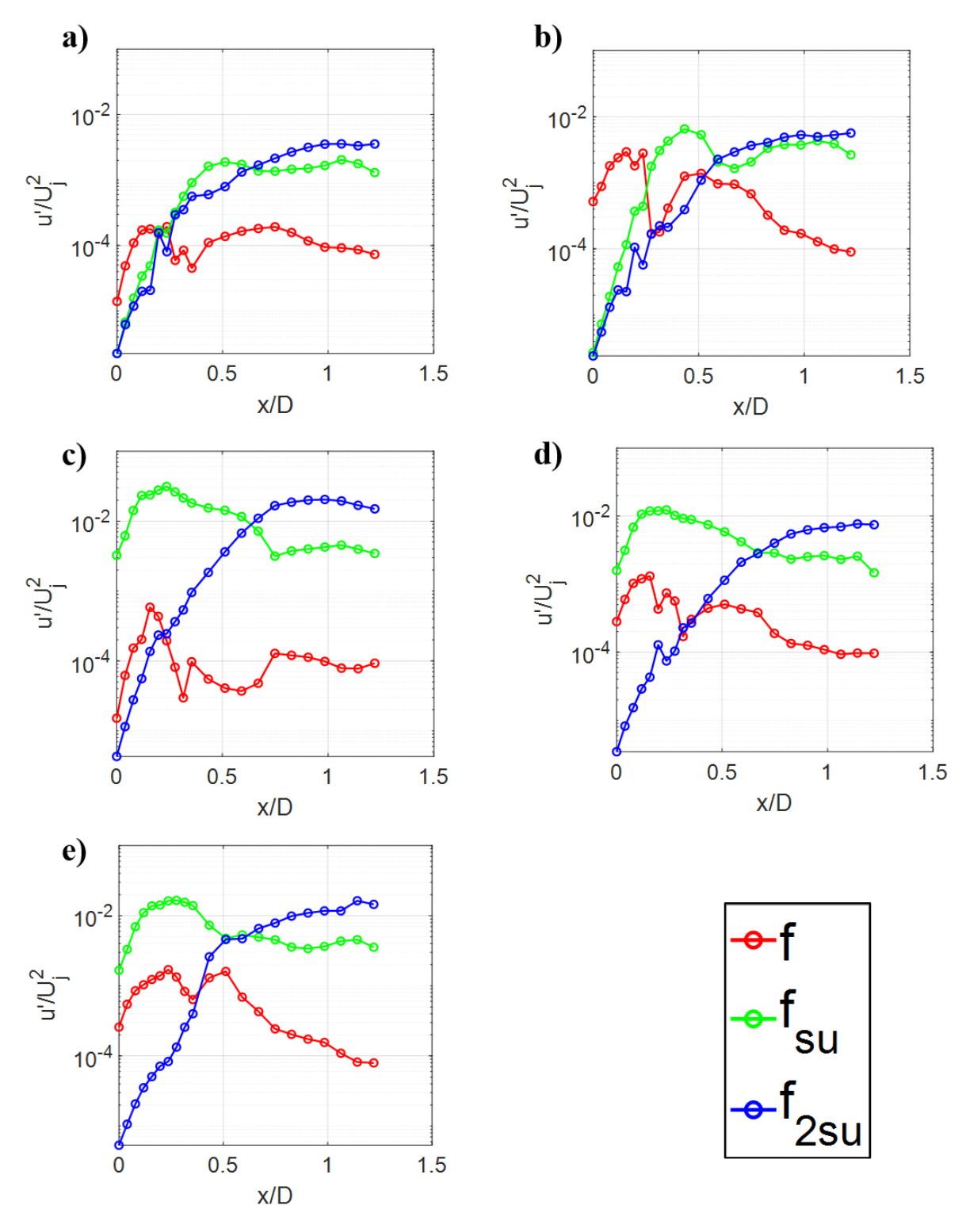


Figure 61 Semi-log progression of the streamwise direction modal energy on the shear layer center at different forcing conditions. a) Natural jet, b) fundamental forcing, c) subharmonic forcing, d) bi-modal forcing $\phi=105^\circ$, and e) bi-modal forcing $\phi=165^\circ$

The streamwise location at which subsequent vortex pairing happens after the initial roll-up is typically taken as the modal peak, or the saturation location, of the mode corresponding to the frequency of the paired vortex [10]. In this case the pairing location is defined as the location where the pairing vortices are aligned across the cross-stream direction [10]. As explained earlier the location of the modal saturation in the shear layer does not agree well with where vortex roll up is completed in the observations from the flow visualization. On the other hand, the jet centerline modal energy evolution in the streamwise direction, shown in Figure 62, provides a good agreement with the flow visualization observations. Inspection of Figure 61 shows that the first pairing, which forms the subharmonic vortex, is completed at $0.9 \le x/D \le 1.15$ for the natural jet, and $0.7 \le x/D \le 1.0$ for fundamental forcing case, where the subharmonic energy (green line) peaks (Figure 62a and Figure 62b). These pairing locations show consistency with those observed in the flow visualization. Subharmonic and bi-modal forcing show accelerated first pairing, where the peak in the subharmonic mode's energy is reached at an earlier streamwise location in the x/D range of 0.5-0.7 (Figure 62c thru Figure 62e).

When it comes to the second pairing, which occurs between two vortices at the subharmonic frequency to form a vortex at the second subharmonic frequency, Figure 62 shows that this pairing is not completed within the streamwise domain of the hot-wire measurements. Specifically, the modal energy of the second subharmonic mode (blue line) does not saturate before the end of the measurement domain. This is consistent with the flow visualization observations, where the second pairing is usually observed in the flow visualization downstream of the end of the hot-wire measurement domain.

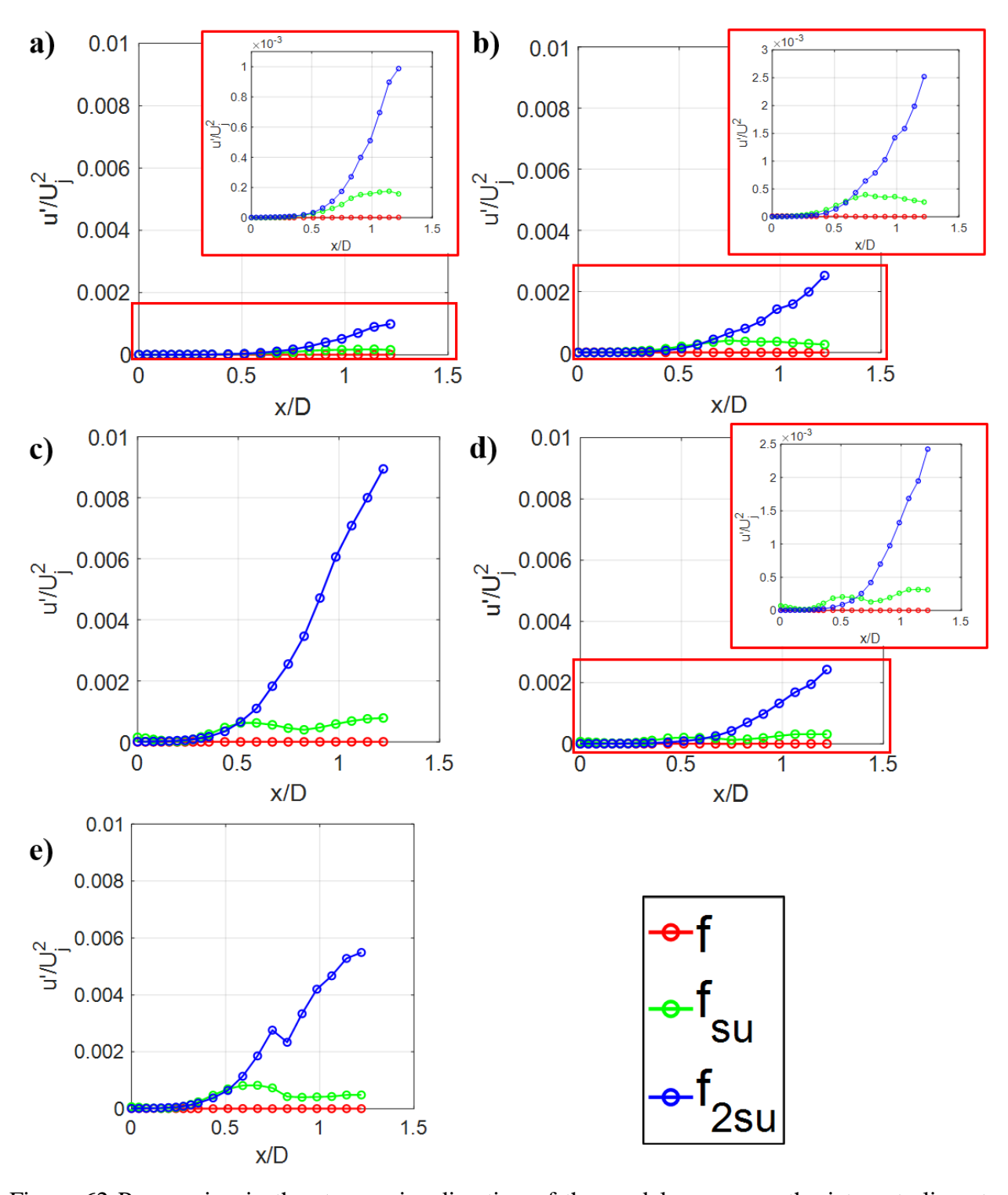


Figure 62 Progression in the streamwise direction of the modal energy on the jet centerline at different forcing conditions. a) Natural jet, b) fundamental forcing, c) subharmonic forcing, d) bi-modal forcing $\phi = 105^{\circ}$, and e) bi-modal forcing $\phi = 165^{\circ}$

4.3 Streamwise Development of Modal Coherence and Phase

4.3.1 <u>Modal coherence</u>

Coherence can be explained as the correlation between two signals at a given frequency independent of the signal strength. In a flow with broadband turbulence, the coherence between two signals generally decays with the distance between the two measurement locations. In the current work, the coherence is computed between the signals of the hot wire and one of the faceplate microphones (microphone #1) as the hot wire is traversed to different *x* locations on the shear layer center and the jet centerline. This is done for the main three modes (fundamental, subharmonic and second subharmonic) at different forcing conditions.

$$\Gamma_{xy}(f) = \frac{|\Phi_{xy}(f)|}{\sqrt{\Phi_{xx}\Phi_{zz}}} \tag{4.1}$$

Where, Φ_{xy} is the cross spectrum between the faceplate microphone (microphone 1) signal and the hot-wire signal, Φ_{xx} is the power spectra of the faceplate microphone, and Φ_{zz} is the power spectrum of the hot wire. Γ_{xy} varies between 0 and 1, where 0 represents no coherence between the two signals and 1 perfect coherence.

The coherence on the shear layer center for the natural case (Figure 63a) shows a monotonic decay in the streamwise direction for the fundamental mode (red line). This indicates a coherence loss due to disorganization and jitter in vortex formation and possibly the development of some small-scale turbulence. A similar overall trend is also seen for the subharmonic mode (green line), except in this case, the coherence does not decay to near zero but rather reaches a plateau downstream of x/D = 0.5. For the second subharmonic mode (blue line), a non-monotonic trend is observed with the coherence growing again as the location of the peak in the second subharmonic modal energy (seen in Figure 62a) is approached. The increased coherence with

increasing downstream distance is believed to be due to an acoustic feedback to the jet exit of fluctuation at f_{2su} . On the jet centerline (Figure 64a), similar trends are seen for the fundamental and second subharmonic modes as in the shear layer but the fundamental mode now exhibits local increases in the coherence at distances farther downstream. These local peaks can be interpreted as the higher harmonics of the subharmonic and the second subharmonic. For the subharmonic mode, the coherence on the jet centerline does not show the initial decay seen in the shear layer. Instead, the coherence grows initially and reaches an approximate plateau. The presence of this plateau for both the jet centerline and the shear layer is also interpreted to be related to the presence of some acoustic feedback from the first vortex pairing and beyond.

All forced jet cases are seen to maintain high coherence of the forced modes for an extended distance that is significantly larger than seen for the natural jet. As seen in Figure 63b and Figure 64b, the fundamental mode coherence for the fundamental forcing case stays close to unity up to x/D = 0.5 for both the shear layer and jet centerline profiles. Farther downstream (x/D > 0.5), the coherence decays monotonically on the shear layer center but exhibits regrowth near x/D = 0.75 on the jet centerline. The results are consistent with expectation, where forcing at the fundamental frequency organizes vortex formation at the fundamental frequency over a larger streamwise domain. However, eventually the coherence decays due to the loss of coherence between the flow structure and the external forcing. The regrowth of the fundamental mode coherence seen on the jet centerline is connected to the growth of the fundamental as a higher harmonic of the second subharmonic mode, which exhibits peak coherence at the same location of the fundamental coherence regrowth. It is also noted that overall, the coherence behavior in the shear layer for the fundamental forcing case is similar to the natural case except the coherence values are maintained higher and over larger distances when forcing the jet (compare Figure 63a

with Figure 63b). Particularly interesting is the rise of the coherence of the subharmonic and second subharmonic with the forcing in Figure 64b compared to Figure 64a. This is consistent with the promotion of double pairing when forcing the jet at the fundamental frequency relative to the natural jet.

When it comes to the forcing schemes involving the subharmonic frequency, Figure 63c through Figure 64e and Figure 64c through Figure 64e show that these schemes maintain subharmonic mode coherence close to unity until the end of the measurement domain. For these cases, the fundamental mode coherence is different depending on the presence of the fundamental frequency in the forcing scheme. For bi-modal forcing, the coherence is generally similar to that when forcing at the fundamental frequency only. In contrast, for subharmonic forcing alone, a much lower coherence (mostly around or below 0.5) is seen across the domain. This is not surprising given the absence of the fundamental frequency in the forcing mode.

A particularly interesting observation is that the second subharmonic mode exhibits high coherence for the entire measurement domain at the subharmonic forcing and the bi-modal forcing at $\phi = 165^{\circ}$ along the shear layer and the jet centerline (except for a short stretch of $0.03 \le x/D \le 0.2$ in the shear layer for bi-modal forcing at $\phi = 165^{\circ}$). As discussed previously, the second subharmonic mode is not an externally forced mode but has a relatively large initial fluctuation energy for these two cases compared to the others. Therefore, it was hypothesized that a feedback mechanism from the second vortex pairing and its interaction with the wall is responsible for these elevated levels. The high level of coherence at the second subharmonic frequency across the full domain of the measurements (more than half the distance to the impingement plate) provides additional supportive evidence of this idea. It is interesting to note that this high coherence level at f_{250} is not found for the case of bi-modal forcing at $\phi = 105^{\circ}$.

As seen in Figure 63c and Figure 64c, the coherence in this case is low on both the shear layer center and the jet centerline. This is consistent with the randomness and the asymmetry of the vortex development observed at this intermodal phase in flow visualization

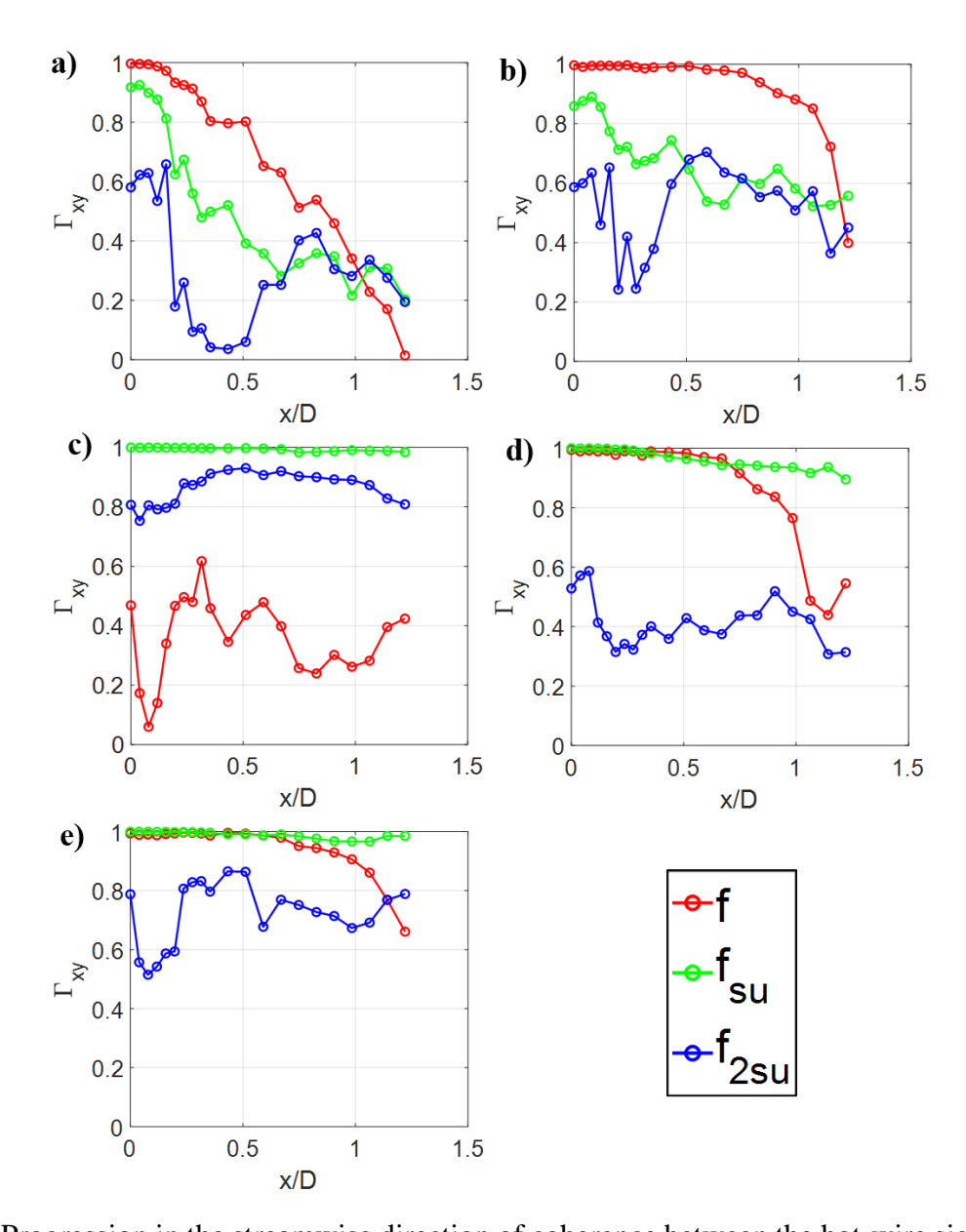


Figure 63 Progression in the streamwise direction of coherence between the hot-wire signal on the shear layer center and the signal from a faceplate microphone (Mic#1). a) Natural jet, b) fundamental forcing, c) subharmonic forcing, d) bi-modal forcing $\phi = 105^{\circ}$, and e) bi-modal forcing $\phi = 165^{\circ}$

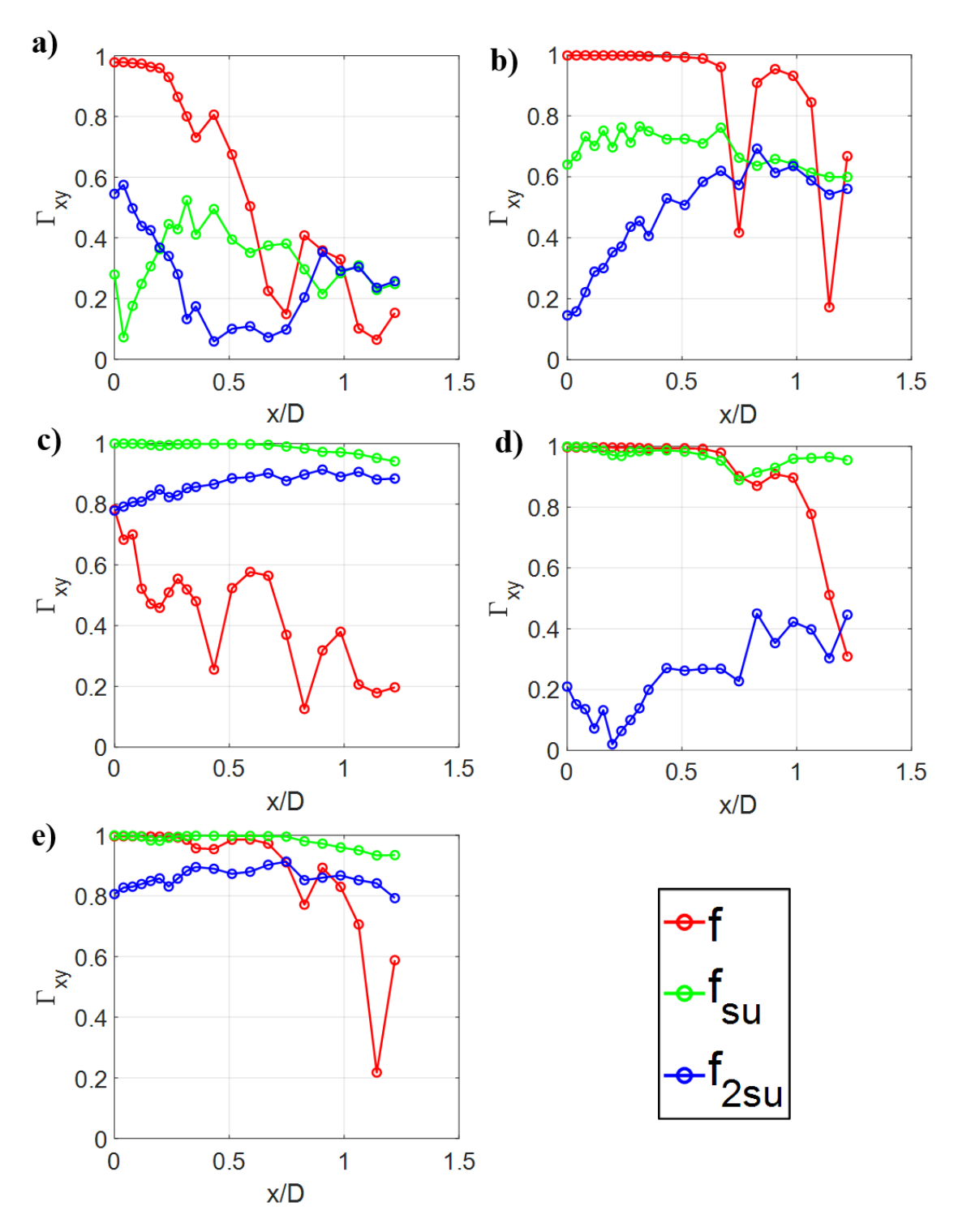


Figure 64 Progression in the streamwise direction of coherence between the hot-wire signal on the jet centerline and the signal from a faceplate microphone (Mic#1). a) Natural jet, b) fundamental forcing, c) subharmonic forcing, d) bi-modal forcing $\phi = 105^{\circ}$, and e) bi-modal forcing $\phi = 165^{\circ}$

4.3.2 Intermodal and modal phase

The intermodal phase between the subharmonic mode and the second subharmonic mode is used to further investigate possible intermodal resonance between these modes. To compute the intermodal phase, referred to here as ϕ_s to distinguish it from ϕ (the intermodal phase between the fundamental and the subharmonic), the time series from the hot wire is broken into 200 records of 3000 points each. Each record is Fourier transformed via the FFT, the phase values at f_{su} and f_{2su} are extracted and the intermodal phase is computed for the i^{th} record as:

$$\phi_s^{(i)} = \frac{2\psi_{2su}^{(i)} - \psi_{su}^{(i)}}{2}; i = 1, ..., N_r$$
(4.2)

Where, $\psi_{su}^{(i)}$ and $\psi_{2su}^{(i)}$ are the phase angles for the subharmonic and second subharmonic respectively and N_r is the number of records. The factor 2 in the numerator and denominator is the multiplicity factor between the two modes. For instance, if the two modes considered have frequencies that are related by a multiple of 5, then the factor 2 would be replaced by 5 in

(4.2). The computed $\phi_s^{(i)}$ value for each record is forced into the interval $0^{\circ} \le \phi_s^{(i)} < 180^{\circ}$ due to the 180° phase periodicity. The overall intermodal phase value ϕ_s is then computed as an average over all records; i.e.

$$\phi_{s} = \frac{\sum_{i=1}^{N_{r}} \phi_{s}^{(i)}}{N_{r}} \tag{4.3}$$

It is found that sufficient spectral resolution is necessary for the phase values to converge and not be influenced by neighboring frequencies or spectral leakage. To this end, the frequency resolution of the analysis is set to 10 Hz with the frequencies of the subharmonic and second subharmonic coinciding exactly with discrete frequency bins of the FFT.

The intermodal phase between the subharmonic and the second subharmonic mode is calculated at the jet centerline for different streamwise locations at all forcing conditions as shown

in Figure 65. Previous studies showed that the best location to investigate the phase is on the high-speed side of the shear layer, where the phase asymptotes to a uniform value, hence avoiding the phase oscillation within the shear layer [7]. They also showed that the resonance between the fundamental mode and the subharmonic mode resulted in an intermodal phase change of 90° at the location of the resonance.

Figure 65a and Figure 65b show that no intermodal phase transitions is observed for the natural jet or when forcing at the fundamental frequency. This is indicative of the absence of resonance between the subharmonic and second subharmonic in these cases. On the other hand, for all cases involving external subharmonic forcing frequency (i.e. subharmonic and bi-modal forcing), phase transitions are indeed observed. The bi-modal forcing at $\phi = 165^{\circ}$ not only shows a 90° phase transition but the transition is sharp (Figure 65e). In comparison, the phase transition for subharmonic forcing and the bi-modal forcing at $\phi = 105^{\circ}$ show a significantly more gradual transition (Figure 65c and Figure 65d). The transition is approximately 90° for subharmonic forcing and about 37° for bi-modal forcing at $\phi = 105^{\circ}$. The sharp transition is an indication of a highly repeatable resonance location, which is consistent with the uniqueness of the case of $\phi =$ 165° bi-modal forcing in providing the most consistent and organized double-paired symmetric structure from cycle to cycle (as seen from the flow visualization analysis). The gradual transition of approximately 90° in the case of subharmonic forcing is indicative of a jitter in the location of resonance and less organization of the double-paired symmetric structure. Also, the phase transition value of less than 90° (specifically 79°) is reflective of a small but non-vanishing fraction of the time when resonance is not taking place. This is also seen in the video images for the subharmonic forcing case, where the double-paired vortex structure is not present all the time. When it comes to bi-modal forcing at $\phi = 105^{\circ}$, the phase transition is both gradual and

significantly less than 90°. This is consistent with the findings from the flow visualization (CHAPTER 3) in this case that the double-paired symmetric structure only occurs for a small fraction of the time. Thus, the observed phase transition is reflective of partial occurrence of resonance that, like the subharmonic forcing case, occurs at a location that jitters in space. Of course, as already observed, in this case also, the jet is the least organized of all bi-modal cases, exhibiting significant asymmetry.

Downstream of the phase transition, the intermodal phase becomes approximately 45° for the cases of subharmonic and bi-modal forcing at $\phi=165^\circ$. For bi-modal forcing at $\phi=105^\circ$, the intermodal phase changes to 63°. The significance of these values can be appreciated by noting that if the intermodal phase varies completely random between records, then the average ϕ_s will equal to 90° (midway of the 0° – 180° interval). Inspection of the intermodal phase for the natural jet in Figure 65a yields $\phi_s=85.54^\circ$, which is very close the value of completely random variation in ϕ_s . With forcing at the fundamental frequency, $\phi_s=71.5^\circ$, indicating perhaps some preference/organization of the intermodal phase. The intermodal phase values become further removed from the 90° value with subharmonic and bi-modal forcing as seen above with the cases dominated by double-paired symmetric vortex structures settling on an intermodal phase value around 45°.

The connection between the intermodal phase behavior and the structure organization can be clarified further using a histogram of $\phi_s^{(i)}$ values, as shown in Figure 66 for all forcing conditions. The histogram is obtained at the most downstream point in the hot-wire measurement domain (x/D=1.22). The natural case (blue line) exhibits a relatively flat histogram with a slight broad peak near 45°. The slight peak results in ϕ_s being slightly below 90°, as discussed above, but the histogram clearly depicts practically no structure organization between the subharmonic

and second subharmonic modes for the natural jet. The fundamental forcing case (red line) shows a higher histogram peak than the natural jet at $\phi_s^{(i)} \approx 30^\circ$, which shows a relatively better organization for developing the double-paired vortex structure, in alignment with the flow visualization findings.

The intermodal phase organization is enhanced further with bi-modal forcing at $\phi=105^\circ$ with the histogram (shown in black) exhibiting an even stronger peak at $\phi_s^{(i)}\approx 45^\circ$. Ultimately, as expected, the best intermodal phase organization is seen for the cases of subharmonic forcing and bi-modal forcing at $\phi=165^\circ$ (green and magenta lines respectively). For these two cases, the intermodal phase histogram becomes highly focused near 45° with large excursion from this value being practically non-existent. The narrow-peak of the histogram indicates the most organization between the subharmonic and the second subharmonic modes for all cases. While the histogram seems to indicate that the subharmonic forcing and bi-modal forcing at $\phi=165^\circ$ cases are similarly organized, it should be noted that this is downstream of the 90° phase transition. The better organization of the bi-modal $\phi=165^\circ$ case is evident in the much sharper phase transition (i.e. resonance location) in Figure 65.

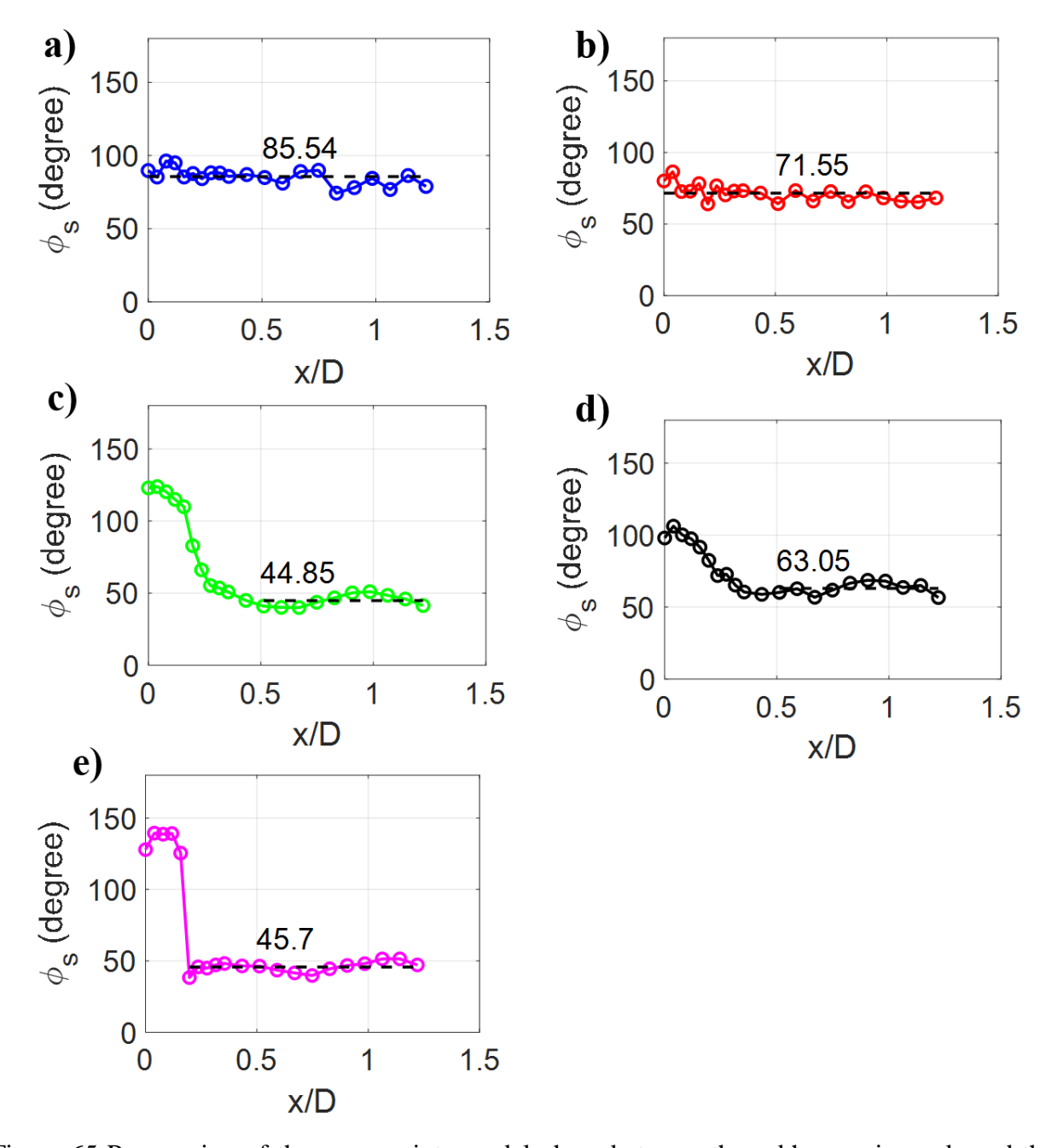


Figure 65 Progression of the average intermodal phase between the subharmonic mode and the second subharmonic mode on the jet centerline in the streamwise direction at different forcing conditions. a) Natural jet, b) fundamental forcing, c) subharmonic forcing, d) bimodal forcing at $\phi = 105^{\circ}$, and e) bi-modal forcing at $\phi = 165^{\circ}$

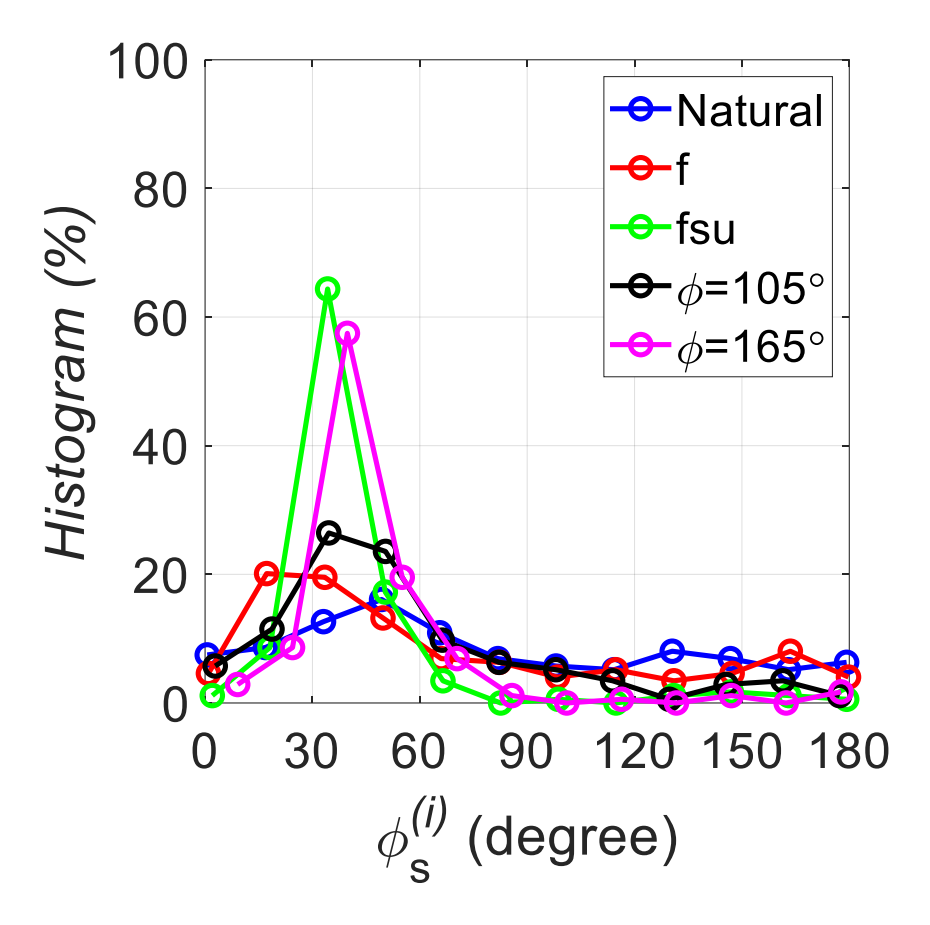


Figure 66 Histogram of the intermodal phase between the subharmonic and the second subharmonic obtained on the jet centerline and x/D = 1.22

Another interesting observation is to compare the streamwise evolution of ϕ_s to the modal energy growth of the subharmonic and second subharmonic modes in the shear layers for the two cases exhibiting evidence of resonance; i.e. the subharmonic and the bi-modal $\phi=165^{\circ}$ cases. These plots are shown in Figure 67 with the intermodal phase shown on the top and the modal energy on the bottom of the figure. A broken black line marks the half-way point of phase transition and extends to the modal energy plot. As seen from the figure the phase transitions coincide well with the saturation of the subharmonic mode and the start of enhanced growth of the second subharmonic, confirming further the idea of occurrence of resonance between these two modes.

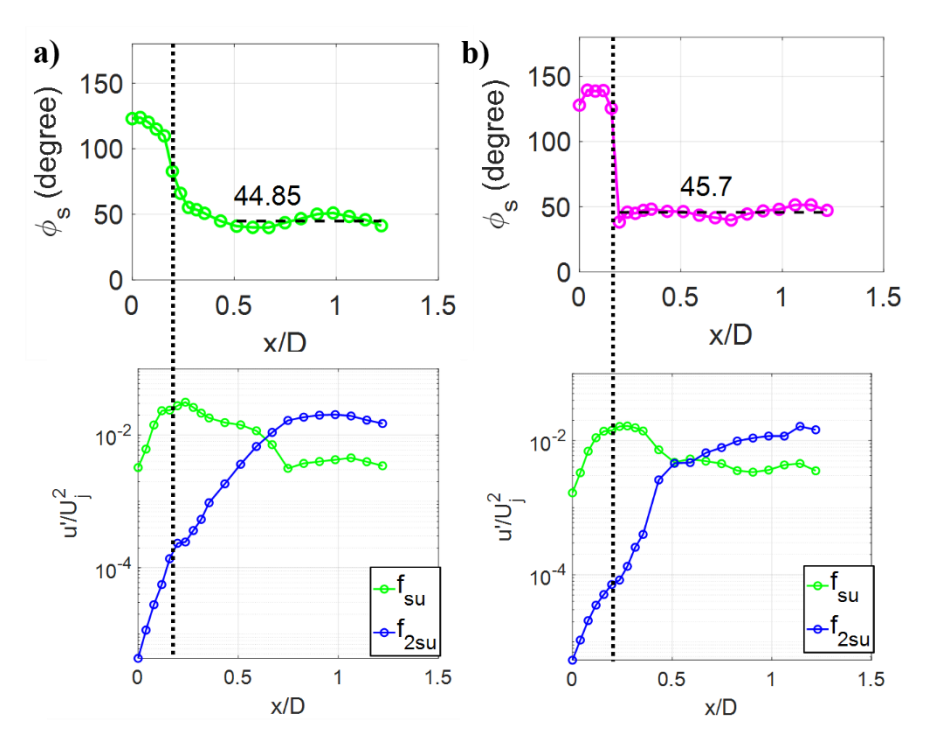


Figure 67 Streamwise progression of the intermodal phase between the subharmonic and the second subharmonic modes on the jet centerline (top), compared to the streamwise modal energy progression on the shear layer center for these two modes (bottom) and subharmonic forcing (left) and bi-modal $\phi = 165^{\circ}$ forcing (right)

Finally, the phase velocities for the two cases exhibiting resonant behavior are computed. The convection velocity is calculated from the slope of the plot of the cross-spectrum phase angle $(\angle \Phi_{xy})$ in radian) versus the streamwise location (m); where the cross-spectrum is calculated between the hot-wire measurement at the jet centerline and microphone #1 in the faceplate. The results are shown in Figure 68. As seen in the figure, the phase variation is initially non-linear, but it becomes linear at $x/D \approx 0.5$. When the curve becomes linear, that indicates a constant convection velocity until the end of the domain (Figure 68). The linear behavior indicates constant convection velocity that can be obtained for a given mode from the slope of the phase line (m_p) in radians/m as follows: $u_c = \frac{2\pi}{m_p} f$, where, f is the frequency of the mode. The line fits to the linear portion of the phase plot to obtain the slope m_p are shown in Figure 68.

The computed convection velocity values are shown in Table 4 for the subharmonic and second subharmonic modes. The values depict a similar convection velocity for the two modes for the bimodal forcing at $\phi=165^\circ$ (approximately 5% deviation from each other). The discrepancy in convection velocity between the two modes for subharmonic forcing show a higher deviation (approximately 11%). It is important to note that when two modes are in resonance, their convection velocity is expected to be the same. The small deviation between the two values for the case of bi-modal forcing at $\phi=165^\circ$ is probably a reflection of the rare times that resonance does not occur. The larger deviation for subharmonic forcing is consistent with the lesser organization of resonance in this case than in the $\phi=165^\circ$ bi-modal case.

It is notable that when normalized by U_j , the convection velocity values are appreciably larger than that found in a nozzle jet. This is due to the jet flow acceleration downstream of the exit because of the vena-contracta effect. If the vena-contracta velocity (U_{vc}) is used to normalize the convection velocity, the values are smaller and comparable to the values reported in the literature [7] (Table 4).

Table 4 Convection velocity of the subharmonic and harmonic modes, normalized by the mean jet velocity and the vena-contracta velocity

Modes	u_c/U_j		u_c/U_{vc}	
Forcing Condition	f_{su}	f_{2su}	f_{su}	f_{2su}
Subharmonic forcing	0.935	0.842	0.703	0.633
Bi-modal forcing $(\phi = 165^{\circ})$	0.822	0.865	0.618	0.65

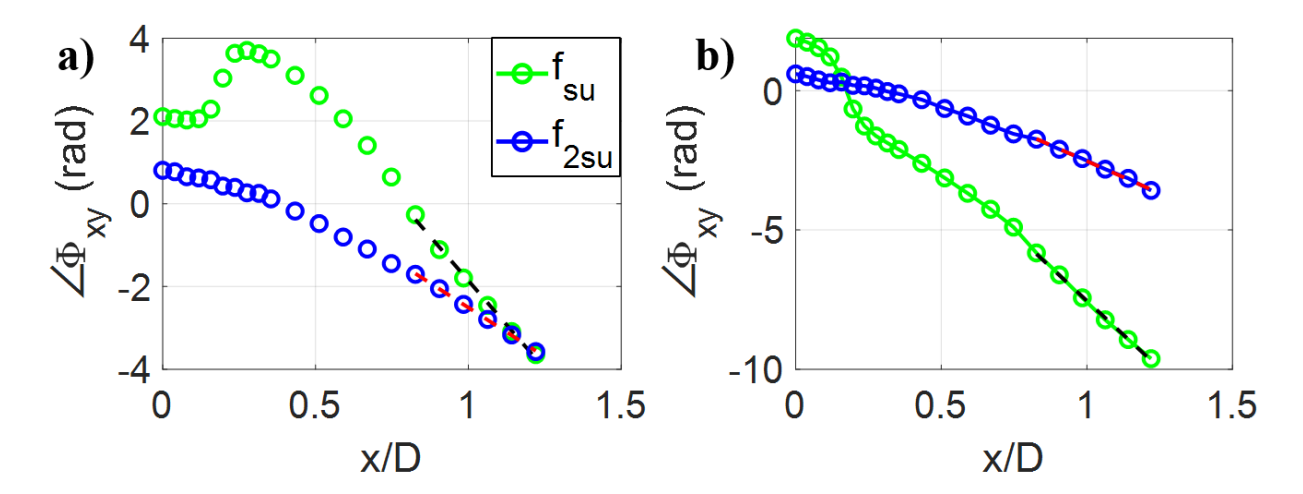


Figure 68 Phase progression in the streamwise direction. a) Subharmonic forcing, b) bi-modal forcing at $\phi=165^\circ$

CHAPTER 5. PRELIMINARY HEAT TRANSFER EXPERIMENTS

Preliminary heat transfer measurements were conducted prior to the experiments utilizing the high-speed flow visualization and hot-wire measurements reported in Chapters 2 through 4. Subsequent to the latter experiments, there was insufficient time to properly conduct the heat transfer measurements under identical conditions. The early heat transfer experiments were based on measuring the excitation sound field at x/D = 0.75 on the centerline of the jet, which is different from the results presented up to this point, where the sound field is characterized at the jet lip. Therefore, it is not expected that the intermodal phase between the early and the main experiments will be the same. Other differences between the two experiments include the forcing level, which is significantly higher at 1%, compared to 0.3% for the main experiments.

Notwithstanding the noted differences, it is deemed worthy to document the early heat transfer experiments and their main results here. There are some qualitative connections that can be drawn between the vortex structure under bi-modal forcing in the early and the main experiments. Specifically, in the early experiments, the largest most consistent vortex structure is identified at $\phi=120^\circ$. This is taken to be the equivalent of $\phi=165^\circ$ in the main data set. Similarly, $\phi=45^\circ$ in the early set produce vortex behavior that exhibits the most intermittent switching between symmetric and asymmetric vortex structures. This is taken to be the equivalent of $\phi=90^\circ$ or 105° in the data reported earlier. It should also be noted that at the time of the early experiments, the capability to conduct high-speed flow visualization did not exist in the present experimental facility. Therefore, the characterization of the vortex structure in the early experiments is done based on phase-averaging relative to the forcing cycle. The early experiments also did not include pure harmonic forcing.

In the following, details of the experimental setup and technique used for measuring the heat transfer in the early experiments are described followed by a summary of the key findings from these experiments.

5.1 Experimental Techniques

The heat transfer impingement plate, which is depicted in Figure 69 and Figure 70, is a 25 µm-thick stainless-steel sheet that is tensioned on two hollow round copper bus bars. The sheet's tension is maintained by three tension springs connected to each side of the sheet via custom-designed clamping plates. The heated area of the impingement plate is 203.2 mm ×152.4 mm (16D × 12D). The plate is heated by applying a DC electrical voltage across the plate. This provides a constant-heat-flux boundary condition for the convective heat transfer coefficient measurements.

Where, q is the local convective heat flux to the jet flow, Q is the total electrical power dissipated in the plate, A is the heated surface area of the plate, and $\Delta T = (T_s - T_{amb})$ is the difference between the surface and the ambient temperature. The heat dissipation via natural convection to the back (non-impingement) side of the plate, via conduction in the plane of the plate, and via radiation are neglected in (5.1).

To measure the convective heat transfer coefficient h from the heated plate to the impinging jet, conservation of energy is applied to the plate at steady state:

$$q = \frac{Q}{A} = h\Delta T \tag{5.1}$$

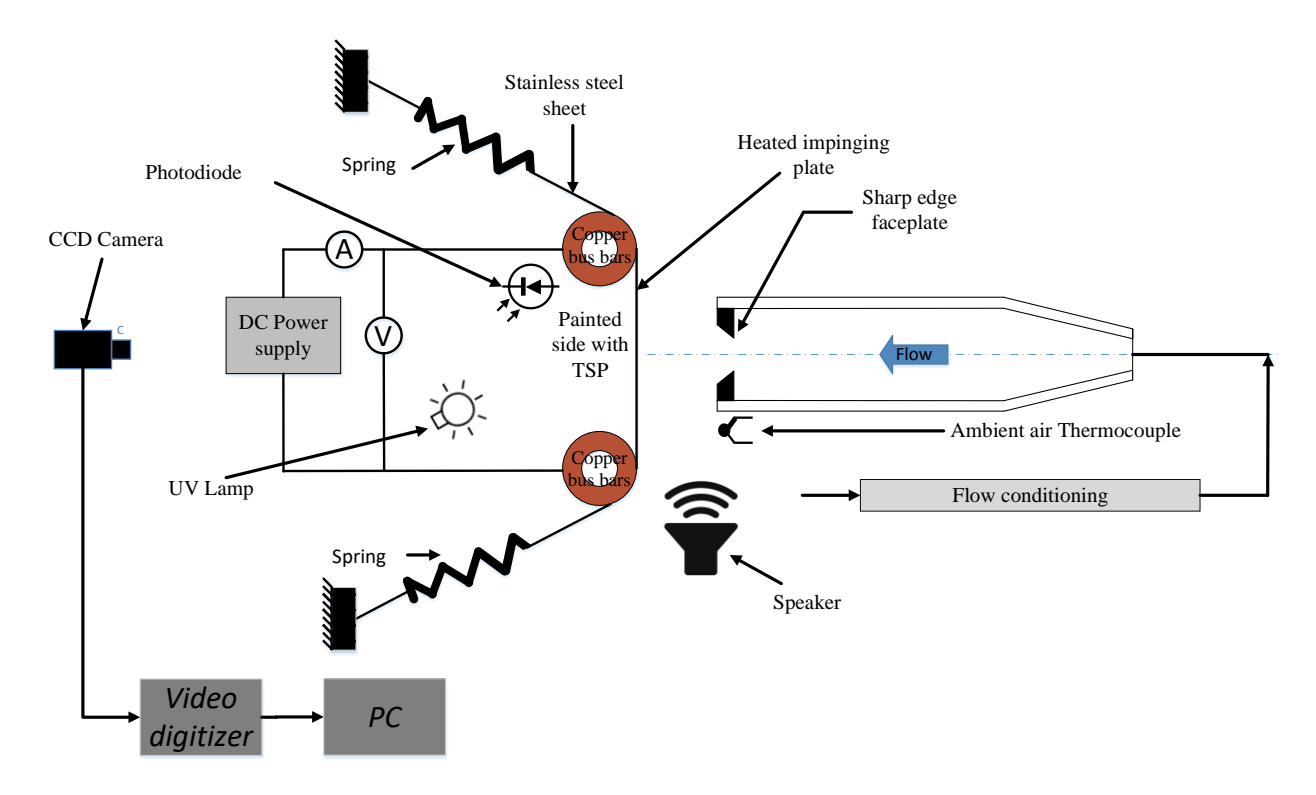


Figure 69 Schematic of the heat transfer measurement setup

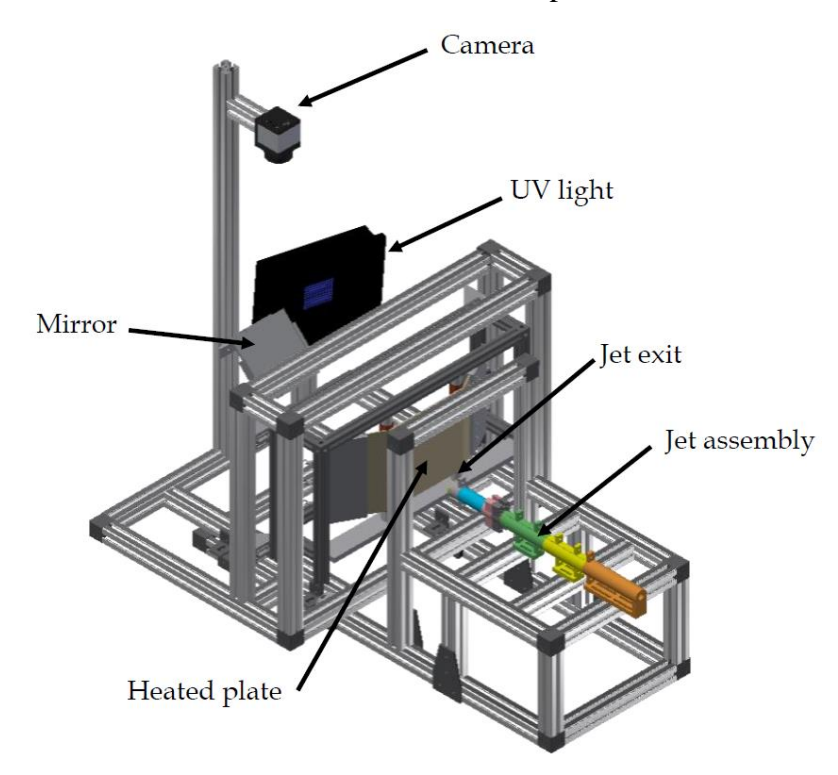


Figure 70 3D drawing for the heat transfer setup. The heated plate frame slides on the jet frame allowing different H/D

Estimates of the uncertainty due to natural convection depends on the radial distance from the jet centerline due to T_s increasing in the r direction from typically $32^{\circ}C$ at r=0, to $60^{\circ}C$ at r=4D. Based on a typical temperature distribution an estimate of the error due to natural convection (computed based on [51]) is made to change between 1.6% to 4.8% between r/D=0-2; in the region where the acoustic forcing is observed to change the convective heat transfer coefficient. For r/D=2-4, the error variation is 4.8% - 15.4%. On the other hand, radiation effect is 0.3% at r=0, increasing to 2% at r/D=4. Additionally, the in-plane conduction error is checked and found to be negligible. Overall, the uncertainty is reasonably small for $r/D \le 2$, consistent with different studies utilizing a similar setup[20], [52].Using (5.1):

$$h = \frac{Q}{A\Delta T} \tag{5.2}$$

and the Nusselt number is given by

$$Nu = \frac{hD}{k} \tag{5.3}$$

Where, D is the jet diameter, and k is the air thermal conductivity.

Based on (5.2), to determine h, the electrical power dissipated, and the plate and ambient temperatures are measured. The plate is heated by the effect of an electrical current passing through the stainless-steel sheet (Joule heating). The heated sheet is stretched tight on two hollow copper bus bars along its sides. This provides uniform voltage distribution along the edges, which when combined with the uniform thickness of the plate, results in uniform power dissipation per unit area (and hence uniform heat flux) over the heated area of the plate. Thus, q is computed by dividing the electrical power dissipated by the heated area of the plate.

Electrical power is supplied to the heated sheet via two 4-gauge copper cables connected to the two bus bars on one end, and to a DC power supply (Harrison laboratories 6456B), on the

other. The supply can provide a maximum DC voltage and current of 40 V and 100 A respectively. In the experiments, the voltage is set to 1.3V, and the current to 30A, resulting in heating power Q = 39 W. The current is measured using a non-contact Hall-effect CR magnetics current meter (CR5211-100) with a range of 100 Ampere and 0.1 Volt/Ampere sensitivity, and the accuracy is 1%, according to the manufacturer specifications, while the voltage is measured by the ADC board (NI USB 6343) with 0.16% accuracy, based on the manufacturer stated accuracy. The resulting overall electrical power uncertainty is 3.3%.

To verify the steady state condition of the plate, four T-type thermocouples are used to measure the temperature of the plate (mounted at one of the plate corners), the positive bus bar, the negative bus bar, and the ambient temperature. The ambient air thermocouple is located close to the external surface of the jet body, in the same plane as the faceplate. The outputs of the thermocouples are acquired using a National Instruments C Series 4-channel Temperature Input Module (NI 9210 Mini TC) embedded in NI CompactDAQ platform. The specified temperature measurement accuracy of the module is ± 0.8 °C.

Figure 71 shows the temperature variation with time of all four thermocouples during heating and subsequent cooling of the impingement plate. Zero time corresponds to the moment, the heating is turned on. All temperatures are plotted in the format:

$$\frac{\Delta T}{\Delta T_{ref}} = \frac{T(t) - T_0}{T_f - T_0} \tag{5.4}$$

Where t is time, T the temperature being monitored, and T_o and T_f are the initial and final (steady state) values of T. The steady-state condition is determined when the impingement plate mean temperature variation is less than 1%. The measurements are conducted while the jet is running.

As seen from Figure 71, the initial rise in the impingement plate's temperature (red line) is much faster (2.7 minutes) than the overall time it takes to reach steady state (1.5 hour). The fast-initial rise is believed to be due to the relatively small thermal capacitance of the thin stainless-steel sheet, while the longer settling time is likely caused by the slower response of the bus bars (with their larger mass) and the ambient air. Based on these results, all measurements of h are carried out after a wait time of 1.5 hours from the time the heating is turned on (as indicated by the broken magenta line in Figure 71). While at this point, some variation in ambient temperature are still observed (green line in Figure 71), the total variation in T_{amb} during an experiment (which typically lasts for 5 min; the period between the broken magenta and cyan in Figure 71) is less than $0.1^{\circ}C$.

Temperature Sensitive Paint (TSP) [51] is utilized to measure the impingement surface temperature distribution. TSP has been utilized in the literature in different studies. TSP is based on a reversible molecular photoluminescence process of thermal quenching of luminescence. A photon with a particular wavelength is absorbed to excite luminophore from the ground electronic state to excited electronic state and emits radiation with a longer wavelength by losing the excitation energy. The luminescent intensity is a function of the excitation photons and the temperature. The luminescence intensity of most molecules is affected by thermal quenching and therefore it depends on temperature. Specifically, the luminescence intensity decreases with increasing the temperature, following the equation [51]:

$$ln\frac{I}{I_{ref}} = \frac{E_{nr}}{R} \left(\frac{1}{T} - \frac{1}{T_{ref}} \right) \tag{5.5}$$

Where I is the luminescence intensity at temperature T, I_{ref} is the luminescence intensity at a reference temperature T_{ref} , E_{nr} is the activation energy for the non-radiative process, and R

is the universal gas constant. In order, to obtain accurate data, the TSP should be calibrated by obtaining the dependence of the ratio I/I_{ref} on T at a given T_{ref} in a special setup. However, the TSP used in the present measurements uses (5.5) directly with the nominally known value of $E_{nr} = 1045.4 \, kJ$ (taken from [51]) and $R = 287.05 \, \frac{J}{Kg.K}$. Therefore, the results are useful for comparative analysis among the different forced-jet cases and the natural jet, as opposed to providing highly accurate temperature measurements.

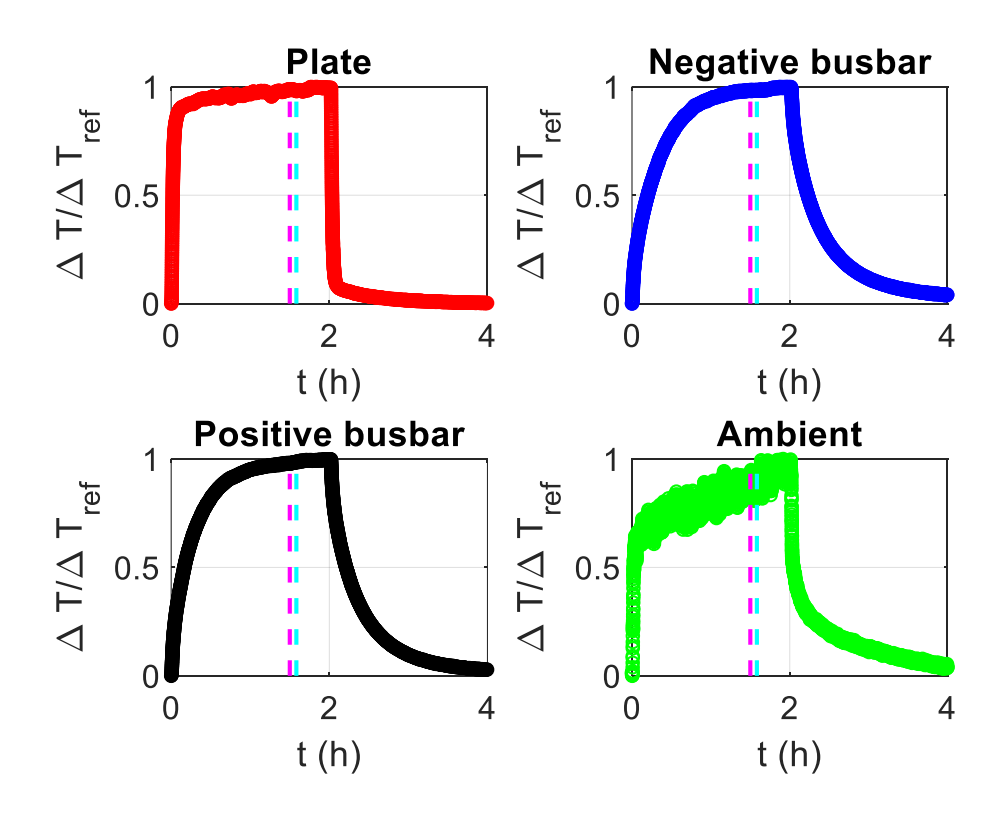


Figure 71 Temperature variation of the heated plate, bus bars and ambient temperature. The magenta broken line in all figures is located at 1.5 hours which is the time at which the experiments starts and the cyan line is located when the experiments end

In the present TSP implementation, a $0.152 \text{ m} \times 0.152 \text{ m}$ white heat-resistant polyester sheet (Mylar sheet) is mounted on the back (non-impingement) side of the stainless-steel sheet. The polyester sheet is painted with TSP, consisting of EuTTA (Europium (III) thenoyltrifluoroacetonate CAS: 21392-96-1) dissolved in model aircraft dope and thinner with a

proportional ratio of (1:1). EuTTA has fluorescence property when activated with UV light (peak absorption at 350 nm wavelength) and it emits at a wavelength of 612 nm. A LED UV lamp is used to excite the EuTTA paint. The stability of the UV lamp is monitored using Thorlab PDA55 photodetector, which showed that the lamp requires 40 minutes to reach steady state (to within less than 0.01%).

The resulting luminescence intensity distribution over the Maylar sheet area is captured using a Charge-Coupled Device (CCD) 14-bit monochromatic camera (FLIR GS3-U3-41S4M-C) fitted with a 50-mm Nikkor lens (f/1.2) and a long-pass filter to remove any UV light from the UV lamp. Due to space restriction, the camera is placed with its axis normal to the centerline of the impingement plate, and the image is captured with the aid of a first-surface mirror tilted at 45° (as depicted in Figure 70). The imaging scale is 0.08 mm/pixel (0.006D/pixel), which is calculated with the aid of a calibration target. The target is made up of a grid printed using a laser printer with 600 dpi resolution, yielding 2.6% uncertainty in the grid size. The grid size is $1.6 \pm 0.026 \text{ mm/cell}$, and it is attached to the bottom of the camera's field of view (see Figure 72). To obtain the imaging scale, the number of cells is counted and multiplied by the grid size then divided by the corresponding number of pixels from the first to the last cell. An example of the measured temperature field is depicted via a flooded color contour map in Figure 73.

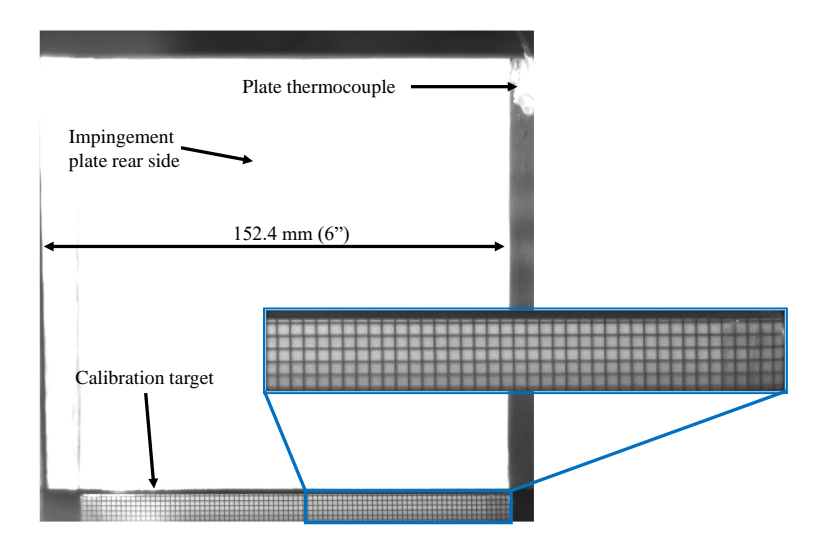


Figure 72 Example image of the back of the impingement plate, used to determine the imaging scale for TSP measurements. A magnified view of the image scale grid is also shown

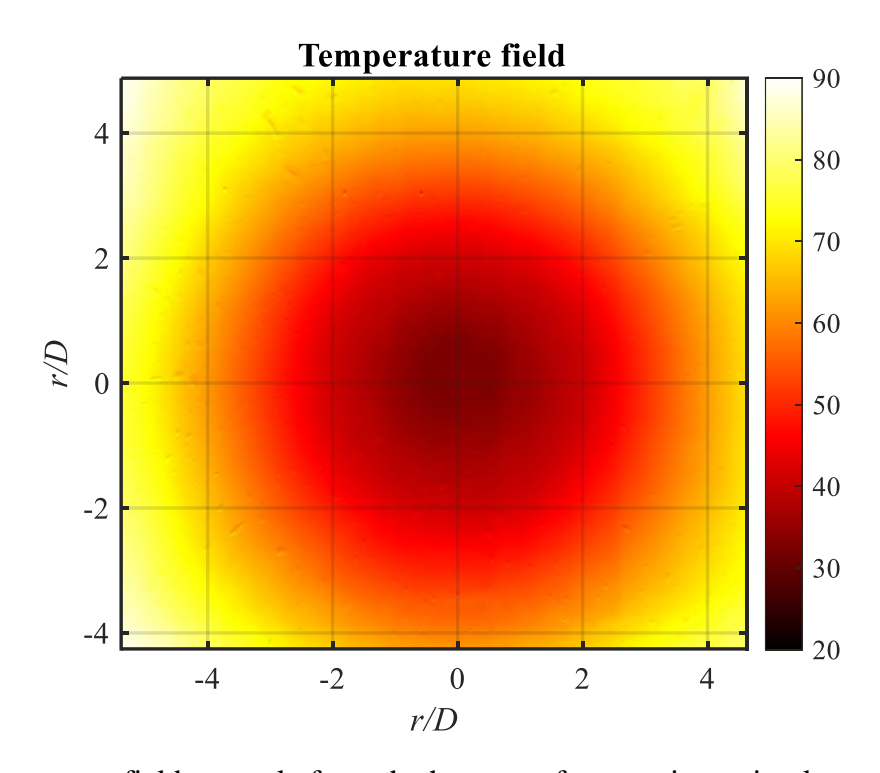


Figure 73 Temperature field example from the heat transfer experiment implemented using TSP technique at H/D=2 and $Re_D=4,233$

5.2 Experimental Procedures and Data Analysis

The heat transfer experiment starts with acquiring the first set of TSP images in a dark environment to estimate the camera noise. This is followed by turning the UV light on for 40 minutes to allow it to reach steady state, while covering the impingement plate's back to reduce

the TSP exposure to UV light in order to minimize the paint deterioration. After 40 minutes, the cover is removed and the second set of images (reference images) is acquired simultaneously with the plate temperature using the thermocouple mounted at the corner of the plate to determine the corresponding reference temperature. Once the acquisition of the reference images is completed, which is done with no heat applied to the impingement plate, the UV light is turned off and the electrical power supply to the impingement plate and the jet flow are turned on.

To reach steady state, the experimental setup is left running for 90 minutes before acquiring the main TSP images. After the first 50 minutes of this period, the UV light is turned on again to allow it to reach steady state at the same time as the overall setup. Once the time required for the plate and the UV light to warm up ends, the experiment is started. A MatLab code is used to generate the acoustic forcing signal and acquire and save the images. The code runs in a loop to acquire images at different forcing intermodal phase angles. The imaging exposure time used in the experiments is 27 ms, and the frame rate is 10 frames/s. For each forcing condition, 200 images are acquired.

During TSP luminescence image acquisition, a few quantities are acquired. Some of these quantities are used for data post-processing: the impingement surface heating current and voltage, the jet volume flow rate, and the ambient temperature. The rest of the quantities are recorded to keep track of the experimental conditions, and to verify that the experiment is implemented under the pre-set conditions. These quantities are the thermocouple-measured temperatures of the impingement plate and the bus bars, the static pressure upstream of the jet faceplate, and the UV-light intensity (photodetector output).

Postprocessing starts with computing the mean image for each of the image sets acquired earlier (dark images set, reference images set, and experiment images set), which yields the pixel-

by-pixel luminescence intensity I distribution over the TSP-covered area. The mean dark image is first subtracted from the experiment mean image and the reference mean image. Then, the ratio R_I between these two luminescence intensities is computed. Specifically,

$$R_I = \frac{I - I_b}{I - I_{ref}} \tag{5.6}$$

Where, I_b is the dark (or black) luminescence intensity. R_I distribution is then used to calculate the temperature field as follows:

$$T = \frac{1}{\frac{\ln R_I}{C} + \frac{1}{T_{ref}}} - 273 \tag{5.7}$$

C is a constant ($C = E_{nr}/R = 3642$), and T_{ref} is the reference temperature measured with the thermocouple attached to the impingement plate. The temperature data are finally used to compute the convective heat transfer coefficient and the Nusselt number.

While TSP allows determination of the planar distribution of Nu over the impingement plate, given the axisymmetric nature of the measurement (e.g. see Figure 73), azimuthal averaging is used in presenting Nu distribution versus the radial coordinate. Additionally, given that the spatial resolution is better than needed (each pixel represents 0.006D), once the azimuthally averaged Nu is obtained, further averaging along the r direction is done using 36-point average. This averaging, which also helps to reduce the random uncertainty, results in Nu(r) distribution in increments of $\Delta r/D = 0.1$. A sample Nu distribution and the radial averaging process for the natural jet is shown in Figure 74. A summary of the heat transfer experiments is listed in Table 5.

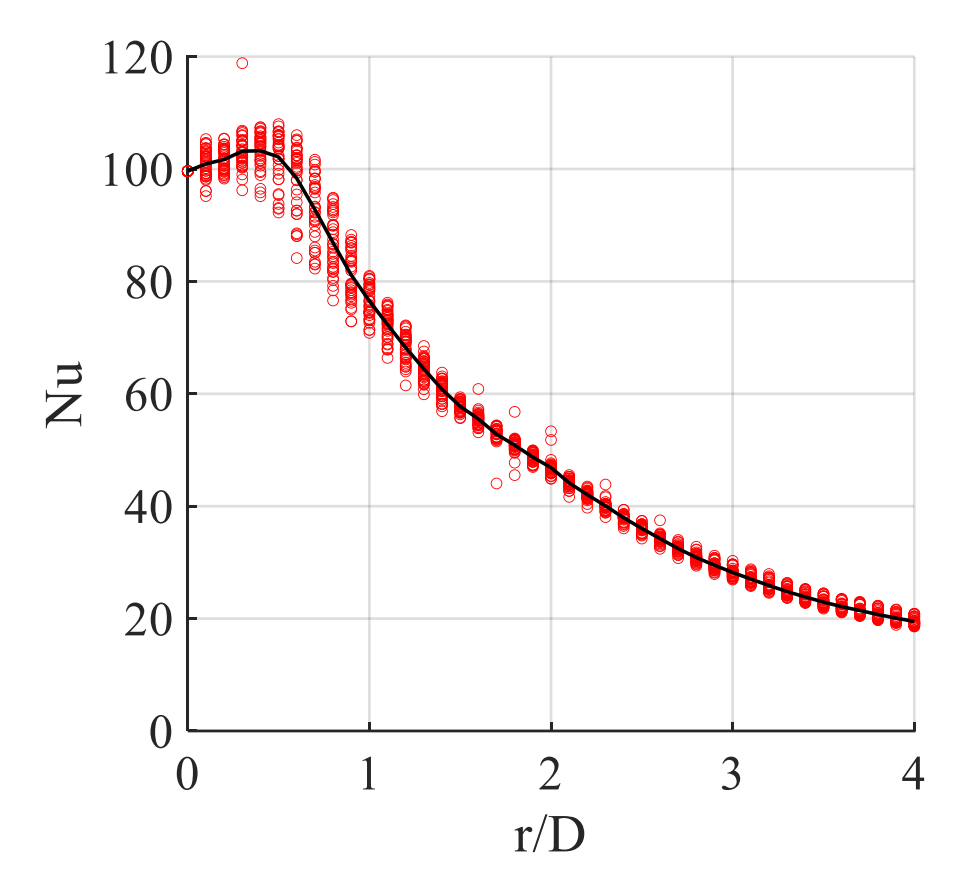


Figure 74 A sample of Nusselt number distribution before averaging (red circles) and after averaging (black line)

Table 5 Summary of the heat transfer experiments

H/D=2			
U_j (m/sec)	5		
Re_D	4,233		
Constant heat power=39 W,		$\phi = 0^{\circ} - 165^{\circ}$ in increments of 15°	
I=30 Ampere and Volt=1.3 Volt			
Forcing amplitude = $0.01U_j$ and unity amplitude ratio			

5.3 Results

With the identified significant influence of bi-modal acoustic forcing on the jet flow structure, it is desired to examine the corresponding effect on the heat transfer from the

impingement plate. In this subsection, data are presented for measurement of the radial distribution of the temperature and the Nusselt number for the natural jet and when the flow is forced.

Before presenting the current study results, a comparison of the natural jet data from the literature and the current study is conducted to check the reasonableness of the present Nusselt number measurements. One difficulty in the comparison is that, to the best of the author's knowledge, the literature does not contain any study reporting Nusselt number data at the same Reynolds number for the sharp-edged impinging jet. Therefore, the comparison is done with Reynolds numbers different than the present one with focus on examining the features of the Nusselt number distribution and how they vary with Reynolds number. The results, shown in Figure 75, demonstrate that the Nusselt number distribution from the present work is consistent with the trend with Reynolds number seen in [20] for $Re_D > 10,000$. Specifically, this trend implies decreasing Nu values with decreasing Reynolds number, and decreasing prominence of the "inner" and "outer" peaks in the distribution. This decrease in the peak visibility is sufficiently strong such that the outer peak is not seen in the present data. The same trend with Reynolds number is seen [53] for a jet emerging from a contoured nozzle. While the study does not have data at H/D = 2, their data at H/D = 1 shows the absence of the outer peak below $Re_D = 11,000$.

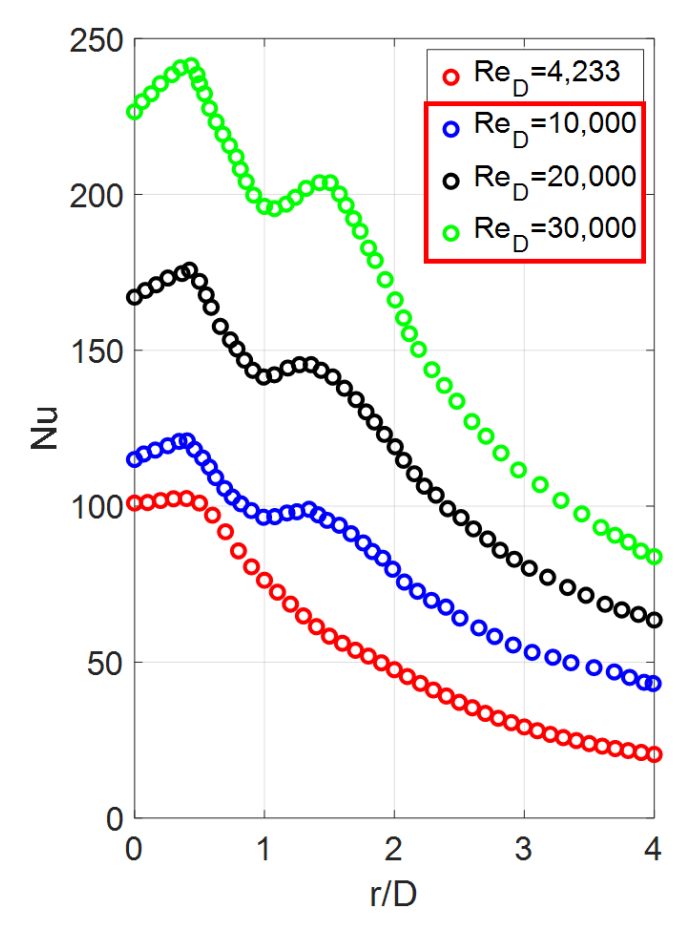


Figure 75 Natural jet Nusselt number radial distribution for different Reynolds numbers. The red circles represents the current study, while the three cases in the red rectangle in the figure legend depict the data taken from [20]

Figure 73 depicts the temperature distribution for the stagnation zone, the wall-jet zone, and the "far field". The stagnation region shows the least temperature across the radial direction, which is indicative of the presence of the highest heat transfer rate in this region. The temperature increases monotonically from the stagnation region to the wall-jet region, and the trend continues to the end of the measurement domain. This is indicative of a corresponding deterioration in the heat transfer rate with increasing r/D.

Following the procedure explained in Section 5.2, the Nusselt number radial distribution is obtained for the natural and the forced jet. The results are depicted in Figure 76 for the natural jet and two of the forcing cases that are equivalent to $\phi = 90^{\circ}$ and $\phi = 165^{\circ}$ in the data reported

in CHAPTER 3 and CHAPTER 4. Two data sets for the natural jet are obtained before and after measurements for the forced cases to ensure no drift has occurred during the experiments. Inspecting Figure 76, it is seen that an increase in Nu is found within the stagnation zone only. The best heat transfer enhancement is found at intermodal phase of 120° (165° -equivalent), with $\phi = 45^{\circ}$ ($90^{\circ}/105^{\circ}$ -equivalent) also exhibiting enhancement. More specifically, the heat transfer enhancement at the stagnation point for forcing intermodal phases of 45° and 120° is 6% and 8.4% respectively. By contrast, the heat transfer in the wall-jet zone is reduced with forcing at 120° , while forcing at 45° does not affect Nu in the same zone. In particular, Nu in the wall-jet region is reduced by approximately 6% at 120° intermodal phase.

Based on the results in CHAPTER 3 and CHAPTER 4, the two phases considered here correspond to different types of jet development. $\phi = 120^{\circ}$ (165°-equivalent) corresponds to the scenario with consistent development of the double-paired symmetric structure, while $\phi = 45^{\circ}$ (90°/105°-equivalent) leads to asymmetric/disorganized vortex structure. The double-paired symmetric structure leads to significant increase in both the vortex size and strength by the impingement location. The heat transfer results in Figure 76 suggest that this increase leads to enhancing the effect of the vortical structures in the vicinity of the stagnation point, leading to the largest observed enhancement in Nu in the stagnation zone. This is hypothesized to be caused by the increased downwash velocity of the merged vortex towards the stagnation zone. The heat transfer enhancement on the downwash side in isolated vortex-wall interaction was clearly demonstrated in the literature, which showed that the maximum Nu enhancement due to the downwash occurs at about one vortex core radius away from the center [41], [42]. It is hypothesized here that with the growth in vortex size though the double pairing process, the influence of the strongest vortex downwash is felt closer to the stagnation point. This, together

with the enhanced vortex strength from pairing is likely the cause of the improvement in the heat transfer in the stagnation zone for the 165°-equivalent case. The lesser improvement seen for the 90°/105°-equivalent case is consistent with this hypothesis. Since this case also leads to improved double pairing but only partially around the jet perimeter due to the asymmetry, the effect of the larger vortex size and strength will be reduced.

The deterioration of the heat transfer in the wall-jet zone (or lack of it) due to the forcing appears to also be consistent with the understanding of the jet vortex structure developed in CHAPTER 3 and CHAPTER 4 [42], [49]. As discussed in connection with Figure 26, the vortex-wall interaction leading to boundary layer separation and secondary vortex formation, is much weaker for $\phi = 105^{\circ}$ in comparison to $\phi = 165^{\circ}$. Thus, it is not surprising to see that the $90^{\circ}/105^{\circ}$ -equivalent case does not lead to heat transfer deterioration in the wall-jet zone, while the 165° -equivalent case does.

The above results suggest that while the double-paired symmetric structure can be beneficial to enhancing the heat transfer in the stagnation zone, it also produces strong boundary layer separation and secondary vortex, reducing the heat transfer in the wall jet zone. However, by changing the intermodal phase it is possible to weaken the vortex-wall interaction in the wall-jet zone at the expense of reducing the heat transfer enhancement in the stagnation zone. This might however lead to a better overall enhancement in the heat transfer. In other words, it might be possible to find an optimum ϕ that produces the best cooling effect throughout both the stagnation and wall-jet regions.

To shed some light on the point of optimality of the forcing condition for heat transfer enhancement, the overall change in Nusselt number over radial domains with various sizes is considered. To do this an average Nusselt number is computed over a given domain as follows:

$$Nu_{avg} = \frac{\int_0^{r_i} Nu(r) 2\pi r dr}{\pi r_i^2}$$

Where, r_i is the radius of the area over which Nu_{avg} is computed. The resulting Nu_{avg} value for a given forcing condition ($\phi = 105^{\circ}$ or 165° - equivalent) is then compared to the natural jet using

$$\Delta Nu_{avg} = \frac{Nu_{avg}(\phi = 105^{\circ} \ or \ 165^{\circ}) - Nu_{avg}(Natrual \ jet)}{Nu_{avg}(Natrual \ jet)}$$

For the above calculation to make sense, it should not be computed over r_i values that extend to infinity. Specifically, the attractiveness of impinging jets in cooling is owing to their high heat transfer rate in, and in the vicinity of the stagnation zone. In the far wall-jet region, Nu drops significantly, and hence in practice, this is compensated for by using impinging jet arrays. If the computation of Nu_{avq} is conducted over a very large domain for a single jet, then inevitably the calculation will be biased towards the lower wall-jet values, which do not represent the practical interest of using impinging jets for cooling. Therefore, the calculation of ΔNu_{avg} is conducted for r_i/D values up to 2. On the other end of the r_i range, it is desirable to compute the average Nusselt number for an area that is not smaller than it is practical to place impinging jets adjacent to each other in an array, since this will be the minimum area cooled predominantly by a single jet. Clearly, a jet-to-jet spacing of S/D = 1 would be the absolute minimum to space jets in an array. However, this does not account for the need to account for the thickness of the wall of the jet body. Therefore, the minimum value of r_i used here is taken to correspond to S/D = 1.4. The results are shown in Figure 77 plotted versus S/D. It is emphasized that no actual array data are used for this figure, and that the results ignores the obviously important effect of jet-jet interaction, which will change Nu and is a complex problem that will depend highly on S/D.

Inspection of Figure 77 shows that the heat transfer shows the best enhancement in the range 1.4 > S/D > 1.6 is attained for $\phi = 165^{\circ}$, while in the range 1.8 > S/D > 4, $\phi = 105^{\circ}$ leads to the best enhancement. This analysis demonstrates the point that there is a possibility that the best forcing condition for Nu enhancement could vary depending on the specific application of the jet in cooling.

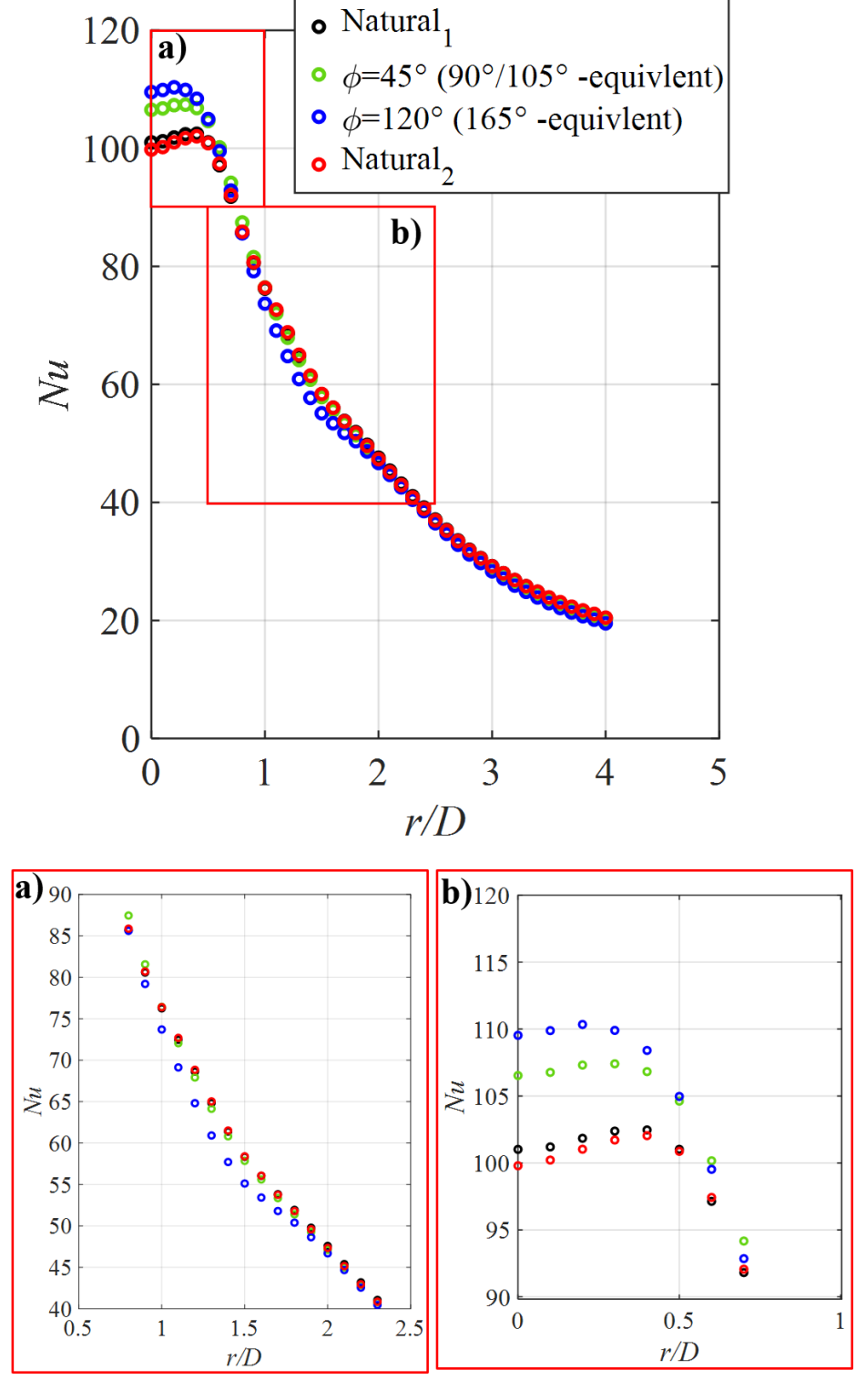


Figure 76 Nusselt number distribution along the radial direction for the natural and forced jet at two values of the intermodal phase. Subplots (a) and (b) provide magnification of the stagnation and the wall-jet zone respectively

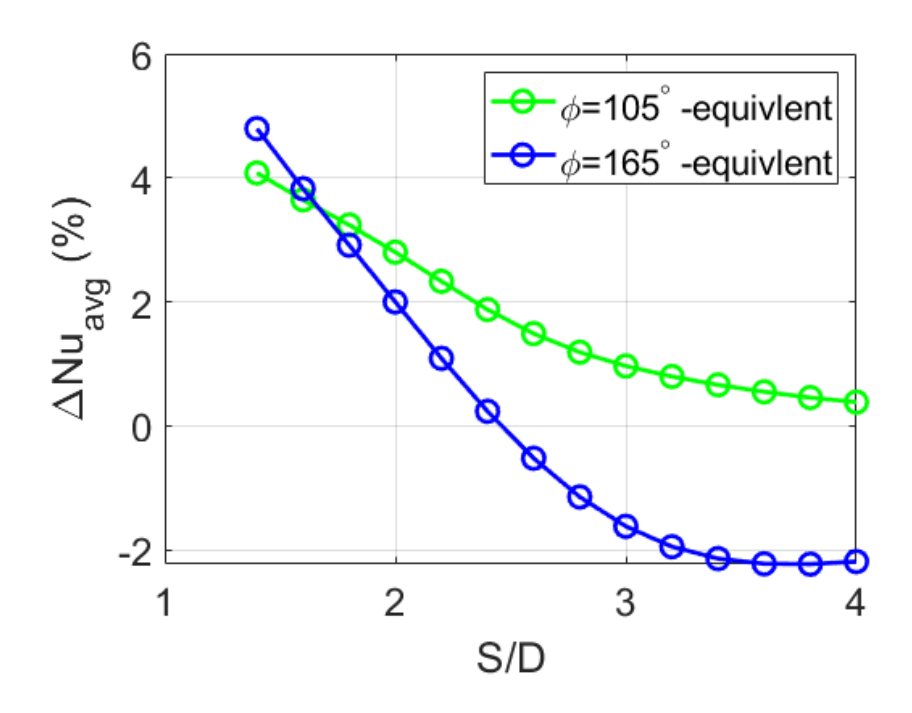


Figure 77 Average Nusselt number enhancement percentage with respect to the natural jet at different nozzle-to-nozzle spacing

CHAPTER 6. CONCLUSIONS AND RECOMMENDATIONS

This work investigates the effect of bi-modal forcing on the vortical structure of a sharp-edged impinging jet at $Re_D = 4,233$. The investigation includes different forcing parameters and nozzle-to-plate distances (H/D = 2, 3, and 4). Additionally, a limited study considers the effect of impinging jets on the heat transfer from the impingement plate.

The bi-modal forcing scheme involves excitation of the jet at two frequencies simultaneously: the initial shear layer instability (fundamental mode, $f = 1000 \ Hz$, $St_D = 2.54$) and its subharmonic (subharmonic mode, $f_{su} = f/2 = 500 \ Hz$, $St_D = 1.27$). Externally forcing the two modes at the same time involves different forcing parameters: the intermodal phase $(\phi = 0^{\circ} - 180^{\circ})$ between the modes at the fundamental and the subharmonic frequency, the amplitude ratio of the two modes $(AR = a_f/a_{fsu} = 0.5, 1, \text{ and } 2)$, and the overall acoustic forcing level (0.1% and 0.3% of U_j). The natural jet and the pure-harmonically forced jet (at f and f_{su}) are also examined to compare the effect of bi-modal forcing to the natural and the pure-harmonically forced jet.

A significant portion of the study focuses on systematically investigating the effect of the intermodal phase on the vortical structure at H/D=2, AR=1, and 0.3% forcing amplitude. The vortical structure is investigated by utilizing a high-speed time-resolved flow visualization, in addition to measuring the streamwise velocity at different radial and streamwise locations using a single hot wire. At the same nozzle-to-plate distance of H/D=2, a limited study of the heat transfer from the plate is conducted. Additionally, flow visualization at different nozzle-to-plate distances, amplitude ratios, and a second forcing level is utilized to compare the effect of the forcing on the vortical structure development.

At H/D=2, AR=1, and 0.3% forcing amplitude, all forcing modes show accelerated vortical structure development with different levels of acceleration depending on the forcing method. The enhanced development is seen in the form of two complete vortex pairing events before reaching the impingement plate. The first pairing happens for two vortices at the fundamental mode frequency (f) yielding one vortex at the subharmonic frequency (f_{su}), and the second pairing between two vortices at the subharmonic frequency producing a vortex at the second subharmonic frequency (f_{2su}). The double-pairing is rarely seen for the natural jet. Forcing at the fundamental forcing frequency accelerates the vortical structure evolution compared to the natural jet; however, the resulting accelerated development is not as much as possible with the other forcing cases. Subharmonic and bi-modal forcing show the most persistent double-pairing between all the forcing cases. The natural jet and the fundamental forcing cases show consistency of single pairing occurrences and occasional three vortex merging. In both cases, the vortical structure shows symmetry between the visualized top and bottom parts of the shear layer.

Bi-modal forcing shows a significant effect on the flow structure development at various intermodal phase values over the full range ($\phi = 0^{\circ} - 180^{\circ}$). At $\phi = 165^{\circ}$ the flow structure exhibits a consistent symmetric double-paired structure, while at $\phi = 90^{\circ}$ the flow shows an inconsistent structure with asymmetric behavior; i.e. pairing on one side only. In the case of the bi-modal forcing at $\phi = 165^{\circ}$, the double-paired symmetric structure produces a larger vortex and yields the narrowest jet core width. This largest vortical structure with the narrowest core width results in the most prominent vortex-wall interaction leading to the formation of the secondary vortex.

Pure-harmonic forcing at the subharmonic frequency produces frequent double-paired symmetric structure that is the most energetic of all cases. However, subharmonic forcing also

induces some randomness and switching between the double-paired structure, the single-paired structure, and the asymmetric structure. In comparison, while not as energetic, bi-modal forcing at $\phi = 165^{\circ}$ leads to the most accelerated development with the most organized and repeatable double-paired symmetric structure.

Bi-modal forcing at the proper intermodal phase is expected to develop subharmonic resonance between the fundamental (f) and the subharmonic (f_{su}) mode. Surprisingly, the streamwise development of the shear layer modal energy shows no evidence of such resonance. Instead, the streamwise development of the modal energy shows possible resonance between the mode at the subharmonic frequency (f_{su}) and the mode at the second subharmonic frequency (f_{2su}) for the cases showing the most accelerated development and most consistent symmetric double-pairing (subharmonic forcing and bi-modal forcing at $\phi = 165^{\circ}$). This resonance is hypothesized to be the reason for the most vortical structure development enhancement. Additionally, the modal phase development along the jet centerline shows a 90° intermodal phase transition for the subharmonic forcing and the bi-modal forcing at $\phi = 165^{\circ}$ at the resonance location. The intermodal phase transition at the resonance location is evidence of the resonance occurrence. Furthermore, the convection velocity of the subharmonic and the second subharmonic mode is found to have similar values, which would permit the occurrence of resonance.

The intermodal phase transition for bi-modal forcing at $\phi = 165^{\circ}$ shows a sharp transition, while the subharmonic forcing shows a gradual transition. The sharp transition implies consistent cycle-to-cycle double-pairing and organized structure, this is also seen visually in the flow visualization videos, and the time percentage the organized structure is found to occur in these videos. In the case of the subharmonic forcing, the transition is more gradual rather than sharp, which indicates more jitter and randomness of the resonance location. The absence of the

fundamental forcing frequency in the subharmonic forcing scheme leads to a lack in the initial organized structure forced by the fundamental mode. This affects the organized occurrence of the first pairing, which affects the second pairing by inducing occasional randomness and switching in the vortical structure development.

The two cases exhibiting the best development of the double-paired symmetric structure (subharmonic and bimodal $\phi=165^{\circ}$) are found to have the highest velocity fluctuation level of the second subharmonic mode (f_{2su}) at the jet exit. Therefore, it is hypothesized that the early presence of velocity fluctuation at this frequency is significant to the promotion of the double-paired symmetric structure. Given that the second subharmonic frequency is not included in the forcing scheme, it is hypothesized that the presence of the second subharmonic mode is due to the acoustic wave created by the occurrence of the second pairing, or feedback from the interaction of the double-paired structure with the impingement wall in the stagnation region and/or the wall jet region.

The limited heat transfer experiments reported in this work show that bi-modal forcing can lead to enhancement of the heat transfer in the stagnation zone. However, it can also cause some deterioration in the wall-jet zone. The actual behavior is dependent on the intermodal phase. Understanding of the effect of bi-modal forcing on the vortex structure suggests that the heat transfer improvement is caused by a stronger vortex downwash of the double-paired structure in the stagnation region. In contrast, the heat transfer drop in the wall-jet zone is reasoned to be due to the stronger vortex-wall interaction of the double-paired symmetric structure, which leads to more energetic separation of the boundary layer and the formation of the secondary vortex. The asymmetric vortical structure for the bi-modal forcing at $\phi = 90^{\circ}$ is not expected to create as strong of a downwash as the symmetric structure. Hence, it is expected to lead to less heat transfer

improvement in the stagnation zone. On the other hand, the heat transfer in the wall jet zone is not reduced due to the presence of the weaker asymmetric vortical structure, which results in a weaker separation of the boundary layer. An optimum intermodal phase that leads to the best enhancement in both the stagnation and wall-jet zones might exist. It is important to note that the heat transfer measurements were challenging, and a focused future study is required to confirm the present findings and to examine the heat transfer aspects of the impinging jet in details.

At H/D=2, AR=1, and 0.1% forcing amplitude, all forced modes show some organization; however, the amount of organization is found to be significantly less than that at the forcing amplitude of 0.3%. This indicates that the forcing amplitude must be high enough to have a substantial effect on the jet. Future studies are needed to investigate the sensitivity of the vortical structure to the forcing amplitude.

The different amplitude ratios (AR = 0.5, 1, 2) at H/D=2 and 0.3% forcing level cause different developmental behavior. All amplitude ratios show relatively similar qualitative behavior with consistent organized double-paired symmetric structure found in most of the ϕ range, and disorganized asymmetric structure in the remainder of the range. While the ϕ intervals for organization and disorganization of the structure for different AR values roughly overlap, at AR=0.5 the disorganized structure is dominant over a narrower intermodal phase band compared to the other two higher amplitude ratios. At the latter ratios of AR=1 and 2, the disorganized structure occurs over a similar ϕ range.

When it comes to the effect of nozzle-to-plate distances (H/D), no significant influence is found on bi-modal forcing among = 2,3,4 cases. The most significant effect of H/D is on the jet response to subharmonic forcing. Increasing H/D is found to result in more consistent and frequent

development of the double-paired symmetric structure. This leads to the hypothesis that the intermittent less organized behavior of the vortices at H/D=2 under subharmonic forcing is related to interaction of the vortices with the plate coupled with sufficient proximity of the plate to the jet exit (i.e. strong feedback effects).

BIBLOGRAPHY

- [1] J. Cohen and I. Wygnanski, "The evolution of instabilities in the axisymmetric jet. Part 1. The linear growth of disturbances near the nozzle," *J. Fluid Mech.*, vol. 176, no. 1, p. 191, 1987.
- [2] Y. Aj, "Large-scale structure in the mixing layer of a round jet," *J. Fluid Mech.*, vol. 89, no. 1978, 1978.
- [3] W. H. Drazin, P. G., & Reid, *Hydrodynamic stability*. Cambridge university press, 2004.
- [4] S. C. Crow and F. H. Champagne, "Orderly structure in jet turbulence," *J. Fluid Mech.*, vol. 48, no. 3, pp. 547–591, 1971.
- [5] W. K. Grinstein, F. F., Glauser, M. N. and George, "Fluid vortices," in *Fluid Vortices*, S. Green, Ed. Springer Science+Business Media Dordrecht, 1995.
- [6] C. O. Popiel and O. Trass, "Visualization of a free and impinging round jet," *Exp. Therm. Fluid Sci.*, vol. 4, no. 3, pp. 253–264, May 1991.
- [7] H. S. Husain and F. Hussain, "Experiments on subharmonic resonance in a shear layer," *J. Fluid Mech.*, vol. 304, pp. 343–372, 1995.
- [8] E. Gutmark and C. M. Ho, "Preferred modes and the spreading rates of jets," *Phys. Fluids*, vol. 26, no. 10, pp. 2932–2938, 1983.
- [9] A. K. M. F. Hussain and K. B. M. Q. Zaman, *The 'preferred mode' of the axisymmetric jet*, vol. 110. 1981.
- [10] C.-M. Ho and P. Huerre, "Perturbed free shear layers," AnRFM, vol. 16, pp. 365–424, 1984.
- [11] J. Vejrazka, J. Tihon, P. Mart, and V. Sobolík, "Effect of an external excitation on the flow structure in a circular impinging jet," *Phys. Fluids*, vol. 17, no. 10, 2005.
- [12] J. F. Arbey, H., & Williams, "Active cancellation of pure tones in an excited jet," *J. Fluid Mech.*, vol. 149, pp. 445–454, 1984.
- [13] C. M. Ho and L. S. Huang, "Subharmonics and vortex merging in mixing layers," *J. Fluid Mech.*, vol. 119, pp. 443–473, 1982.

- [14] I. Namer and M. V. Ötügen, "Velocity measurements in a plane turbulent air jet at moderate Reynolds numbers," *Exp. Fluids*, vol. 6, no. 6, pp. 387–399, 1988.
- [15] R. C. Deo, J. Mi, and G. J. Nathan, "The influence of Reynolds number on a plane jet," *Phys. Fluids*, vol. 20, no. 7, 2008.
- [16] W. R. Quinn and J. Militzer, "Effects of nonparallel exit flow on round turbulent free jets," *Int. J. Heat Fluid Flow*, vol. 10, no. 2, pp. 139–145, 1989.
- [17] W. R. Quinn, "Upstream nozzle shaping effects on near field flow in round turbulent free jets," *Eur. J. Mech. B/Fluids*, vol. 25, no. 3, pp. 279–301, 2006.
- [18] J. Mi, G. J. Nathan, and D. S. Nobes, "Mixing characteristics of axisymmetric free jets from a contoured nozzle, an orifice plate and a pipe," *J. Fluids Eng.*, vol. 123, no. 4, pp. 878–883, 2001.
- [19] J. Mi, P. Kalt, G. J. Nathan, and C. Y. Wong, "PIV measurements of a turbulent jet issuing from round sharp-edged plate," *Exp. Fluids*, vol. 42, no. 4, pp. 625–637, 2007.
- [20] J. Lee and S. J. Lee, "The effect of nozzle configuration on stagnation region heat transfer enhancement of axisymmetric jet impingement," *Int. J. Heat Mass Transf.*, vol. 43, no. 18, pp. 3497–3509, 2000.
- [21] J. Mi, G. J. Nathan, and R. E. Luxton, "Centreline mixing characteristics of jets from nine differently shaped nozzles," *Exp. Fluids*, vol. 28, no. 1, pp. 93–94, 2001.
- [22] N. Ho, Chin Ming and Nossair, "Dynamics of an impinging jet. part 1. the feedback phenomenon," *J. Fluid Mech.*, vol. 105, pp. 119–142, 1981.
- [23] C. M. Didden, Norbert and Ho, "Unsteady separation in a boundary layer produced by an impinging jet," *J. Fluid Mech.*, vol. 160, pp. 235–256, 1985.
- [24] C. C. Landreth and R. J. Adrian, "Impingement of a low Reynolds number turbulent circular jet onto a flat plate at normal incidence," *Exp. Fluids*, vol. 9, no. 1–2, pp. 74–84, 1990.
- [25] E. Gutmark, M. Wolfshtein, and I. Wygnanski, "The plane turbulent impinging jet," *J. Fluid Mech.*, vol. 88, no. 4, pp. 737–756, 1978.
- [26] L. Tianshu and J. P. Sullivan, "Heat transfer and flow structures in an excited circular impinging jet," *Int. J. Heat Mass Transf.*, vol. 39, no. 17, pp. 3695–3706, 1996.
- [27] A. S. Ginevsky, Y. V. Vlasov, and R. K. Karavosov, *Acoustic Control of Turbulent Jets*. Berlin, Heidelberg: Springer Berlin Heidelberg, 2004.

- [28] H. E. Paschereit, C.O., Wygnanski, I., and Fiedler, *Experimental investigation of an axisymmetric jet in a coflowing airstream.*, vol. 14, no. 9. 1995.
- [29] C. O. Paschereit, I. Wygnanski, and H. E. Fiedler, "Experimental investigation of subharmonic resonance in an axisymmetric jet," *J. Fluid Mech.*, vol. 283, pp. 365–407, 1995.
- [30] G. RAMAN and E. J. RICE, "Axisymmetric jet forced by fundamental and subharmonic tones," *AIAA J.*, vol. 29, no. 7, pp. 1114–1122, 1991.
- [31] K. Jambunathan, E. Lai, M. A. Moss, and B. L. Button, "A review of heat transfer data for single circular jet impingement," *Int. J. Heat Fluid Flow*, vol. 13, no. 2, pp. 106–115, 1992.
- [32] G. M. Carlomagno and A. Ianiro, "Thermo-fluid-dynamics of submerged jets impinging at short nozzle-to-plate distance: A review," *Exp. Therm. Fluid Sci.*, vol. 58, pp. 15–35, 2014.
- [33] S. D. Hwang and H. H. Cho, "Effects of acoustic excitation positions on heat transfer and flow in axisymmetric impinging jet: Main jet excitation and shear layer excitation," *Int. J. Heat Fluid Flow*, vol. 24, no. 2, pp. 199–209, 2003.
- [34] S. D. Hwang, C. H. Lee, and H. H. Cho, "Heat transfer and flow structures in axisymmetric impinging jet controlled by vortex pairing," *International Journal of Heat and Fluid Flow*, vol. 22, no. 3. pp. 293–300, 2001.
- [35] C. J. Hoogendoorn, "The effect of turbulence on heat transfer at a stagnation point," *Int. J. Heat Mass Transf.*, vol. 20, no. 12, pp. 1333–1338, 1977.
- [36] N. T. Obot, W. J. M. Douglas, and A. S. Mujumdar, "Effect of semi-confinement on impingement heat transfer," in *International Heat Transfer Conference Digital Library*, 1982.
- [37] C. O. Popiel and L. Boguslawski, "Effect of flow structure on the heat or mass transfer on a flat plate in impinging round jet," in 2nd UK National Conf. on Heat Transfer, 1988, vol. 1, pp. 663–685.
- [38] L. A. Brignoni and S. V Garimella, "Effects of nozzle-inlet chamfering on pressure drop and heat transfer in confined air jet impingement," *Int. J. Heat Mass Transf.*, vol. 43, no. 7, pp. 1133–1139, 2000.
- [39] S. Roux, M. Fénot, G. Lalizel, L. E. Brizzi, and E. Dorignac, "Experimental investigation of the flow and heat transfer of an impinging jet under acoustic excitation," *Int. J. Heat Mass Transf.*, vol. 54, no. 15–16, pp. 3277–3290, 2011.

- [40] M. Al-Aweni, "SIMULTANEOUS FLOW VISUALIZATION AND UNSTEADY-SURFACE-PRESSURE MEASUREMENTS IN NORMALLY AND OBLIQUELY IMPINGING JETS," PhD Thesis, Michigan State University, 2013.
- [41] H. H. Jabbar and A. M. Naguib, "A computational study of vortex rings interacting with a constant-temperature heated wall," *Int. J. Heat Fluid Flow*, vol. 76, pp. 197–214, 2019.
- [42] H. H. Jabbar, "A computational study of vortex rings interaction with a constant-temperature heated wall," Michigan State University, 2020.
- [43] R. S. Bunker, J. E. Dees, and P. Palafox, *Impingement Cooling in Gas Turbines: Design, Applications, and Limitations*, vol. 76. 2014.
- [44] E. M. Sparrow, J. P. Abraham, and W. J. Minkowycz, "Flow separation in a diverging conical duct: Effect of Reynolds number and divergence angle," *Int. J. Heat Mass Transf.*, vol. 52, no. 13–14, pp. 3079–3083, 2009.
- [45] T. L. Doligalski and J. D. A. Walker, "The boundary layer induced by a convected two-dimensional vortex," *J. Fluid Mech.*, vol. 139, pp. 1–28, Feb. 1984.
- [46] D. Fabris, D. Liepmann, and D. Marcus, "Quantitative experimental and numerical investigation of a vortex ring impinging on a wall," *Phys. Fluids*, vol. 8, no. 10, pp. 2640–2649, 1996.
- [47] C. P. Gendrich, D. G. Bohl, and M. M. Koochesfahanif, "Whole-field measurements of unsteady separation in a vortex ring/wall interaction," 28th Fluid Dyn. Conf., 1997.
- [48] U. Piomelli, "Large-eddy simulations," in *Advanced Approaches in Turbulence*, Elsevier, 2021, pp. 83–131.
- [49] H. H. Jabbar and A. M. Naguib, "On the links between unsteady separation and Nusselt number deterioration during vortex-wall interaction," *Int. J. Heat Fluid Flow*, vol. 96, no. September 2021, p. 108979, Aug. 2022.
- [50] P. Laufer, J., & Monkewitz, "On turbulent jet flows-a new perspective," 6th Aeroacoustics Conf., p. 962, 1980.
- [51] L. and S. Tianshu, *Pressure and temperature senstive paint*. 2005.
- [52] L. N. Cattafesta, T. Liu, and J. P. Sullivan, "Uncertainty Estimates for Temperature-Sensitive Paint Measurements with Charge-Coupled Device Cameras," *AIAA J.*, vol. 36, no. 11, pp. 2102–2108, Nov. 1998.

[53] D. Lytle and B. W. Webb, "Air jet impingement heat transfer at low nozzle-plate spacings," *Int. J. Heat Mass Transf.*, vol. 37, no. 12, pp. 1687–1697, 1994.

APPENDIX

Centerline mean velocity profile for non-impinging jet

The free jet (non-impinging jet) streamwise mean velocity profile measured at the jet centerline for different Re_D shows flow acceleration due to the presence of vena-contracta.

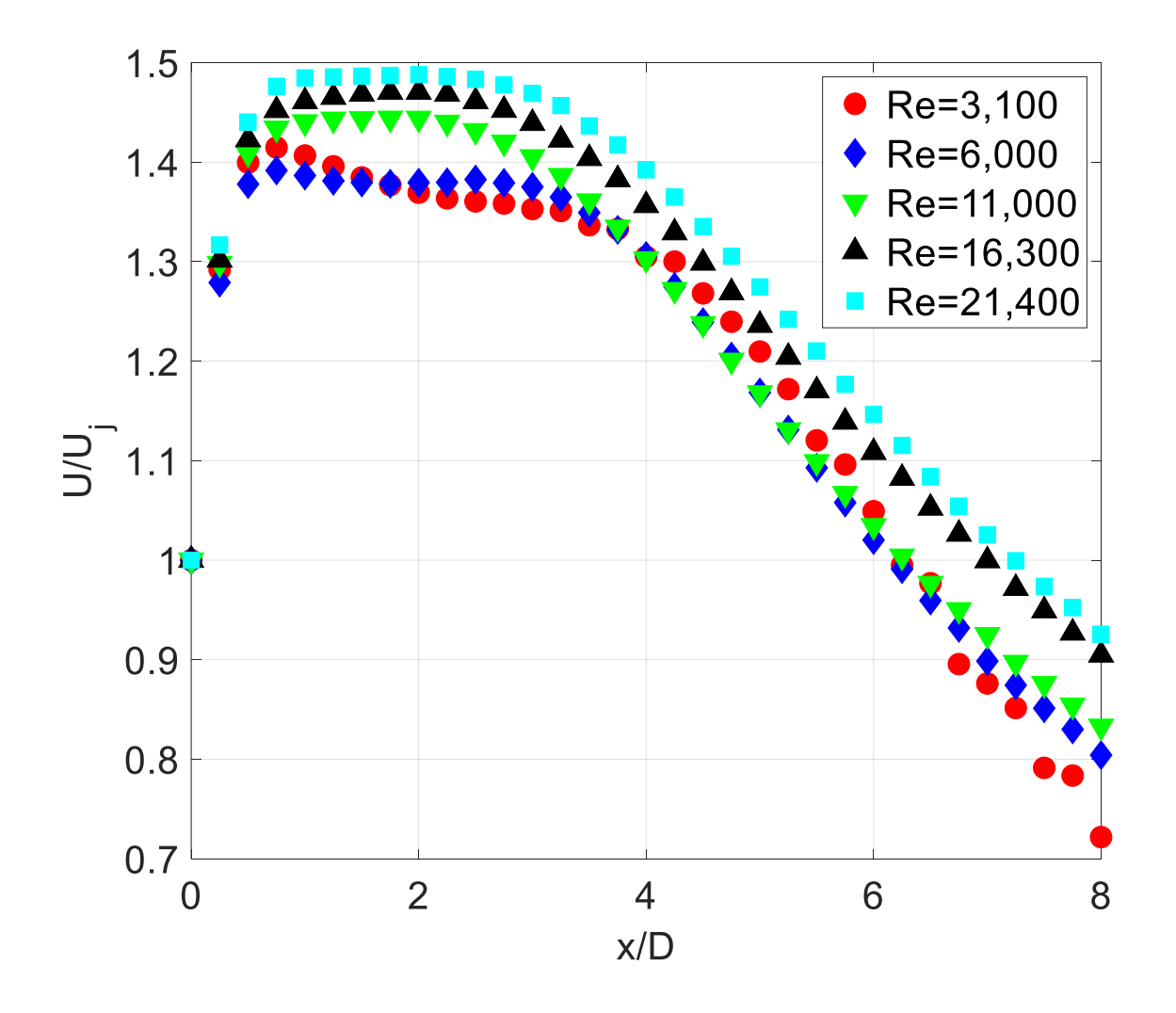


Figure 78 Centerline mean velocity profile for non-impinging jet at different Reynold's number